Search for Gaugino Production in R-parity violating Supersymmetry with the ZEUS Detector at HERA

Dissertation
zur Erlangung des Doktorgrades
des Fachbereichs Physik der
Universität Hamburg

vorgelegt von

Chi Nhan Nguyen
aus
Long An (Vietnam)

Hamburg
November 2005

Gutachter der Dissertation:	Prof. Dr. P. Schleper
	Prof. Dr. J. Meyer
Gutachter der Disputation:	Prof. Dr. R. Klanner
	Dr. A. Geiser
Datum der Disputation:	08. Dezember 2005
Vorsitzender des Prüfungsausschusses:	Prof. Dr. G. Heinzelmann
Vorsitzender des Promotionssausschusses:	Prof. Dr. G. Huber
Dekan des Fachbereichs:	Prof. Dr. G. Huber

Abstract

A search for gaugino production in R-parity violating supersymmetry has been performed with the ZEUS detector at HERA using a data set corresponding to an integrated luminosity of 121.1 pb^{-1}. The data contains events from e^+p and e^-p collisions at a centre of mass energy of 300 GeV and 318 GeV, recorded in the years 1996 to 2000. Theoretically, neutralinos and charginos are produced via t-channel exchange of a left-handed scalar electron or a scalar neutrino, the superpartners of the electron and the neutrino, respectively. It is assumed that one single Yukawa coupling λ'_{1j1}, with $j = 1, 2$, is dominant, while the contributions from the other Yukawa couplings are negligible.
No deviation from the Standard Model was observed and exclusion limits on parameters of the Minimal Supersymmetric Standard Model were obtained. Excluded areas in the (μ, M_2)-plane were derived, which partially extend the corresponding results from LEP. In addition, limits on the masses of left-handed selectrons and the lightest neutralino were derived assuming that $\tilde{\chi}_1^0$ is the lightest supersymmetric particle (LSP) and has a dominant photino component. Selectron masses up to 150 GeV and LSP masses up to 89 GeV were excluded at 95% C.L.

Kurzfassung

Mit dem ZEUS Detektor bei HERA wurde eine Suche nach Gauginos im Rahmen der R-Paritätsverletzenden Supersymmetry durchgeführt. Der untersuchte Datensatz stammt aus den Jahren zwischen 1996 und 2000 und entspricht einer Luminosität von 121.1 pb^{-1}. Die Daten enthalten sowohl Ereignisse aus e^+p als auch aus e^-p Kollisionen mit Schwerpunktsenergien von 300 GeV und 318 GeV. Theoretisch können Neutralinos und Charginos durch den Austausch von linkshändigen, skalaren Elektronen und skalaren Neutrinos, den Superpartnern der Elektronen und Neutrinos, produziert werden. Dabei wurde eine dominante Yukawa-Kopplung λ'_{1j1}, mit $j = 1, 2$, vorrausgesetzt, während alle anderen Yukawa-Kopplungen als vernachlässigbar klein angenommen wurden.
Es konnte keine signifikante Abweichung vom Standard Modell beobachtet werden. Ausschließungsgrenzen (95% C.L.) für die Parameter μ und M_2 des Minimalen Supersymmetrischen Standard Modells wurden abgeleitet. Diese stellen eine teilweise Verbesserung entsprechender Ergebnisse bei LEP dar. Zusätzlich wurden Grenzen auf die Massen der skalaren Elektronen und des leichtesten Neutralinos gesetzt unter der Annahme, daß das Neutralino das leichteste supersymmetrische Teilchen (LSP) und photino-artig ist. Skalare Elektronmassen bis zu 150 GeV und LSP-Massen bis zu 89 GeV konnten ausgeschlossen werden (95% C.L.).

Contents

Chapter 1

Introduction

The Standard Model of particle physics (SM) is a very successful theory in describing particles and interactions up to energies of a few hundred GeV. However, there are several problems which give rise to the question whether the SM is really a complete theory. The so called hierarchy problem or fine tuning problem is maybe the most severe indication that the Standard Model might not be valid for all energy scales. Gravitation, dark matter and the unification of the known forces are other issues, where the SM fails to give answers. Hence, it is expected that new physics has to occur as the energy scale approaches 1 TeV. Supersymmetry (SUSY) is the most promising extension of the Standard Model. It establishes a fundamental relationship between fermions and bosons and predicts new particles in addition to the known particles of the SM.

R-parity (R_p), the quantum number which distinguishes SM particles from their superpartners, is phenomenologically of great importance, because its conservation implies baryon as well as lepton number conservation. However, the most general Lagrangian for supersymmetric theories does not exclude R-parity violating ($\not{R}_P$) terms explicitely.

Previous searches at LEP (Large Electron Positron Collider), Tevatron, HERA (Hadron-Elektron Ringanlage) [1] and other, low energy experiments could not prove the existence of supersymmetric particles. The results from the LEP collider which operated at centre of mass energies up to 209 GeV represent to date the best limits on neutralino, chargino and light slepton masses in the framework of R-parity conserving (RPC) and $\not{R}_P$ supersymmetry, while the Tevatron, operating at centre of mass (cms) energies up to $E_{cms} = 1.96$ GeV, has the best sensitivity for squarks. Slepton masses up to about 100 GeV and squark masses up to more than 250 GeV could be excluded for many SUSY scenarios.

HERA provides an ideal environment to look for R-parity violating supersymmetry, in particular for processes proceeding via the $L_i Q_j \bar{D}_k$ operator with the Yukawa-like coupling λ'_{1jk}, since a lepton and quarks are available in the initial state.

Motivated by phenomenological studies [2], previous searches for $\not{R}_P$ SUSY [3] at HERA have been performed looking for resonant squark production in the s-channel. This production mode is considered to be the most promising process to search for $\not{R}_P$ supersymmetry at HERA provided the squark mass is smaller than about 250 GeV. Special attention was given to stop production [4], since large mixings can be significant in the third family which lead to very light stop mass eigenstates, especially for large $\tan\beta$. No deviation from the Standard Model was observed in any of these searches and upper bounds on the Yukawa couplings λ'_{1jk} as a function of squark mass were derived.

Strong constraints on squark masses exist from Tevatron and low energy processes. The strongest bounds on many $\not{R}_P$ Yukawa couplings come from low energy experiments, they usually depend on the squark and gluino masses [5–7]. Theoretically, in most scenarios it is expected that squarks are much heavier than sleptons, so that squarks might have escaped detection, whereas sleptons are still in reach of current colliders. The most promising process at HERA, which is independent of squark masses, is the t-channel exchange of a slepton via the Yukawa coupling λ'_{1jk}, leading to a final state with a quark jet and a neutralino or chargino.

In this thesis a search for these processes is performed with the ZEUS detector at HERA using e^+p and e^-p data, collected in the years between 1996 – 2000, which corresponds to an integrated luminosity of 121.1 pb^{-1}.

An overview of Standard Model physics at HERA is given in Chapter 2, followed by an introduction to supersymmetry in Chapter 3, where the emphasis of the topics are chosen to suit the supersymmetric process under investigation. Chapter 4 explains the experimental environment, namely the HERA collider and the ZEUS detector. The Chapter 5 and Chapter 6 are dedicated to simulation of physics processes and detector performance and the reconstruction of measured quantities. The methods used to distinguish the signal events from the background are presented in Chapter 7. Chapter 8 gives a detailed description of the search strategy and the data analysis based on the methods developed in the previous chapters. In Chapter 9 all results are presented and, finally, a summary and an outlook is given in Chapter 10.

Chapter 2

Standard Model Physics at HERA

A general introduction to electron[1]-proton scattering at the HERA collider is given in the following sections, focusing on SM physics which can be a potential source for background events to the SUSY processes under study.

2.1 Brief Overview of the Standard Model

Our current best knowledge of matter and interactions is formulated in the Standard Model [8]. The SM includes the electroweak theory (EW) [9] and quantum chromodynamics (QCD) [10] which both are based on quantum field theory [11]. While the EW provides a unified description of quantum electrodynamics (QED) and the weak force, QCD describes the strong force.

From the view of the SM the world is built from elementary particles with spin 1/2, the quarks and leptons, and the forces between these fermions, mediated by gauge bosons (spin 1). Quarks and leptons come in three generations as listed in Table 2.1 and the forces are the electromagnetic, the weak and the strong force, summarised in Table 2.2. The gravitational force has not been included, since there are severe problems to join gravitational interaction and quantum field theory.

The EW is based on the gauge group $\mathrm{SU(2)_L} \times \mathrm{U(1)_Y}$. The symmetry requires massless gauge bosons, which is contrary to observations at high energy physics experiments. This problem is solved by introducing a scalar field, associated with the Higgs boson (H), which induces spontaneous symmetry breaking [12] at energies below the electroweak unification scale. All massive particles aquire mass via their Yukawa interaction with the Higgs field.

QCD is a non-Abelian gauge theory based on the group $\mathrm{SU(3)}_c$ of colour. A consequence of the structure of QCD is asymptotic freedom and confinement. At

[1] Unless stated otherwise, the term 'electron' refers to both positron and electron and the term 'neutrino' refers to both neutrino and anti-neutrino.

	1.	**2.**	**3.**	**Forces**
Leptons	$\begin{pmatrix} \nu_e \\ e \end{pmatrix}_L$ e_R	$\begin{pmatrix} \nu_\mu \\ \mu \end{pmatrix}_L$ μ_R	$\begin{pmatrix} \nu_\tau \\ \tau \end{pmatrix}_L$ τ_R	electromagnetic, weak
Quarks	$\begin{pmatrix} u \\ d \end{pmatrix}_L$ $u_R\ d_R$	$\begin{pmatrix} c \\ s \end{pmatrix}_L$ $c_R\ s_R$	$\begin{pmatrix} t \\ b \end{pmatrix}_L$ $t_R\ b_R$	electromagnetic, weak, strong

Table 2.1: SM particles and the forces in which they participate.

Force	electromagnetic	weak	strong
Gauge Boson	photon (γ)	$W^\pm$, Z^0	8 gluons

Table 2.2: Gauge bosons associated with the three fundamental forces described by the SM.

short distances the strong coupling is small, i.e. the quarks are moving almost freely within the hadrons, while at large distances the coupling gets increasingly strong. This is the reason, why it is not possible to observe bare quarks directly, but only as composite colourless states.

2.2 Deep Inelastic Scattering

The kinematics of ep collisions can be illustrated with the help of a general Feynman diagram shown in Figure 2.1. The electron (e) interacts with the proton (p)

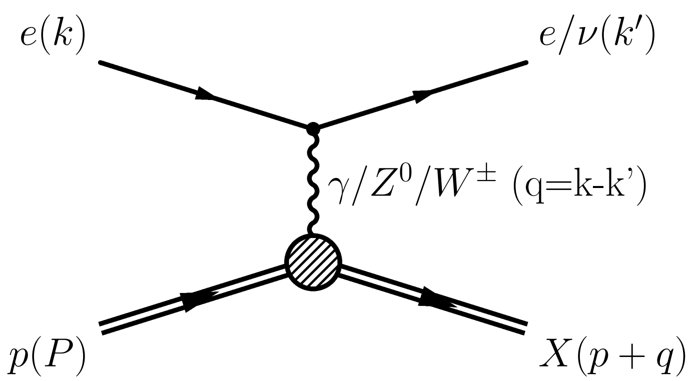

Figure 2.1: Electron Proton scattering.

by an exchange of a virtual vector boson, where X stands for the hadronic final state, in which the proton fragments after the interaction. Assuming that k and

k' are the four vectors of the initial and final lepton and P and $P+q$ are those of the incoming proton and the outgoing final state hadronic system X, where q is the four vector of the exchanged boson, the variables usually used to describe the kinematics are:

$$\sqrt{s} = \sqrt{(k+P)^2}, \tag{2.1}$$
$$Q^2 = -q^2 = (k-k')^2, \tag{2.2}$$
$$x = \frac{Q^2}{2P\cdot q}, \tag{2.3}$$
$$y = \frac{q\cdot P}{k\cdot P}, \tag{2.4}$$

where $\sqrt{s}$ is the cms energy of the lepton-proton system. At the moment the HERA cms energy is $\sqrt{s} = 318\,\mathrm{GeV}$. Q^2 is the four momentum transfer squared. It determines the hardness of the collision. Deep inelastic scattering (DIS) refers to processes, where Q^2 is much higher than $1\,\mathrm{GeV}^2$ and where the invariant mass of the hadronic system is much larger than the proton mass ($M_X \gg M_p$). Processes with $Q^2 \lesssim 1\,\mathrm{GeV}^2$ usually lead to soft interactions. At present, HERA covers a Q^2 region up to $40,000$ GeV^2. The phase space covered by HERA and fixed-target experiments are depicted in Figure 2.2. The dimensionless variable y can

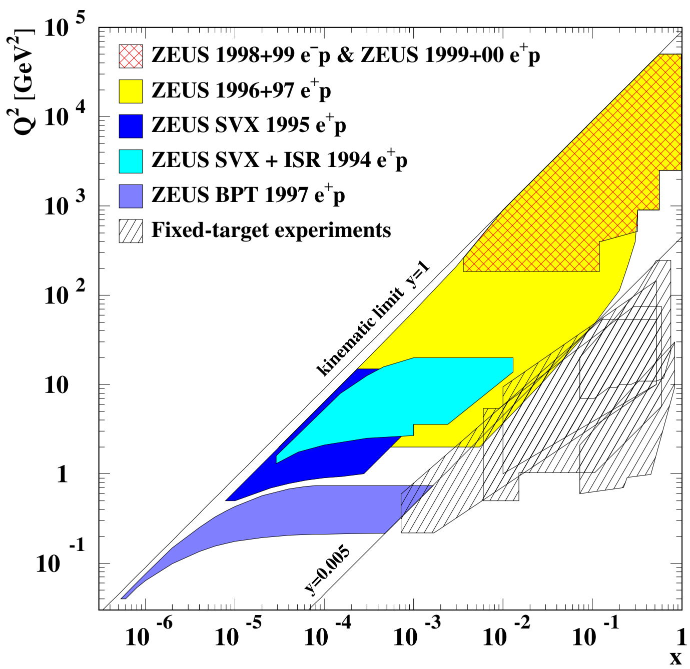

Figure 2.2: (Q^2, x)-plane covered by HERA and fixed target experiments.

be interpreted as an inelasticity parameter of the interaction. In the proton rest system it measures the fraction of the energy from the electron transferred to the hadronic system, hence it is defined in the range $0 \leq y \leq 1$. x is the dimensionless Bjorken scaling variable, which can be interpreted in the quark parton model as the fraction of the proton momentum carried by the massless parton interacting with the lepton, thus $0 \leq x \leq 1$. Due to momentum conservation only three out of these four variables are independent. By neglecting the lepton and nucleon masses the parameters Q^2, x, y and s are related to each other through:

$$Q^2 = x \cdot y \cdot s. \tag{2.5}$$

Processes in which the exchanged boson is a highly virtual photon or a Z^0 boson and Q^2 is typically much higher than $1\,\mathrm{GeV}^2$ are called neutral current (NC) DIS processes. Those where the exchanged boson is a highly virtual $W^{\pm}$ boson are called charged current (CC) DIS processes. Due to the $W^{\pm}$ boson exchange instead of an scattered electron an electron-neutrino is found in the final state.

2.2.1 Quark Parton Model

In the quark parton model (QPM) the proton is considered to consist of a accumulation of non-interacting point-like quarks and gluons, also called partons. In this model the DIS process can be considered as an elastic scattering of the electron with a single massless quark carrying the fraction x of the proton momentum (see Figure 2.3). The hardness or the resolving power of the interaction

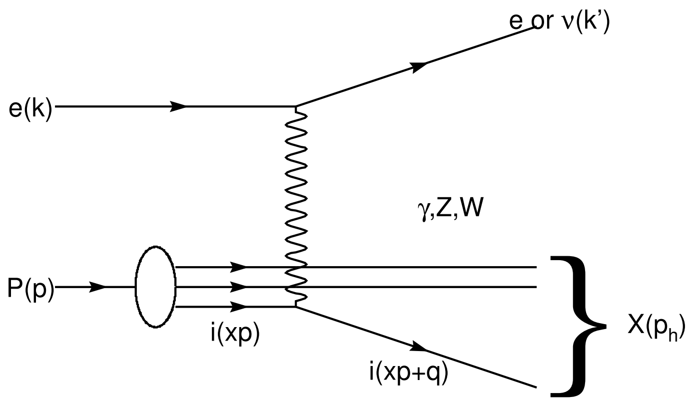

Figure 2.3: The quark parton model.

corresponds to the virtuality of the exchanged vector boson. As the boson virtuality increases, it probes smaller transverse distance scales and is able to resolve the structure of the proton. Therefore one of the main interests in DIS processes is to test the interaction of quarks and gluons within the proton and to probe the proton structure down to the 10^{-16} cm scale.

2.2.2 Cross Sections & Structure Functions

In the QPM the double differential Born cross section for the CC DIS process $e^{\pm}p \rightarrow \nu X$ using unpolarised beams can be expressed in terms of the structure functions F_2, F_L and F_3:

$$\begin{aligned}\frac{\mathrm{d}^2\sigma^{CC}_{\mathrm{Born}}}{\mathrm{d}x\mathrm{d}Q^2} &= \frac{G_F^2}{4\pi x}\frac{M_W^4}{(Q^2+M_W^2)^2}\times \\ &\{Y_+F_2^{CC}(x,Q^2) - y^2F_L^{CC}(x,Q^2) \mp Y_-xF_3^{CC}(x,Q^2)\},\end{aligned} \tag{2.6}$$

where $Y_\pm = 1 \pm (1-y)^2$, G_F is the Fermi coupling constant and M_W is the mass of the $W^\pm$ boson. Similarly, the cross section for the NC DIS process $e^\pm p \to e^\pm X$ reads as:

$$\begin{aligned}\frac{\mathrm{d}^2\sigma^{NC}_{\mathrm{Born}}}{\mathrm{d}x\mathrm{d}Q^2} &= \frac{2\pi\alpha_{\mathrm{em}}^2}{xQ^4}\times \\ &\{Y_+F_2^{NC}(x,Q^2) - y^2F_L^{NC}(x,Q^2) \mp Y_-xF_3^{NC}(x,Q^2)\},\end{aligned} \tag{2.7}$$

where α_{em} is the electromagnetic fine structure constant. The structure function F_2^{em} [2] as a function of Q^2 for fixed values of x as measured by different experiments can be seen in Figure 2.4.

For $x \approx 0.2$, F_2^{em} is approximately independent of Q^2. This behaviour of F_2 is called scaling. At high x, the cross section is sensitive only to the valence quarks. The density of the valence quarks falls with increasing Q^2 due to gluon radiation, resulting in scaling violation and a decrease of the cross section. At low x, gluon radiation leads to more gluons and quark anti-quark pairs in the proton, also leading to scaling violation and an increase of the cross section.

2.2.3 Parton Density Functions

In the QPM the DIS cross section is calculated as an incoherent sum of that of the elastic scatterings of the partons, which constitute the proton, as shown in Figure 2.3. The distribution of partons cannot be calculated from first principles within perturbative QCD. Thus, a separation of the short-range part (hard process) from the long-range part (soft process) is introduced (factorisation theorem), in order to factorise the cross section into a calculable term corresponding to the hard subprocess and the parton density functions (PDF). At present, the latter cannot be calculated and has to measured in experiments. The cross sections are obtained by a convolution of the two parts. Hence, in terms of the PDFs the cross sections are given by:

$$\frac{\mathrm{d}^2\sigma^{CC}}{\mathrm{d}x\mathrm{d}Q^2} = \frac{G_F^2}{2\pi}\frac{M_W^4}{(Q^2+M_W^2)^2}\times\sum_{i=1,2}\{\bar{u}_i(x,Q^2)+(1-y)^2d_i(x,Q^2)\}, \tag{2.8}$$

$$\frac{\mathrm{d}^2\sigma^{NC}}{\mathrm{d}x\mathrm{d}Q^2} = \frac{2\pi(\alpha_{\mathrm{em}})^2}{xQ^4}\times\sum_{i=1,2}\{\bar{u}_i(x,Q^2)+d_i(x,Q^2)\}, \tag{2.9}$$

[2] F_2^{em} is the purely electromagnetic part of F_2.

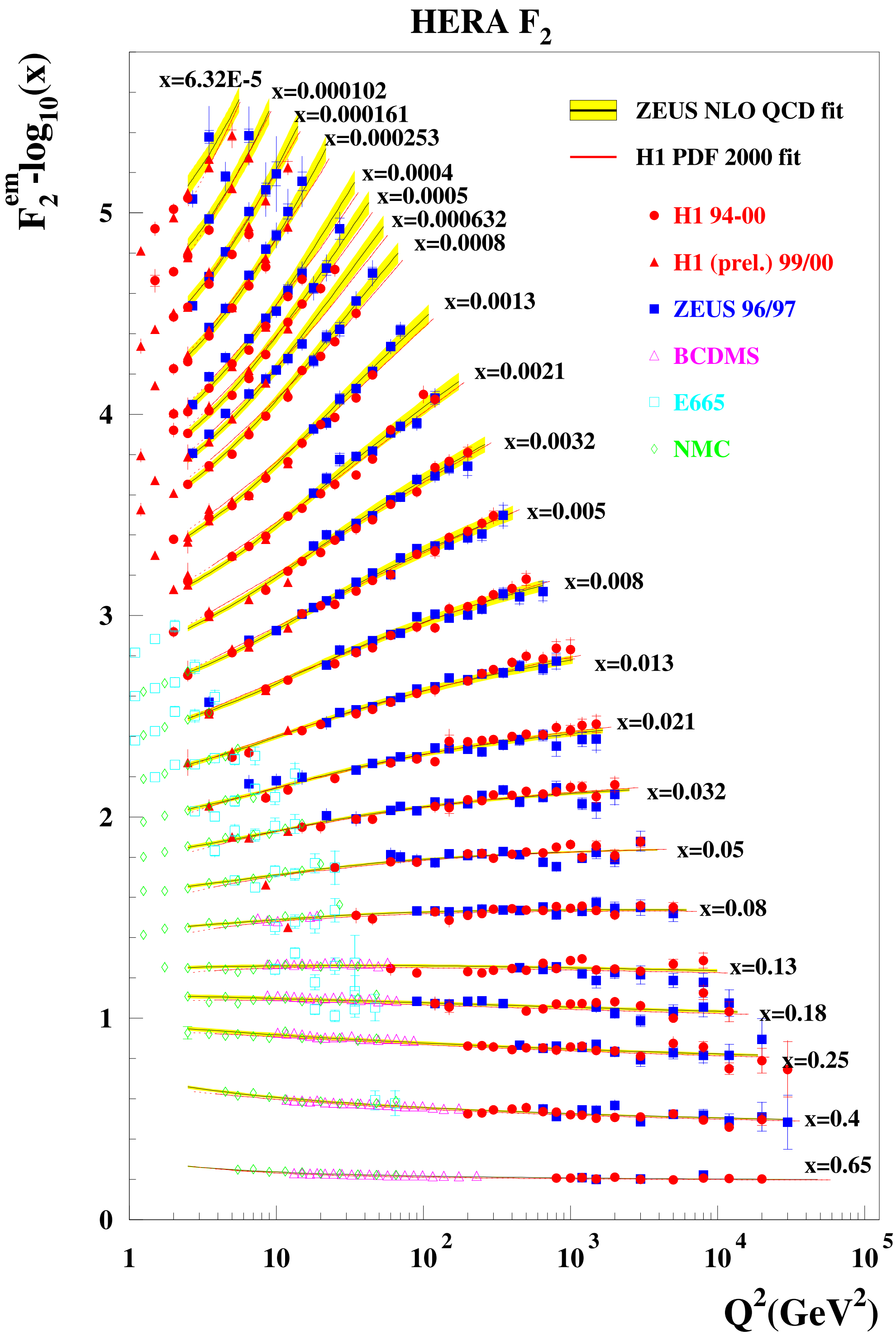

Figure 2.4: The structure function $F_2^{\rm em}$ measured by different experiments as a function of Q^2 in different bins of x.

for e^+p, and

$$\frac{\mathrm{d}^2\sigma^{\mathrm{CC}}}{\mathrm{d}x\mathrm{d}Q^2} = \frac{G_F^2}{2\pi}\frac{M_W^4}{(Q^2+M_W^2)^2} \times \sum_{i=1,2}\{u_i(x,Q^2)+(1-y)^2\bar{d}_i(x,Q^2)\}, \quad (2.10)$$

$$\frac{\mathrm{d}^2\sigma^{\mathrm{NC}}}{\mathrm{d}x\mathrm{d}Q^2} = \frac{2\pi(\alpha_{\mathrm{em}})^2}{xQ^4} \times \sum_{i=1,2}\{u_i(x,Q^2)+\bar{d}_i(x,Q^2)\}, \quad (2.11)$$

for e^-p collisions, respectively.

The u_i is the PDF for up-type quarks and d_i for down-type quarks with i running over the two lightest generations, assuming that the contributions from b- and t-quarks in the proton are negligible. $u_i(x, Q^2)$ gives the probability of finding a quark of the type u_i in the proton, with momentum fraction x at a given Q^2. Figure 2.5 shows the cross section measurements for CC and NC DIS. At low

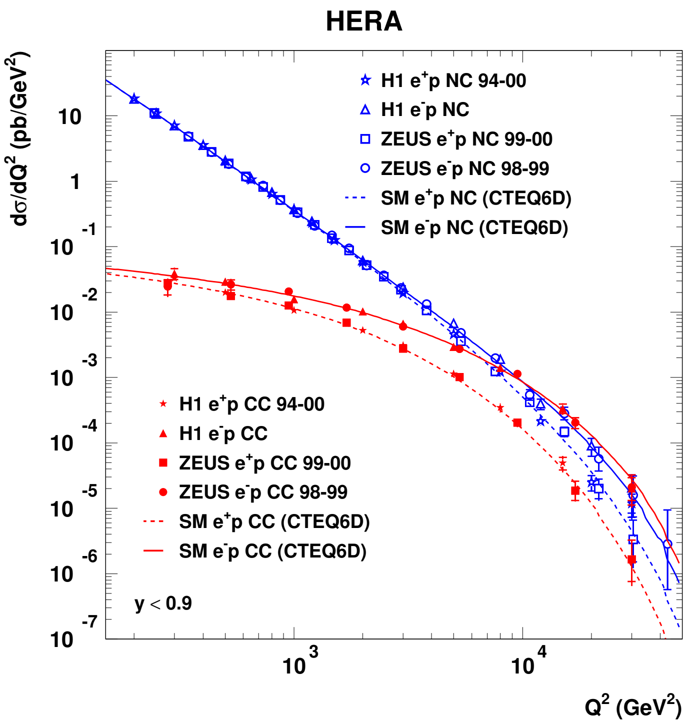

Figure 2.5: Differential cross section for NC and CC DIS as a function of Q^2.

$Q^2 \ll M_Z^2$ the cross section is dominated by photon exchange. The exchange of the Z^0 and $W^\pm$ bosons is suppressed by their large masses. The CC DIS cross section in e^-p interactions are larger than the one in e^+p interactions, since the density of the up quark is in general higher than that of the down quark (see Figure 2.6). The cross section difference increases towards higher Q^2, which reflects by contributions from valence quarks at higher x. Additionally, the kinematic factor $(1-y)^2$ suppresses the (anti-)quark contribution to the CC DIS cross section for e^+p (e^-p).

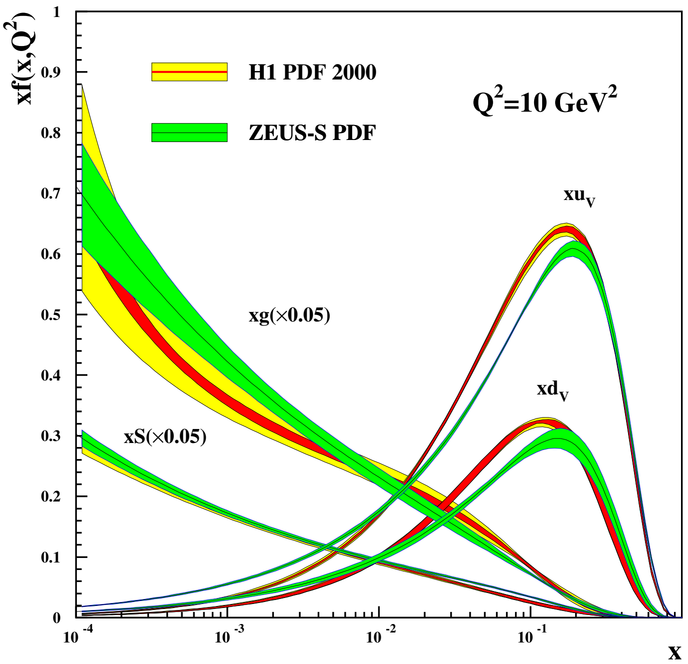

Figure 2.6: Parton density functions extracted from NLO calculations by H1 and ZEUS.

2.3 Photoproduction

Photoproduction processes (γp) are characterised by an exchange of a quasi-real photon ($Q^2 \approx 0$) between the incoming electron and the hadronic system. It is the dominant process at HERA with a total cross section of approximately $150 - 200\,\mu$b [13]. Most of the interactions are soft, i.e. the transverse energy of the final state particles is too small to be observed in the detector. However, jets at high transverse energies can be produced by hard photon-parton and parton-parton interactions. They provide a good testing ground for perturbative QCD and can give insights into the structure of the photon. In general there are two types of hard photoproduction subprocesses: Direct and resolved photoproduction.

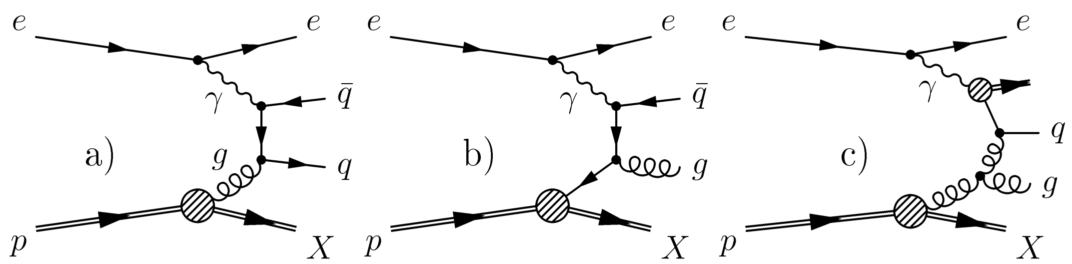

Figure 2.7: Example diagrams for boson-gluon fusion (a), QCD Compton (b) and resolved photoproduction (c).

In direct γp interactions the photon couples as a point-like particle to a parton from the proton. Two examples for direct photoproduction processes are boson-gluon fusion (BGF) (see Figure 2.7a) and QCD Compton (see Figure 2.7b).

In resolved processes, the photon fluctuates into quark anti-quark pairs, where one of the quarks carrying a fraction of the total photon momentum interacts with a parton from the proton (an example diagram is shown in Figure 2.7c).

2.4 Di-Lepton Production

The dominant source for lepton pair production at HERA is the Bethe-Heitler process. Small contributions to di-lepton production can also come from the QED Compton process and Z^0 radiation.

In the Bethe-Heitler process $ep \to \gamma\gamma \to \ell^+\ell^-$ (see Figure 2.8a) a quasi-real photon is emitted from the electron and interacts with a photon radiated from a quark inside the proton. The two photons fuse to a lepton anti-lepton pair like e^+e^-, $\mu^+\mu^-$ or $\tau^+\tau^-$. The total cross section for inclusive $e^+e^- \to \ell^+\ell^-$ interactions is relatively large: $\sim 150\,\text{pb}$, but falls steeply with increasing transverse momenta of the produced leptons [14]. The phase space for lepton pair production can be divided into three regions, defined by the momentum transfer squared Q^2 and the invariant mass M_X of the produced hadronic final state.

In the elastic region, the hadronic final state X consists only of the scattered proton, which stays intact in the scattering process, i.e. $M_X = M_p$.

In the quasi-elastic region the proton does not stay intact during the scattering process, but is transformed into an excited nucleon state, which decays into a nucleon and mostly pions, i.e. $M_X > M_p$.

In the inelastic region the proton breaks off and many hadrons are produced, i.e. $M_X \gg M_p$. In this region the momentum transfer between the incoming proton and the final state hadronic system is large, usually more than a few GeV^2.

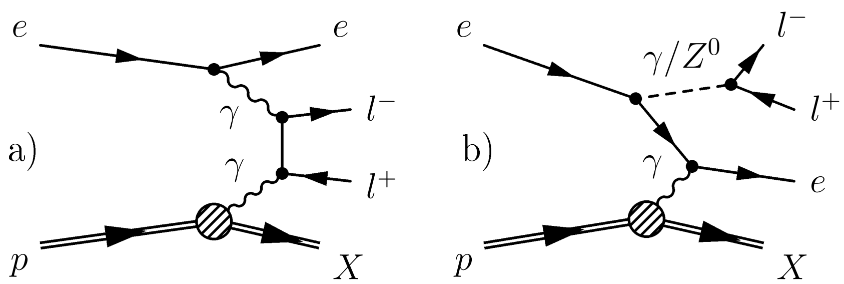

Figure 2.8: Example diagrams for di-lepton production in Bethe-Heitler (a) and QED Compton/Z^0 radiation processes (b).

Figure 2.8b shows an example for the QED Compton (Z^0 radiation) process:

A photon from internal photon conversion of the initial electron can decay into lepton pair. Alternatively, Z^0 bosons are produced in initial state radiation and subsequently decay into a lepton pair. The total cross section for these processes is expected to be small ($\lesssim 0.1\,\text{pb}$).

2.5 Single W Boson Production

Single $W^\pm$ boson production $ep \to eWX$ is the most important source for $W^\pm$ bosons at HERA. The dominant contribution to the single W Boson $ep \to eWX \to el\nu X$ cross section arises from the graph in Figure 2.9a, where a quasi-real photon and a massless quark are exchanged in a u-channel configuration. Another example diagram contains the $WW\gamma$ (WWZ) triple-gauge-boson coupling, as shown in Figure 2.9b. The total cross section has been estimated to be of the order of 1 pb [15].

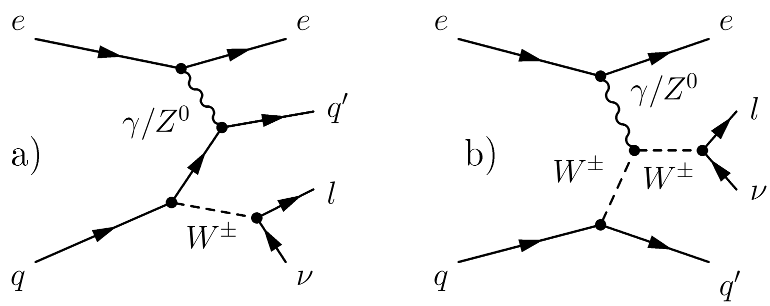

Figure 2.9: Two example diagrams for single W boson production, where the $W^\pm$ subsequently decays into leptons.

2.6 Limitations of the Standard Model

The SM has been tested at many high energy physics experiments with very high accuracy and the agreement between the SM predictions and the measurements is magnificent. Yet, only the evidence for the Higgs boson is missing. However, some theoretical aspects indicate that the SM is not a complete theory[3]. Some of the most fundamental questions are left unexplained by the SM. As mentioned before, the SM does not incorporate the gravitational force, and, hence, is no candidate for a theory which unifies all known forces. Another severe issue is the hierarchy problem. Why is the Planck scale so much larger than the electroweak scale? The Planck mass is defined as $M_P = \sqrt{8\pi G} \approx 10^{19}\,\text{GeV}$, where G is the gravitational constant. The Planck scale is the energy scale where the gravitational interactions of elementary particles become comparable to those of

[3]The SM is not expected to be valid at all energy scales.

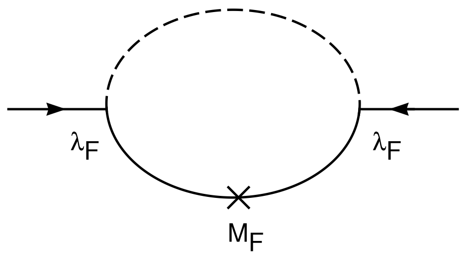

Figure 2.10: Radiative correction to the Higgs mass. The example loop show the coupling of the Higgs boson with a fermion.

gauge interactions. Radiative corrections to the Higgs mass lead to quadratically divergent vacuum correction terms (see Figure 2.10) and spoil the hierarchy. A fine tuning of the coupling constants is needed for a very accurate cancellation of these divergencies.

Supersymmetry (SUSY) can solve these problems. It provides a framework for the unification of quantum field theory and gravity at the Planck scale and also gives a solution for the hierarchy problem, or fine tuning problem.

Chapter 3

Supersymmetry

3.1 Basic Elements of Supersymmetry

SUSY is a generalisation of spacetime symmetries in quantum field theory. Its operators transform fermions into bosons and vice versa (for a review on SUSY see [16]):

$$Q \ |\text{fermion}\rangle \ = |\text{boson}\rangle \ \text{ and } \ Q \ |\text{boson}\rangle \ = |\text{fermion}\rangle, \tag{3.1}$$

where Q is an operator which acts on fermionic and bosonic states. Q must satisfy the following commutator and anti-commutator algebra:

$$\{Q, Q^\dagger\} = P^\mu \tag{3.2}$$

$$\{Q, Q\} = \{Q^\dagger, Q^\dagger\} = 0 \tag{3.3}$$

$$[P^\mu, Q\} = \{P^\mu, Q^\dagger] = 0 \tag{3.4}$$

Here, P^μ denotes the 4-momentum operator. The irreducible representations of the SUSY algebra contain single particle states, called supermultiplets, of both fermion and boson states. Since the generators Q and $Q^\dagger$ commute with the momentum operator and the generators of the SM gauge transformations, the superpartners should have the same mass, electric charge, weak isospin and colour, but different spin. The contribution of the superpartners to the radiative corrections leads to a cancellation of all quadratic divergences in all orders. This means, the contribution from fermion loops are cancelled by the ones from boson loops because of an additional factor (-1) coming from Fermi statistics, as illustrated in Figure 3.1. From experimental observations we know that the particles and their superpartners cannot be degenerate in mass. Hence, SUSY cannot be an exact symmetry and must be broken.

Probably one of the best argument why SUSY is expected to be the most promising theory beyond the SM is the fact that simplest SUSY models lead to unification of all known forces at an energy scale of $\sim 10^{16}$ GeV. A unification of

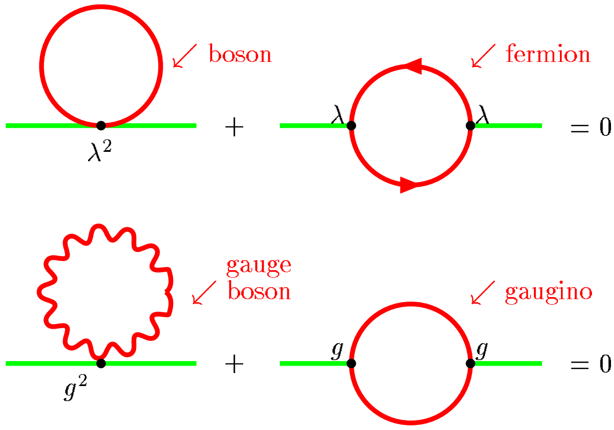

Figure 3.1: Cancellation of the quadratic divergencies in the radiative corrections to the Higgs mass.

the coupling constants cannot be obtained in the SM (see Figure 3.2). A perfect unification can be obtained if the SUSY masses are at the order of 1 TeV. Above this energy scale the effective contribution of the SUSY particles to the running of the coupling constants[1] becomes significant and causes a change in the slope of the lines.

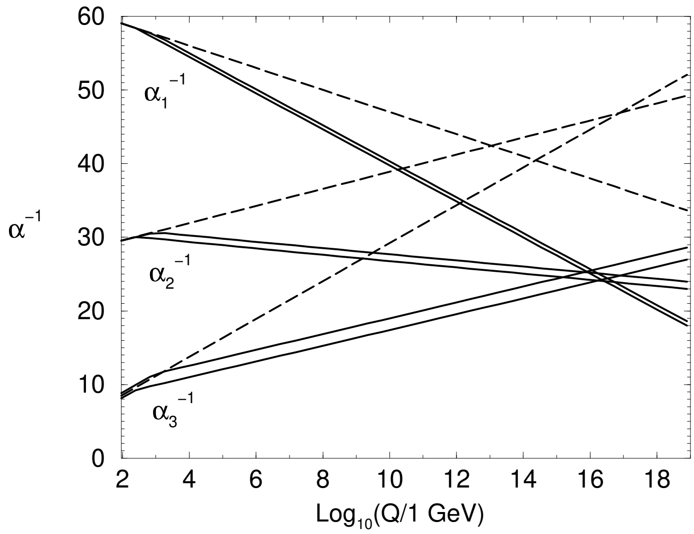

Figure 3.2: RG evolution of the inverse coupling constants in the SM (dashed lines) and in a SUSY model (solid lines). The thickness of the lines represents the error on the coupling constants.

[1]The running of the coupling constants results from radiative corrections coming from loop diagrams. These corrections are scale dependent and can be calculated using the renormalisation group (RG) equations which treat the couplings and masses as running parameters.

3.2 The Minimal Supersymmetric Standard Model

The Minimal Supersymmetric extension of the Standard Model (MSSM) is defined to be consistent with the SM gauge group and contains the SM particles and their superpartners. However, two Higgs doublets are needed in order to give mass to down-type and up-type[2] quarks. Table 3.1 gives an overview of the MSSM superfields, the corresponding supermultiplets and their properties. R-parity is assumed to be conserved (will be discussed in Section 3.3) and finally, the most general soft-supersymmetry-breaking terms has to be added. Soft-breaking means that the cancellation of quadratic divergencies must not be destroyed by the breaking mechanism. There are different proposals for realistic models of SUSY breaking. Most of them favour spontaneous SUSY breaking over explicit SUSY breaking. Two examples are gravity mediated SUSY breaking in the framework of minimal supergravity (mSUGRA) and gauge mediated SUSY breaking (GMSB). Details about these models can be read in [16].

The Yukawa-like terms of the MSSM superpotential are given by

$$W_{\mathrm{MSSM}} = y^u_{ij} Q_i \bar{U}_j H_u + y^d_{ij} Q_i \bar{D}_j H_d + y^l_{ij} L_i \bar{E}_j H_d + \mu H_d H_u, \tag{3.5}$$

where the objects $Q, L, \bar{E}, \bar{U}, \bar{D}, H_u, H_d$ are the chiral superfields and the dimensionless Yukawa-type coupling parameters $y^u_{ij}, y^d_{ij}, y^l_{ij}$ are 3×3 matrices in family space. i, j are family indices and the μ term is the supersymmetric version of the Higgs boson mass in the SM. The superfield notation in Equation (3.5) include all possible interactions between the Higgs bosons and the particles of the MSSM. Not shown are the interaction terms from gauge invariance.

The gauge eigenstates of the SUSY particles are not always the mass eigenstates. The relations between gauge and mass eigenstates are summarised in Table 3.2. In general, the left- and right-handed squarks and sleptons are not mass eigenstates, since there is $\tilde{f}_L - \tilde{f}_R$ mixing. The nature of this mixing is complicated and depends on many parameters. However, it turns out that in the case of three generations the first two generation sfermions are usually almost degenerate in mass. But for the third generation, squark and slepton mixing can lead to a light and a heavy mass eigenstate, in particular at large $\tan\beta$ which is defined as the ratio of the vacuum expectation values of the up-like and the down-like neutral higgsinos ($\tan\beta = v_u/v_d$). In the MSSM all squark and slepton masses can be treated as free parameters.

Since the MSSM contains two complex Higgs doublets, there are five Higgs mass eigenstates: The two CP-even neutral Higgses (h, H), the CP-odd neutral one (A) and the charged ones ($H^{\pm}$). Their masses depend on the Higgs mixing parameters M_{H_u}, M_{H_d}, μ and $\tan\beta$.

[2]The term 'down-type' quarks refers to the down, strange and bottom quark and their anti-particles, whereas 'up-type' quarks refers to the up, charm and top quark and their anti-particles.

Superfield	**Fermions**	Spin	**Bosons**	Spin	**Group Symmetry**
Gauge:					
G^a	gluino ($\tilde{g}$)	1/2	gluon (g)	1	(8, 0, 3)
G^k	winos ($\tilde{W}^{\pm}$,$\tilde{W}^0$)	1/2	W bosons ($W^{\pm}$)	1	(1, 3, 0)
V'	bino ($\tilde{B}^0$)	1/2	B boson (B^0)	1	(1, 1, 0)
Matter:					
	quarks		squarks		
Q_i	$(u^i\ d^i)_L$	1/2	$(\tilde{u}^i\ \tilde{d}^i)_L$	0	(3, 2, $\frac{1}{3}$)
$\bar{U}_i$	u^i_R	1/2	$\tilde{u}^i_R$	0	(3, 1, -$\frac{4}{3}$)
$\bar{D}_i$	d^i_R	1/2	$\tilde{d}^i_R$	0	(3, 1, $\frac{2}{3}$)
	leptons		sleptons		
L_i	$(e^i\ \nu^i)_L$	1/2	$(\tilde{e}^i\ \tilde{\nu}^i)_L$	0	(1, 2, -1)
$\bar{E}_i$	e^i_R	1/2	$\tilde{e}^i_R$	0	(1, 1, 2)
Higgs:					
H_u	$(\tilde{H}^+_u\ \tilde{H}^0_u)$	1/2	$(H^0_u\ H^+_u)$	0	(1, 2, -1)
H_d	$(\tilde{H}^0_d\ \tilde{H}^-_d)$	1/2	$(H^-_d\ H^0_u)$	0	(1, 2, 1)

Table 3.1: Particle content of the MSSM, where $a = 1, ..., 8$ and $k = 1, 2, 3$ are the SU(3)$_c$ and SU(2)$_\mathrm{L}$ indices, respectively, and $i = 1, 2, 3$ is the family index. The group symmetry refers to the transformation properties of the supermultiplet under the SM gauge group SU(3)$_c$ $\times$ SU(2)$_\mathrm{L}$ $\times$ U(1)$_\mathrm{Y}$.

	Spin	**R-parity**	**Mass Eigenstates**	**Gauge Eigenstates**
gluino	1/2	-1	$\tilde{g}$	- " -
neutralinos	1/2	-1	$\tilde{\chi}^0_{1,...,4}$	$\tilde{B}^0\ \tilde{W}^0\ \tilde{H}^0_u\ \tilde{H}^0_d$
charginos	1/2	-1	$\tilde{\chi}^{\pm}_{1,2}$	$\tilde{W}^{\pm}\ \tilde{H}^+_u\ \tilde{H}^-_d$
squarks			$\tilde{u}_L\ \tilde{u}_R\ \tilde{d}_L\ \tilde{d}_R$	- " -
	0	-1	$\tilde{c}_L\ \tilde{c}_R\ \tilde{s}_L\ \tilde{s}_R$	- " -
			$\tilde{t}_1\ \tilde{t}_2\ \tilde{b}_1\ \tilde{b}_2$	$\tilde{t}_L\ \tilde{t}_R\ \tilde{b}_L\ \tilde{b}_R$
sleptons			$\tilde{e}_L\ \tilde{e}_R\ \tilde{\nu}_e$	- " -
	0	-1	$\tilde{\mu}_L\ \tilde{\mu}_R\ \tilde{\nu}_\mu$	- " -
			$\tilde{\tau}_1\ \tilde{\tau}_2\ \tilde{\nu}_\tau$	$\tilde{\tau}_L\ \tilde{\tau}_R\ \tilde{\nu}_\tau$
Higgs bosons	0	$+1$	$h^0\ H^0\ A^0\ H^{\pm}$	$H^0_u\ H^0_d\ H^{\pm}_u$

Table 3.2: Mass eigenstates of the superpartners.

3.2.1 Gaugino Sector

Because of the great importance of the neutralino and the chargino sector for this search, the gaugino sector will be discussed in more detail in the following.

Of direct interest for the phenomenology of SUSY at experiments are the supersymmetric gauge interactions. Production and decay of superpartners are usually dominated by the gauge coupling strength. Example diagrams for the interaction of the gauginos with fermion pairs are shown in Figure 3.3. The mass eigenstates

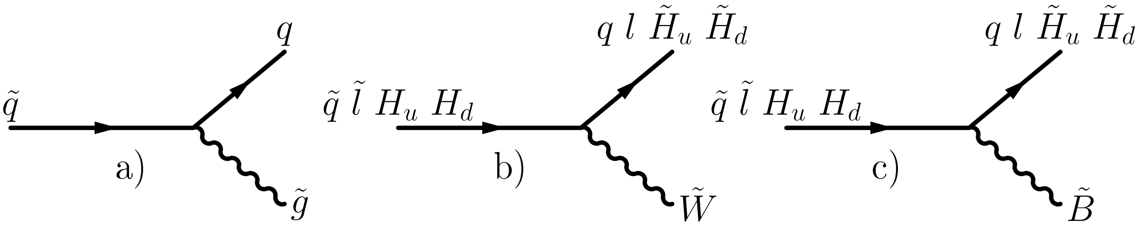

Figure 3.3: Interactions of the gluino (a), wino (b) and bino (c) with scalar with fermion pairs.

of the gauginos are called neutralinos, charginos and the gluino. The gluino ($\tilde{g}$) is the fermion partner of the gluon with mass $M_{\tilde{g}} = M_3$. There are four neutralino states formed by the mixing of the bino, the neutral wino and the two neutral higgsinos. The neutralino mass eigenstates are denoted as $\tilde{\chi}^0_{1,..,4}$, where the indices are defined by mass ordering: $M_{\tilde{\chi}^0_1} < M_{\tilde{\chi}^0_2} < M_{\tilde{\chi}^0_3} < M_{\tilde{\chi}^0_4}$. The four chargino states contain the charged winos and the charged higgsinos. These mass eigenstates are denoted as $\tilde{\chi}^\pm_{1,2}$, with $M_{\tilde{\chi}^\pm_1} < M_{\tilde{\chi}^\pm_2}$. The corresponding mixing matrix for the neutralinos with the basis ($\tilde{B}^0$, $\tilde{W}^0$, $\tilde{H}^0_d$, $\tilde{H}^0_u$) is given by

$$M_{\tilde{\chi}^0_i} = \begin{pmatrix} M_1 & 0 & -M_Z\ c_\beta\ s_W & M_Z\ s_\beta\ s_W \\ 0 & M_2 & M_Z\ c_\beta\ c_W & -M_Z\ s\beta\ c_W \\ -M_Z\ c_\beta\ s_W & M_Z\ c_\beta\ c_W & 0 & -\mu \\ M_Z\ s_\beta\ s_W & -M_Z\ s_\beta\ c_W & -\mu & 0 \end{pmatrix}, \tag{3.6}$$

where s_W (c_W) is the sine (cosine) of the weak mixing angle and s_β (c_β) denotes $\sin\beta$ ($\cos\beta$). M_1, M_2 and M_3 are the supersymmetric mass breaking terms associated with the gauge group $\mathrm{SU(3)}_c \times \mathrm{SU(2)_L} \times \mathrm{U(1)_Y}$. The mixing matrix for the charginos with the basis ($\tilde{W}^+$, $\tilde{H}^+_u$, $\tilde{W}^-$, $\tilde{H^-}_d$) is given by

$$M_{\tilde{\chi}^\pm_i} = \begin{pmatrix} 0 & X^T \\ X & 0 \end{pmatrix}, \tag{3.7}$$

with

$$X = \begin{pmatrix} M_1 & M_W\ \sqrt{2}\ \sin\beta \\ M_W\ \sqrt{2}\ \cos\beta & -\mu \end{pmatrix}. \tag{3.8}$$

If one assumes that the gauge couplings unify at the scale $\sim 10^{16}$ GeV, a relation between M_1, M_2 and M_3 can be obtained from the RG equations which is called the GUT (Grand Unified Theory) relation and which is often used to reduce the number of free parameters. At the electroweak scale this relation becomes

$$M_1 = \frac{5}{3} M_2 \tan^2\theta_W = \frac{5}{3}\frac{\alpha_{\mathrm{em}}}{\alpha_s}\frac{M_3}{\cos^2\theta_W} \approx \frac{1}{2} M_2 \approx \frac{1}{7} M_3 \tag{3.9}$$

If one applies the relation in Equation (3.9) to substitute M_1 in Equations (3.6)–(3.8), one can immediately see that the gaugino masses depend only on three unknown parameters: μ, M_2 and $\tan\beta$. In general, gauginos are heavier the larger $|\mu|$ and M_2 and the shape of the mass contours in the (μ, M_2)-plane depend on $\tan\beta$, as can be seen in Figure 3.4.

For a better understanding of the phenomenology in the gaugino sector one characterises the gauginos by their dominant gauge eigenstate component. Usually the mixing basis is changed for this purpose. Analogous to the mixing of the B^0, W^0 and $W^{\pm}$ bosons to form the photon, the Z^0 boson and the $\mathrm{W}^{\pm}$ bosons in the SM, one can apply the corresponding mixing to the superpartners. In this way the gauginos can be characterised by their photino ($\tilde{\gamma}$), zino ($\tilde{z}$), wino ($\tilde{w}$) and higgsino ($\tilde{h}$) content, which strongly affects the interaction of the gauginos with other particles. The gauge eigenstate content depends as well as the masses on the three unknown parameters μ, M_2 and $\tan\beta$. Hence, the (μ, M_2)-plane can be divided into different regions with different dominant gauge states, as shown in Figure 3.5.

In general, the nature of the gauginos has the same effect on the interaction as known for SM gauge bosons. A pure photino, in contrary to a zino or wino, does not interact weakly, hence, it does not couple to electrically neutral particles like a neutrino or a sneutrino. On the other hand, pure higgsinos predominantly couple to heavy particles.

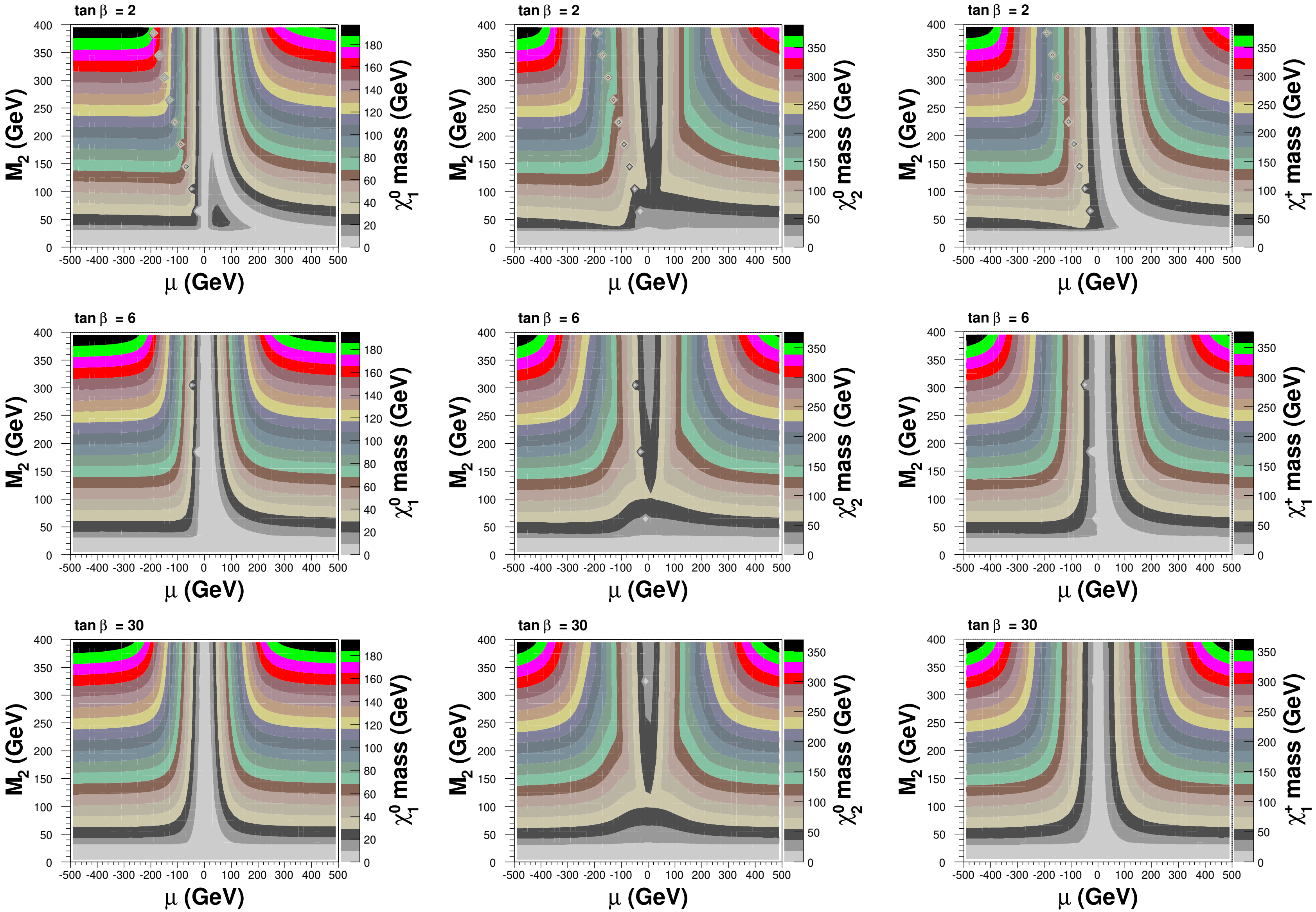

Figure 3.4: The masses of $\tilde{\chi}^0_{1,2}$ and $\tilde{\chi}^\pm_1$ in the (μ, M_2)-plane for $\tan\beta = 2, 6, 30$.

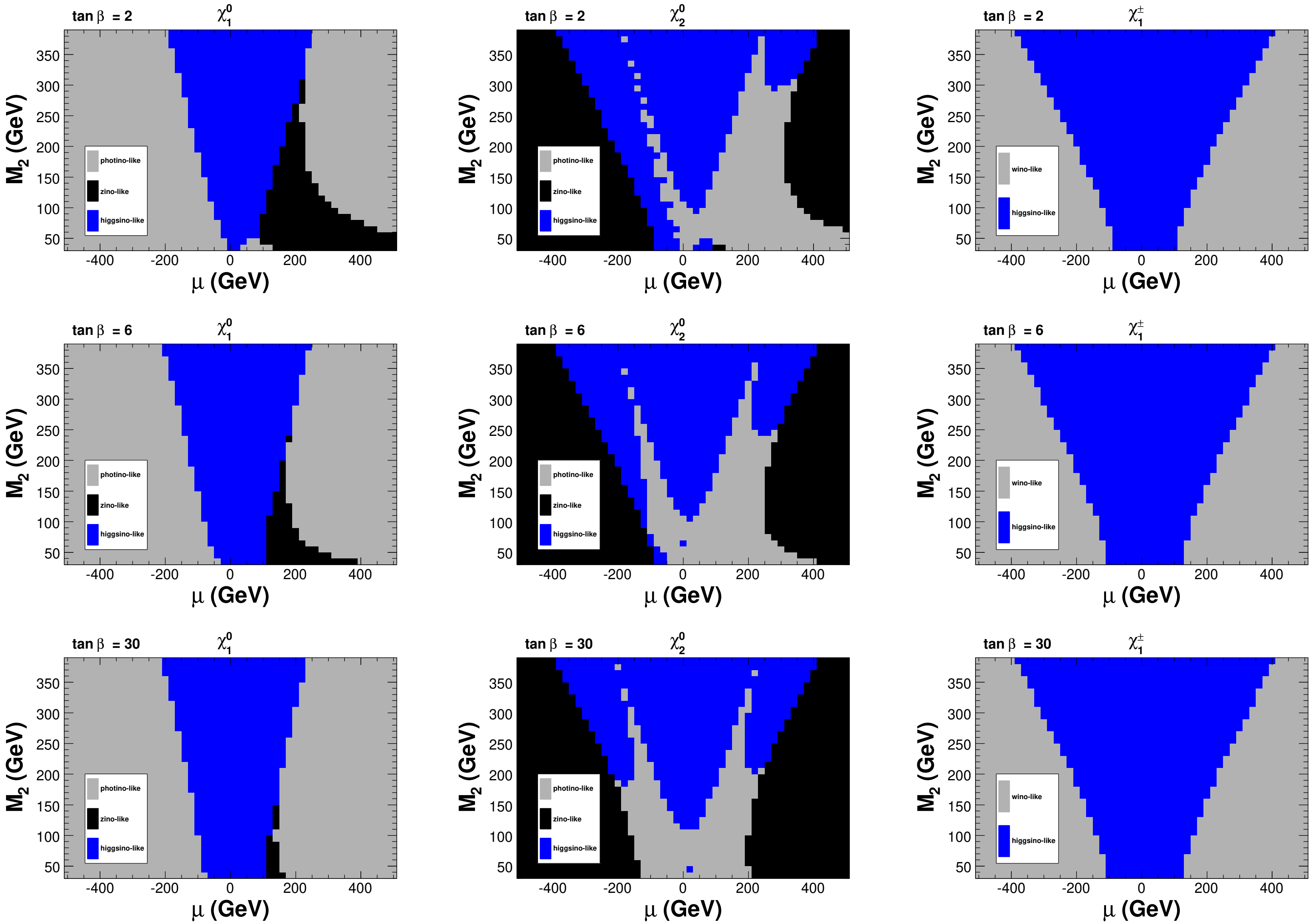

Figure 3.5: Regions in the (μ, M_2)-plane characterised by the dominant gauge eigenstate content of $\tilde{\chi}^0_{1,2}$ and $\tilde{\chi}^\pm_1$ for $\tan\beta = 2, 6, 30$.

3.3 R-parity

R-parity (R_p) is a discrete multiplicative symmetry defined by $R_p = (-1)^{3B+L+2S}$, where B is the baryon number, L the lepton number and S the spin of the particle. SM particles including the Higgs bosons have R-parity +1, while all SUSY particles have R-parity −1. R-parity conserving (RPC) SUSY is well-motivated by the hope that the lightest supersymmetric particle (LSP) will provide a promising candidate for non-baryonic dark matter. It has important phenomenological consequences:

- In collider experiments SUSY particles can only be produced in pairs.
- The LSP is absolute stable. If the LSP is electrically neutral it can only interact weakly with ordinary matter which makes it a good candidate for cold dark matter. The signature for a LSP in the detector would be missing energy.
- Each SUSY particle other than the LSP would eventually decay into a final state with an odd number of LSPs. Also this would lead to an energy imbalance in the detector.

However, the most general supersymmetric Lagrangian does not exclude R_p violating terms explicitely. Non-conservation of R_p allows for additional terms in the superpotential:

$$W_{\not R_P} = \lambda_{ijk} L_i L_j \bar{E}_k + \lambda'_{ijk} L_i Q_j \bar{D}_k + \lambda''_{ijk} \bar{U}_i \bar{D}_j \bar{D}_k \ + \mu'_i L_i H_u, \tag{3.10}$$

where λ_{ijk}, λ'_{ijk} and λ''_{ijk} are Yukawa coupling constants and i, j, k denote family indices. The first two terms and the fourth term in Equation (3.10) violate lepton number conservation, while the third term violates conservation of baryon number. Hence, the phenomenology in $\not R_P$ SUSY scenarios are very different from the one in RPC models:

- Single production of SUSY particles is possible.
- The LSP is not absolute stable and can decay into SM particles. In this case the LSP is no candidate for cold dark matter anymore.
- The number of possible experimental signatures increases significantly.

For more details about $\not R_P$ SUSY one can find a detailed review in [17].

3.4 R-parity violating Supersymmetry at HERA

At HERA leading order and next-to-leading order diagrams proceed through the second term in Equation (3.10). The very compact superfield notation can be expanded and the corresponding Lagrangian for the $L_i Q_j \bar{D}_k$ term becomes

$$\mathcal{L}_{L_i Q_j \bar{D}_k} = \lambda'_{ijk} \quad \{ \quad \tilde{\nu}^i_L d^j_L \bar{d}^k_R - \tilde{e}^i_L u^j_L \bar{d}^k_R + \nu^i_L \tilde{d}^j_L \bar{d}^k_R - e^i_L \tilde{u}^j_L \bar{d}^k_R + \tag{3.11}$$

$$(\bar{\nu}^i_L)^c \bar{d}^j_L \tilde{d}^{k*}_R - (\bar{e}^i_L)^c \bar{u}^j_L \tilde{d}^{k*}_R \ \} + h.c., \tag{3.12}$$

where the superscript ^{c} denote the charge conjugate spinors and the * the complex conjugate of scalar fields.

3.4.1 Gaugino Production

At electron-proton colliders the interaction terms in Equation (3.11) can lead to tree-level diagrams with a quark and a gaugino in the final state. According to the Mandelstam notation, these diagrams can be classified in s-channel, u-channel (for neutralino production only) and t-channel processes. In the s-channel the resonant production of squarks is possible which can subsequently decay into a gaugino and a quark. The u-channel is characterised by a squark exchange, whereas one has an exchange of a slepton in the t-channel. Two example Feynman diagrams for neutralino and chargino production in the t-channel at HERA are shown in Figure 3.6. Neutralinos can be produced via an exchange of a left-handed electron which interacts with a right-handed down-like quark or a left-handed up-like quark, dependent on the charge of the initial electron. In the case of chargino production the exchanged slepton is a left-handed sneutrino which interacts with a left- or right-handed down-like quark.

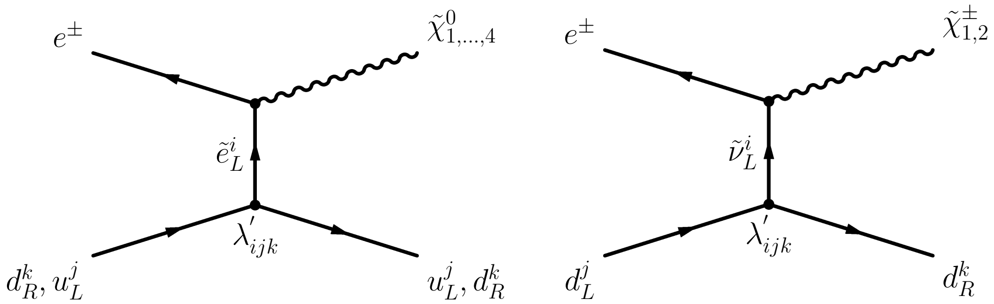

Figure 3.6: Example t-channel diagrams for neutralino (a) and chargino production (b) at HERA.

Neutralino and Chargino Production

The cross section for neutralino and chargino production at the parton level has been calculated by H. Dreiner and J. Butterworth in [2]. In the case where the initial state consists of $e^+ + d^k$ and the neutralino is pure photino-like, taking into account the pure t-channel contributions only[3] , the following relation for the differential cross section has been derived:

$$\frac{\mathrm{d}\sigma(e^+d^k \to u^j\tilde{\chi}_n^0)}{\mathrm{d}t} \propto \frac{\lambda'^2}{s^2} \cdot \frac{(t-M_u^2)(t-M_{\tilde{\chi}}^2)}{(t-M_{\tilde{e}}^2)^2}, \tag{3.13}$$

where the Mandelstam variables s and t correspond to the square of the centre of mass energy and the square of the momentum transfer in the exchange process, respectively.

For chargino production and in the case the initial state consists of $e^+ + d^k$, taking into account the pure t-channel contributions only, the relation for the differential cross section reads as:

$$\frac{\mathrm{d}\sigma(e^+d^k \to d^j\tilde{\chi}_n^+)}{\mathrm{d}t} \propto \frac{\lambda'^2}{s^2} \cdot \frac{(t-M_d^2)(t-M_{\tilde{\chi}}^2)}{(t-M_{\tilde{\nu}}^2)^2} \tag{3.14}$$

For light sleptons and heavy squarks the contribution of the t-channel process to the total cross section for gaugino production is dominant. The programme SUSYGEN [18] is used to calculate the cross sections for HERA. In SUSYGEN the above differential cross sections are convoluted with the density of the incoming quark within the proton. The cross section contributions as a function of the slepton mass of the different subprocesses in e^+p and e^-p collisions, respectively, are depicted in Figure 3.7. A sample point in the parameter space is chosen which roughly corresponds to a photino-like $\tilde{\chi}_1^0$ with a mass of 58 GeV which is above the existing limit of 32.5 GeV from the LEP experiment L3 [19][4]. In e^+p collisions the valence quark contribution for chargino production is dominant, while the sea quark contribution for chargino production is suppressed. On the other hand in e^-p neutralino production is dominant and the valence quark contribution for chargino production is suppressed, but since the probability to find a up quark within the proton is about two times higher than to find a down quark, the total cross section is slightly higher in electron-proton collisions than in positron-proton collisions.

The cross section for gaugino production also depends on the mass of the gaugino and its gauge state content. An illustration for the behaviour of the different contributions in different parameter space regions is given in Figure 3.8. Figure 3.8a-b shows the region where the neutralinos have dominant photino content and the chargino dominant wino content . Similar results, but not shown, were obtained in regions where the neutralinos are more zino-like. In the region where the $\tilde{\chi}_1^0$ and the chargino both have dominant higgsino content, but the $\tilde{\chi}_2^0$ is photino-like (see Figure 3.8c-d), the cross section for $\tilde{\chi}_1^0$ and $\tilde{\chi}_1^\pm$ is suppressed, since the higgsino Yukawa coupling strength with light (s)leptons becomes small.

---

[3] Contributions from the s- and u-channel as well as the t-s and t-u interference terms are not shown in Equations (3.13)–(3.14).

[4] The $\tilde{\chi}_1^0$ mass limit presented in [19] was derived for large sfermion masses and a large $\tan\beta$ range ($0.7 \geq \tan\beta \geq 40$), assuming that only one λ_{ijk}, λ'_{ijk} or $\lambda''{}_{ijk}$ coupling is non-zero.

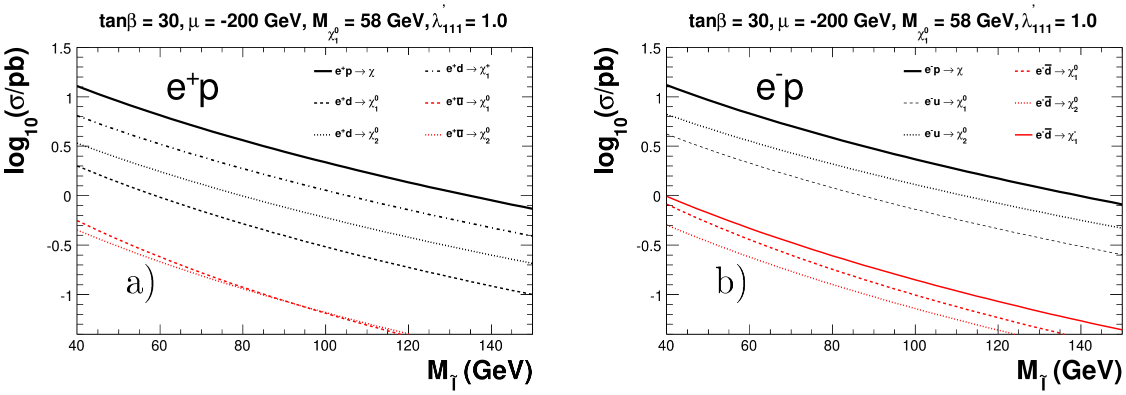

Figure 3.7: Total Cross section and contributions from valence and sea quarks as a function of the slepton mass for neutralino and chargino production at HERA for e^+p (a) and e^-p (b) collisions. The chosen point in the parameter space roughly corresponds to a photino-like neutralino.

In summary, the cross section decreases for increasing neutralino, chargino and slepton masses. The total cross section in e^-p collisions becomes more dominant over the one in e^+p collisions as the neutralino mass gets larger.

3.4.2 Gaugino Decays

The gaugino decays depend strongly on the gauge eigenstate content of the gaugino in question and on the Yukawa coupling strength λ'. If λ' is not too small ($\gtrsim 0.25$), the $\not{R}_P$ three-body decays (see Figure 3.9) will usually dominate. The gauginos can decay into an slepton lepton pair, where the slepton subsequently decays via λ' into two quarks (see Figure 3.9a,b,d,e). Or the gauginos decay into a $q\tilde{q}$ pair, where the squark subsequently decays via λ' into a quark and a lepton (see Figure 3.9c,f). Also the three-body gauge decays (see Figure 3.10a,b) and $q\tilde{q}$ ($\ell\tilde{\ell}$) pair decays (see Figure 3.10c,d) are possible. However they are are suppressed if λ' is large. A neutralino can decay into a Z^0 boson and a lighter neutralino which subsequently decays into a fermion pair (for example see Figure $3.10a : \tilde{\chi}^0_m \rightarrow \tilde{\chi}^0_n f f,\ n > 1,\ n < m$). A chargino can decay into a $W^\pm$ boson and a neutralino which subsequently decays into a fermion pair (for example see Figure $3.10b : \tilde{\chi}^\pm_m \rightarrow \tilde{\chi}^0_n f f$). A chargino or neutralino can also decay into a $q\tilde{q}$ ($\ell\tilde{\ell}$) pair, where the squark (slepton) subsequently decays into quark and a gaugino (see Figure 3.10c,d).

It has been shown that the $\not{R}_P$ decays of the neutralino and the chargino is dominant, if $\lambda' \gtrsim 0.25$ [20]. The decay rates of the neutralino and the gaugino has been discussed extensively by H. Dreiner et al. in [21] and [22]. In the

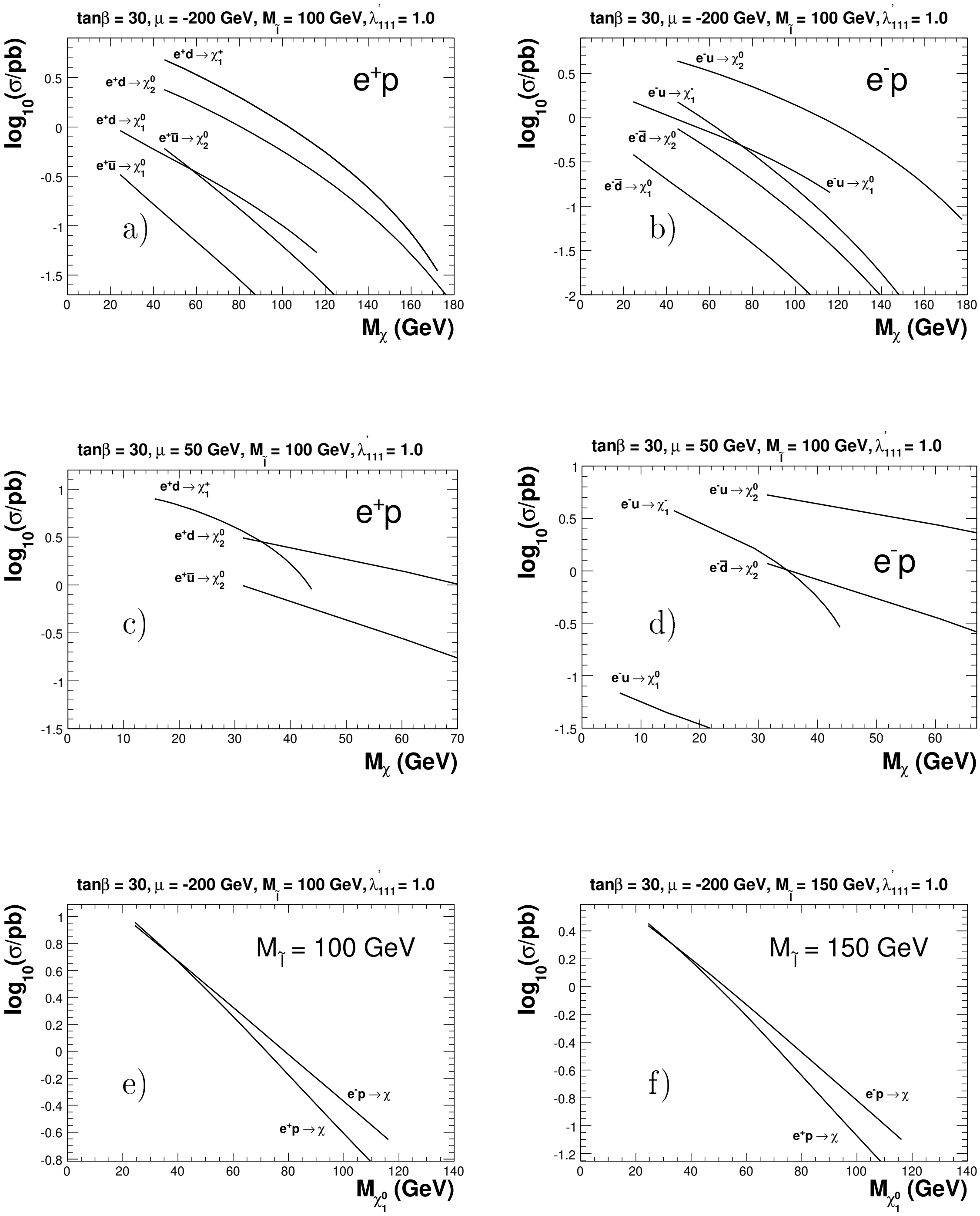

Figure 3.8: Cross sections for gaugino production as a function of the gaugino mass in different regions of the parameter space.

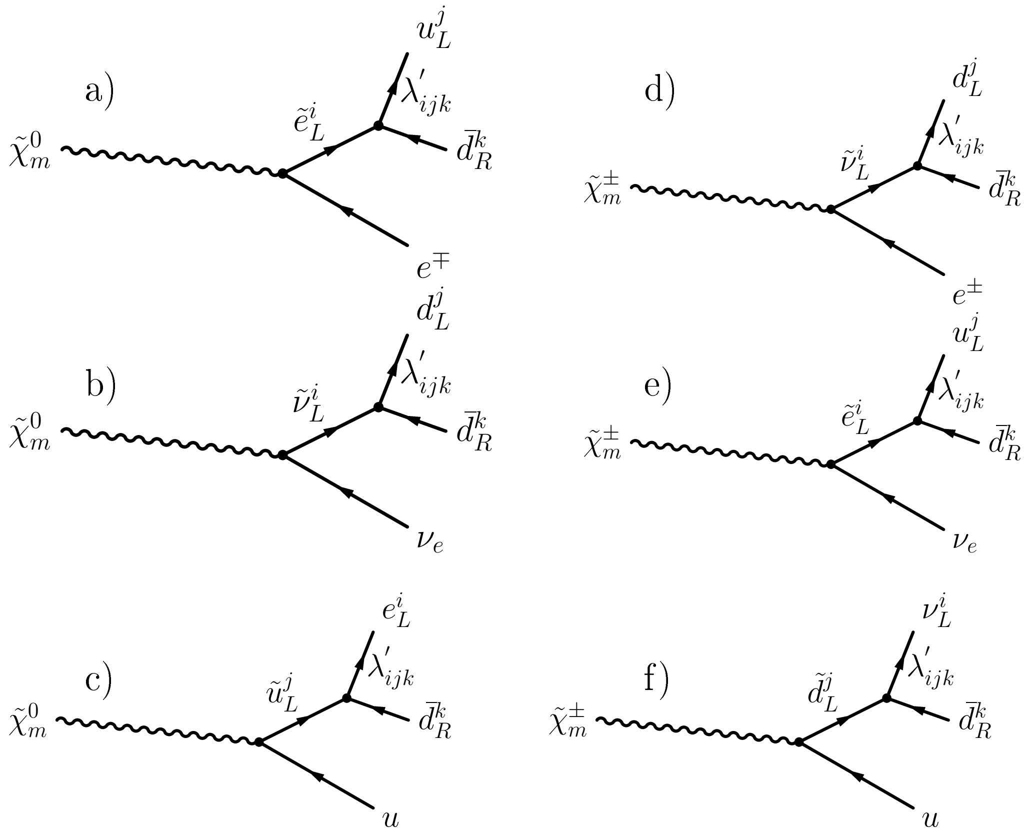

Figure 3.9: Example diagrams for the $\not{R}_P$ three-body decays of the neutralinos (a-c) and the charginos (d-f).

following the results are illustrated for characteristic regions in the parameter space.

Figure 3.11 shows the branching ratios for the $\not{R}_P$ three-body decays of the $\tilde{\chi}^0_1$ as a function of $\tan\beta$ at fixed M_2 and in four bins of μ. In Figure 3.11a the lower $\tan\beta$ region correspond to photino-like neutralinos. Since there is no coupling of the photino with a neutrino or a sneutrino, the BR for the neutrino decay is suppressed. As $\tan\beta$ grows the zino-component of the neutralino increases and the neutrino decay channel becomes available. At $\mu = 400\,\mathrm{GeV}$ (see Figure 3.11b) the situation is the other way around. At low $\tan\beta$ the neutralinos starts with large zino content and becomes more and more photino-like as $\tan\beta$ rises. At $\mu = 200\,\mathrm{GeV}$ (see Figure 3.11c) the zino content of the neutralino is even more dominant than in the latter case. Figure 3.11d shows a situation where the higgsino part dominates and the zino content is small, but still much larger than the negligibly small photino content. Similar arguments can be applied to explain the evolution of the BRs for $\tilde{\chi}^0_2$ (see Figure 3.12) and $\tilde{\chi}^{\pm}_1$ (see Figure 3.13) based on Figure 3.5, except for one difference: The influence of the gauge decays causes

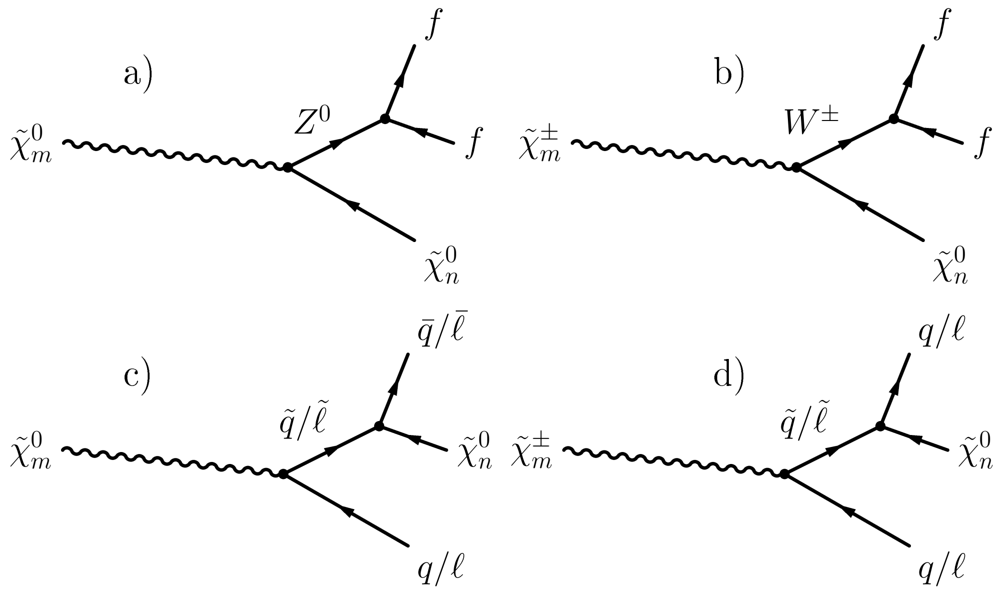

Figure 3.10: Example diagrams for the gauge decays (a-b) and the $q\tilde{q}$ ($\ell\tilde{\ell}$) decays (c-d) of the neutralinos and charginos.

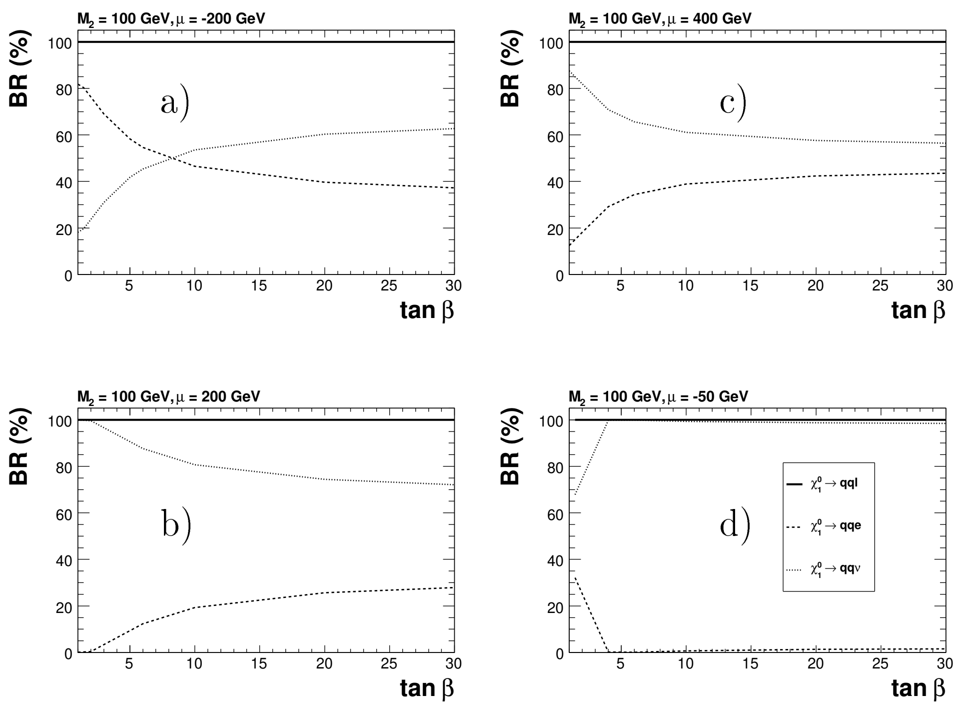

Figure 3.11: Branching ratios for the $\not{R}_P$ three-body decays of the $\tilde{\chi}^0_1$ in different regions of the parameter space. The full line indicates the sum of the dashed and the dotted line.

the drop of the total BR ($\tilde{\chi} \to qq\ell$) in some regions. In addition, there is one remark for an almost pure higgsino-like LSP. In this case the total decay width

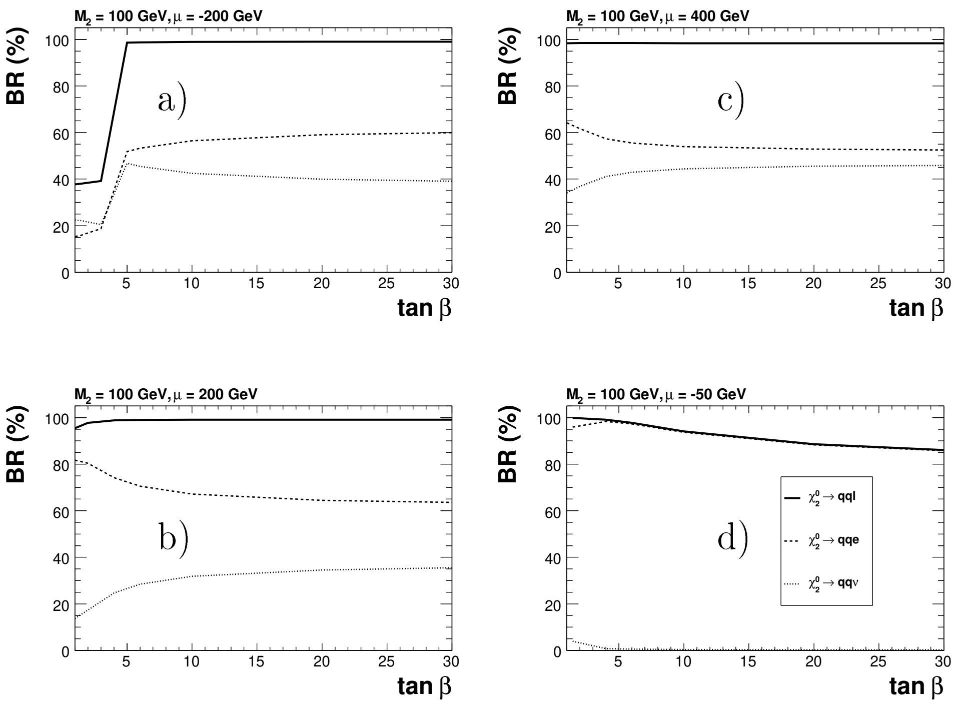

Figure 3.12: Branching ratios for the $\not{R}_P$ three-body decays of the $\tilde{\chi}^0_2$ in different regions of the parameter space. The full line indicates the sum of the dashed and the dotted line.

can become so small that it decays outside of the detector [21].

3.5 Summary

In this thesis a search for neutralino and chargino production via a t-channel exchange of a slepton is performed. The exchange of the slepton violates R-parity via an $L_i Q_j \bar{D}_k$ operator and the slepton is assumed to be a left-handed selectron or a sneutrino. The framework is the R-parity violating MSSM.

The R-parity conserving MSSM has 124 unknown parameters, including the 28 parameters from the SM. R-parity violating adds another 48 unknown Yukawa coupling constants. Apparently, it is crucial to reduce the number of free parameters significantly. The following constraints are assumed, in order to minimise the parameter space under study:

- Only one λ'_{1jk} is dominant, while all other $\not{R}_P$ couplings are negligibly small. The strength of the dominant λ'_{1jk} is a free parameter in this search.

- All squarks are degenerate in mass and there are no large mixings in the third family.

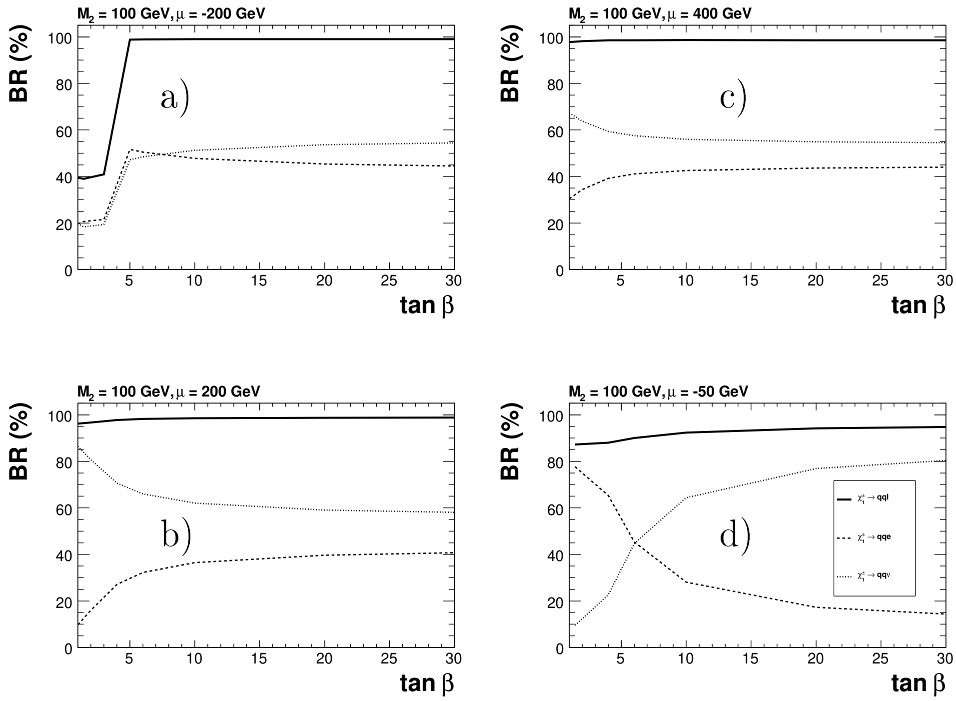

Figure 3.13: Branching ratios for the $\not{R}_P$ three-body decays of the $\tilde{\chi}_1^{\pm}$ in different regions of the parameter space. The full line indicates the sum of the dashed and the dotted line.

- The selectrons and sneutrinos are degenerate in mass and are much lighter than the squarks (this suppresses s- and u-channel contributions). The selectron (sneutrino) mass is treated as a free parameter in this analysis.
- The GUT relation in Equation (3.9) is applied, so that the gaugino masses depend only on μ, M_2 and $\tan\beta$. These parameters are treated as free variables in this analysis.
- Only the production of $\tilde{\chi}_1^0$, $\tilde{\chi}_2^0$ and $\tilde{\chi}_1^{\pm}$, are considered. All other gauginos including the gluino are too heavy to have sizeable cross sections.
- λ'_{1jk} is chosen such that the $\not{R}_P$ three-body decays of the gauginos are dominant. The three-body gauge decays and $q\tilde{q}$ pair decays are suppressed in most of the parameter space under study, but are considered as well in this search, if the event has a topology listed in Table 3.3.
- Usually, the lightest neutralino is the LSP. Sometimes the selectron or the sneutrino is the LSP. This rare case is not considered explicitely in this search.
- The regions of the parameter space, where the gauginos have a large higgsino content is not in the reach of this search, since the coupling strength of a

higgsino with light (s)leptons is small. If pure higgsinos are produced, they have very likely a long lifetime and escape the detector unobserved. This leads to signatures with only one jet and missing P_T or with one jet, missing P_T and a lepton. These cases are not covered by this search.

All possible final state topologies which are considered in this analysis are summarised in Table 3.3. It should be noticed, that the electron channel is potentially characterised by a striking 'wrong sign' signature. In fifty percent of the cases the final electron can have a different charge than the initial electron. This striking signature is expected to be almost background free.

Gaugino Decay	**Final State**	**Signature**
$\tilde{\chi}^0_{1,2} \rightarrow e^{\pm} qq$	$e^{\pm} qqq$	$e^{\pm}$ + multi-jets
$\tilde{\chi}^0_{1,2} \rightarrow \nu qq$	νqqq	missing P_T + multi-jets
$\tilde{\chi}^0_2 \rightarrow \tilde{\chi}^0_1 qq$ $\hookrightarrow \tilde{\chi}^0_1 \rightarrow e^{\pm} qq$	$e^{\pm} qqqqq$	$e^{\pm}$ + multi-jets
$\tilde{\chi}^0_2 \rightarrow \tilde{\chi}^0_1 qq$ $\hookrightarrow \tilde{\chi}^0_1 \rightarrow \nu qq$	$\nu qqqqq$	missing P_T + multi-jets
$\tilde{\chi}^{\pm}_1 \rightarrow e^{\pm} qq$	$e^{\pm} qqq$	$e^{\pm}$ + multi-jets
$\tilde{\chi}^{\pm}_1 \rightarrow \nu qq$	νqqq	missing P_T + multi-jets
$\tilde{\chi}^{\pm}_1 \rightarrow \tilde{\chi}^0_1 qq$ $\hookrightarrow \tilde{\chi}^0_1 \rightarrow e^{\pm} qq$	$e^{\pm} qqqqq$	$e^{\pm}$ + multi-jets
$\tilde{\chi}^{\pm}_2 \rightarrow \tilde{\chi}^0_1 qq$ $\hookrightarrow \tilde{\chi}^0_1 \rightarrow \nu qq$	$\nu qqqqq$	missing P_T + multi-jets

Table 3.3: All final state topologies considered in this thesis.

Chapter 4

Experimental Setup

4.1 The HERA Collider

HERA is a worldwide unique facility, since it accelerates both leptons and protons and brings them to collision [23]. Located at the DESY (Deutsches Elektron-Synchrotron) laboratory in Hamburg, Germany, HERA has been built in the years between 1984 – 1990 and is operating since 1992. The electrons (positrons) and protons are accelerated in two separated storage rings with circumferences of about 6.3 km each. Normal conducting magnets with a field strength up to

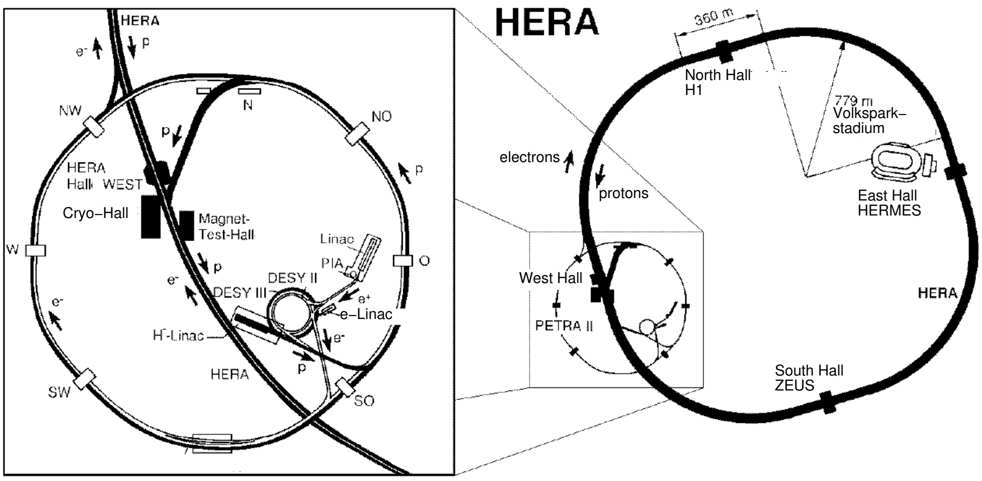

Figure 4.1: Schematic view of the HERA rings and the pre-accelerators.

0.165 T are used in the electron ring, whereas superconducting magnets with a field strength up to 4.65 T are used to form the proton beam. At two points along the circumference the two beam pipes merge into one providing electron-proton collisions for the experiments H1 and ZEUS. The two other experiments which are located at HERA, named HERMES and HERA-B, operate in the fixed-target mode, using the electron beam and the proton beam, respectively. HERA-B has stopped operation in the year 2003. A schematic picture of the HERA storage rings and the pre-accelerator-system is shown in Figure 4.1.

The electrons can be accelerated up to an energy of 27.5 GeV and the protons up to an energy of 920 GeV which leads to a maximum centre of mass energy of 318 GeV. HERA started operation as an electron-proton collider with a proton energy of 820 GeV and an electron energy of 26.7 GeV. Since then HERA has been undergoing several upgrade schemes. In Table 4.1 the type of the interaction, the proton energy, the electron energy, the delivered luminosity and the luminosity useful for physics analysis for the different running periods are listed. An

Year	E_e(GeV)	E_p(GeV)	**delivered** $\mathcal{L}$(pb^{-1})	**Physics** $\mathcal{L}$(pb^{-1})
93 – 94 e^-p	26.7/27.5	820	7.3	4.8
94 – 97 e^+p	27.5	820	70.9	48.3
98 – 99 e^-p	27.5	920	25.2	16.71
99 – 00 e^+p	27.5	920	95.0	65.8
03 – 04 e^+p	27.5	920	84.5	40.6
04 – 05 e^-p	27.5	920	114.9	84.6

Table 4.1: Summary of the luminosities and the beam energies for the different running periods.

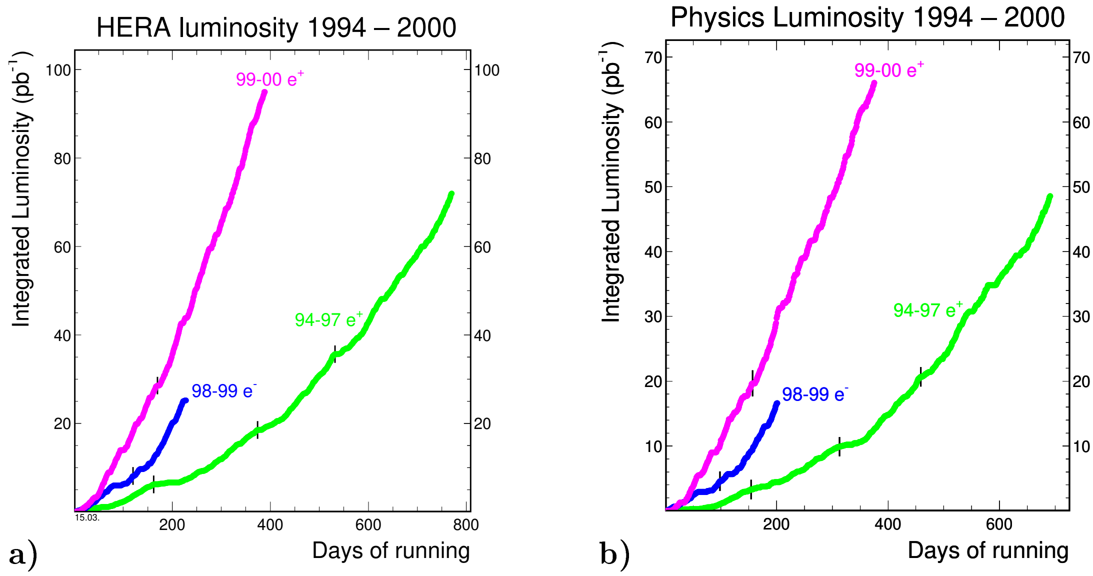

Figure 4.2: Integrated luminosity delivered by HERA (a) and integrated physics luminosity (b) as a function of running days for the periods from 1994 to 2000.

illustration of the delivered and the physics luminosity as a function of the days of data taking from 1994 – 2000 is shown in Figure 4.2. The design instantaneous luminosity at the interaction points is $\mathcal{L} = 1.6 \cdot 10^{31}\,\mathrm{cm}^{-2}\,\mathrm{s}^{-1}$ with a maximum number of 210 colliding bunches. In the years between 2000 and 2002 HERA was undergoing a major upgrade. The main goal of this upgrade was an increase of the luminosity by a factor of five. Also spin rotators have been installed in order to provide a longitudinally polarised lepton beam to the experiments [24]. After severe problems with high backgrounds at the beginning of the restart, the regular operation of HERA with stable beams has begun in 2003 (HERA II). Up to now HERA II has delivered $84.5\,\mathrm{pb}^{-1}$ of e^+p data and $114.9\,\mathrm{pb}^{-1}$ of e^-p data.

In this thesis the analysed data was taken in the years 1996 – 2000, which correspond to an integrated luminosity of $\mathcal{L} = 121.1\ \mathrm{pb}^{-1}$.

4.2 The ZEUS Detector

The ZEUS detector system was designed as a multi-purpose detector with nearly hermetic coverage. It consists of many components, so in the following sections only the detector parts which are most important for this analysis will be discussed in more detail. For further and more exhausting informations on the ZEUS detector see [25].

Until 1995 the vertex detector (VXD) was the detector nearest to the beam pipe, but it was removed during the 1995/1996 shutdown period. In 2001, a silicon-strip micro-vertex detector (MVD) has been installed and is now the innermost component of the ZEUS detector system. A drift chamber acts as the central tracking detector (CTD), complemented by the forward detector (FDET) and the rear tracking detector (RTD). For charge and momentum determination the tracking system is surrounded by a super-conducting solenoid providing a magnetic field up to $1.8\,\mathrm{T}$. The uranium calorimeter system is divided into a barrel part (BCAL), a forward part (FCAL) and a rear part (RCAL), which provides a nearly hermetic coverage. It is surrounded by a backing calorimeter (BAC), which measures late showering particles and additionally operates as magnetic yoke. The muon detector system consists of the parts located inside (FMUI, BMUI, RMUI) and outside (FMUON, BMUON, RMUON) the magnetic yoke. Figures 4.3 and 4.5 give a cross sectional view of the ZEUS detector along the beam pipe (r-z-view) and perpendicular to the beam pipe (x-y-view), respectively.
The ZEUS coordinate system (see Figure 4.4) is a right-handed Cartesian system, with the Z axis pointing in the proton beam direction, referred to as the 'forward direction', and the X axis pointing left towards the centre of HERA. The coordinate origin is at the nominal interaction point.

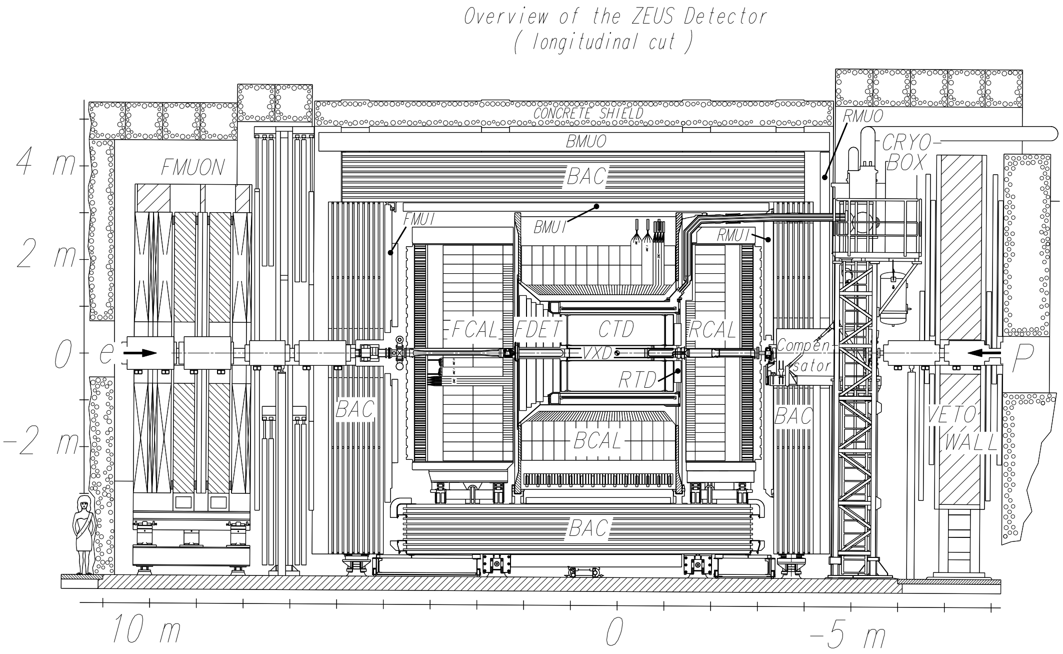

Figure 4.3: Cross sectional view of the ZEUS detector along the beam pipe.

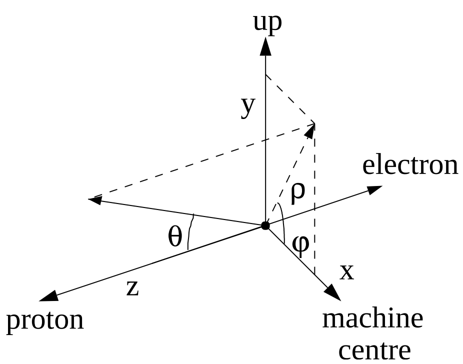

Figure 4.4: The ZEUS reference coordinate system.

4.2.1 The Calorimeter

The ZEUS detector is a uranium-scintillator calorimeter (CAL) [26] which is designed to have high resolution for both hadronic and electromagnetic energies. It consists of three parts: The forward calorimeter (FCAL), the barrel calorimeter (BCAL) and the rear calorimeter (RCAL), as depicted in Figure 4.6. The FCAL and the BCAL are divided into three layers - an electromagnetic segment (EMC) and two hadronic segments (HAC1, HAC2) - while the RCAL consists of one EMC and one HAC1. Each part consists of modules, towers and cells as can be seen in Figure 4.6 and Figure 4.7. The overall number of cells is nearly 6000 having inner dimensions in the range from $5 \times 20\,\mathrm{cm}^2$ to $24 \times 35\,\mathrm{cm}^2$ de-

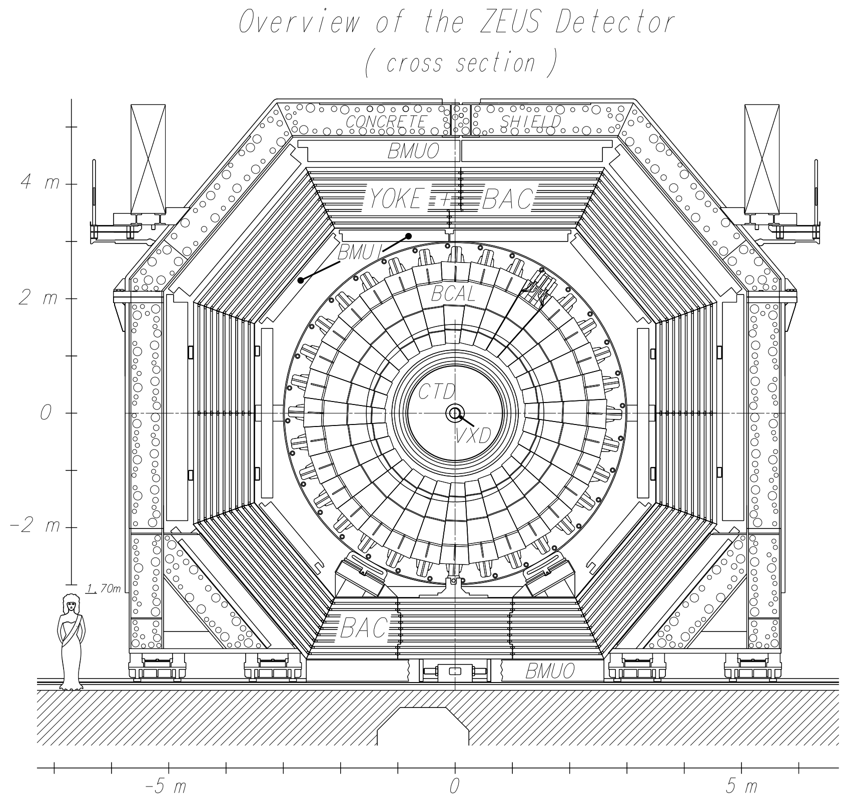

Figure 4.5: Cross sectional view of the ZEUS detector perpendicular to the beam pipe.

pending on the type and their position. Each cell consists of depleted uranium (98.1% U^{238}, 1.7% Nb, 0.2% U^{235}) plates as absorber alternated with organic scintillators (SCSN-38 polystyrene) as active material. The thickness of the absorber material and the active material have been chosen in order to be compensating, which means that the same response for an electron or a hadron of the same energy ($e/h = 1.00 \pm 0.02$) passing through the detector is achieved. The maximal depths of the HAC1 (HAC2) for the FCAL, the BCAL and the RCAL are $\sim 7\lambda$, $\sim 5\lambda$ and $\sim 4\lambda$, respectively, while the ones of the EMC are $\sim 26X_0$, $\sim 23X_0$ and $\sim 26X_0$. Here, λ is the hadronic absorption length and X_0 is the electromagnetic radiation length. The arrangement of the different calorimeter parts ensures a nearly hermetic coverage. The polar angular range covered by the calorimeter system is $2.5° < \theta < 178.4°$.

When a high energetic particle crosses a scintillator plate it can interact with the atoms and lift an electron to a higher energetic state. This electron will return after a characteristic time to its initial state by emitting light with a characteristic frequency spectrum. The light generated in the scintillator is collected on both sides of a module by wavelength shifters and is guided to the photomultiplier tubes, which converts it into an electronic signal. These information are used for

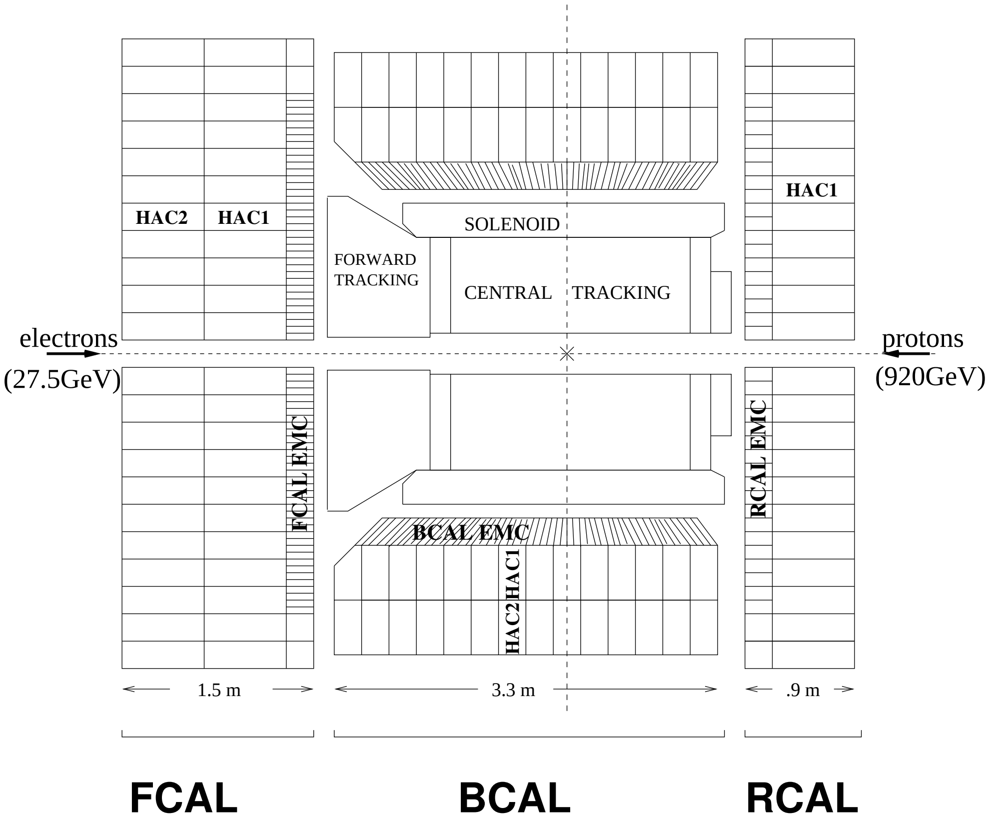

Figure 4.6: The different parts of the ZEUS calorimeter in a cross sectional view.

energy as well as for time measurement.

The CAL provides timing information of the order of 1 ns for tracks with an energy deposit of more than 1 GeV. The timing information of a particle with respect to the bunch crossing time can be used by the trigger algorithm to reject background events. The energy resolution of the calorimeter for electromagnetic and hadronic showers, measured under test beam conditions is

$$\frac{\sigma_{\mathrm{em}}(E)}{E} = \frac{18\%}{\sqrt{E\ (\mathrm{GeV})}} \oplus 1\% \tag{4.1}$$

and

$$\frac{\sigma_{\mathrm{h}}(E)}{E} = \frac{35\%}{\sqrt{E\ (\mathrm{GeV})}} \oplus 2\%, \tag{4.2}$$

respectively.

4.2.2 The Central Tracking Detector

The central tracking detector (CTD) [27] is a cylindrical wire chamber used to measure direction and momentum of charged tracks and to estimate the energy

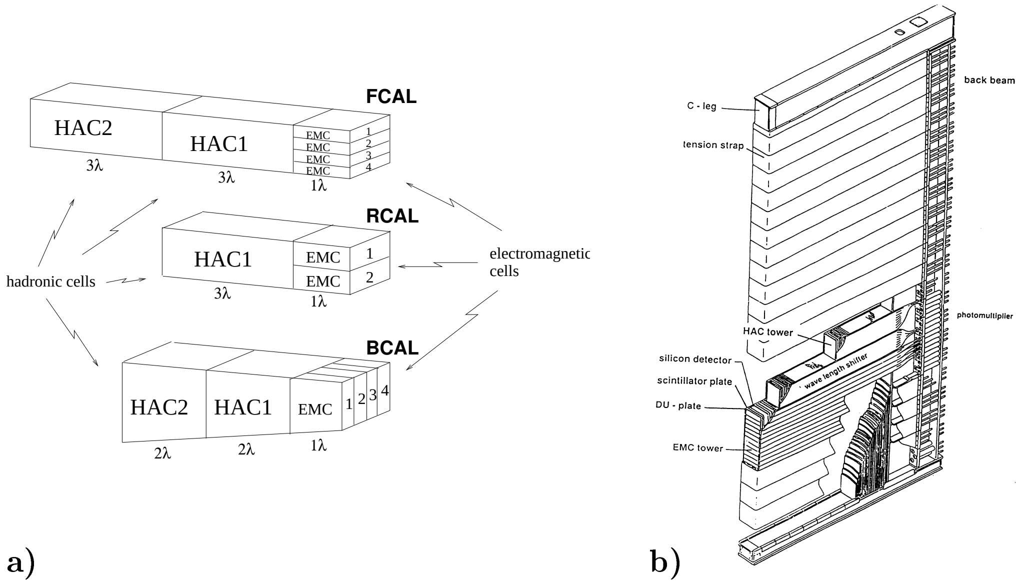

Figure 4.7: Towers from the different calorimeter parts (a) and a module from the FCAL (b).

loss dE/dx of charged particles to provide information on particle identification.

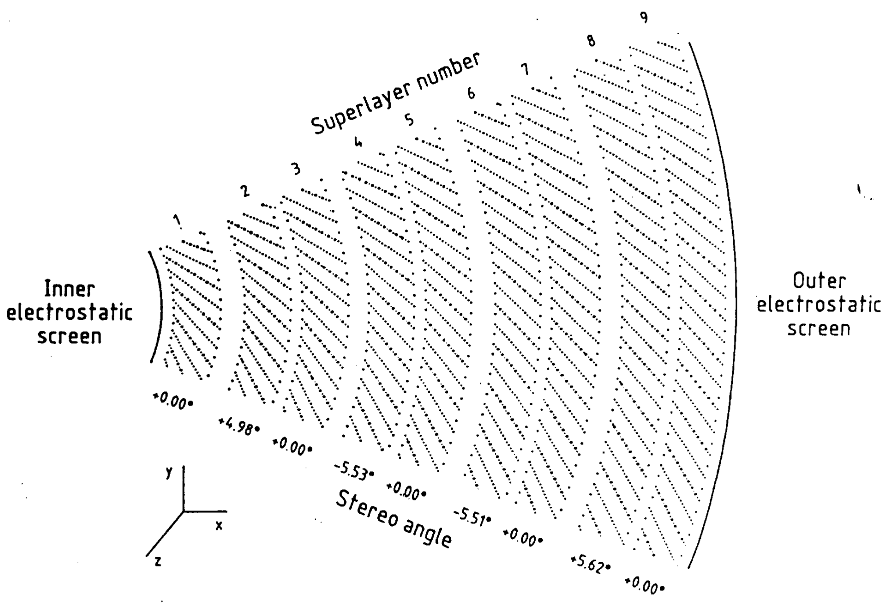

Figure 4.8: Segment of the CTD in cross sectional view: Shown are the nine super-layers with their different stereo angles.

The CTD is divided into nine super-layers, each consisting of eight sense wire layers. Figure 4.8 shows a cross sectional view of a CTD segment. The chamber has an outer radius of 85 cm and an overall length of 241 cm, while the active dimensions are $18.2 - 79.4$ cm and 204 cm, respectively. The polar angle coverage is $15° < \theta < 165°$ taking into account that a measured track is required to pass through at least two super-layers. The basic structure is a cell which is made up from eight sense wires surrounded by drift wires. The overall number of sense wires is 4608 complemented by 19584 field wires arranged in 576 cells. The drift chamber is filled with a gas mixture (with proportion 85 : 5 : 1) of argon (Ar), carbon dioxide (CO_2) and ethane (C_2H_6) bubbled through ethanol (C_2H_6O) at atmospheric pressure. The gas will be ionised by traversing charged particles along their trajectories. The produced electrons and ions will drift to different charged wires. In the field of the sense wire they produce new electron ion pairs, which leads to an avalanche effect and a multiplication of the signal of typically 10^4-10^5.

The wire planes are oriented at an angle of 45° to the radial direction to compensate the Lorentz angle of 45°, resulting from the combined electric and magnetic field. This ensures an optimal drift path and reduces the drift time (max. drift time ~ 500 ns). From the innermost to the outermost the super-layers are numbered from one to nine. The wires of the five odd numbered super-layers lie in direction of the chamber axis, while those of the four even numbered super-layers are tilted by stereo angles of about $\pm 5°$ with respect to the beam line. This arrangement leads to a position resolution of about $\sigma_{\{r,\phi\}} = 200\ \mu$m ($\theta$-dependent) in the (r, ϕ)-plane and a z-coordinate resolution of $\sigma_z = 2$ mm. Three super-layers are equipped to provide z-by-timing measurements. With this method the z-position is obtained by measuring the difference of the running times of the signal at the two opposite ends of a wire. Since this method is much faster than the stereo method it is used for trigger purposes, although with a lower resolution of about $\sigma_z = 4$ cm. The primary vertex can be calculated by extrapolating the reconstructed tracks to the beam axis. The typical resolution is 0.4 cm in z direction and 0.1 cm in transverse direction, respectively.

The strong magnetic field of 1.43 T provided by the superconducting solenoid ensures a high transverse momentum (P_T) resolution of

$$\frac{\sigma(P_T)}{P_T} = 0.0058 \cdot P_T(\text{GeV}) \oplus 0.0065 \oplus 0.0014/P_T\ (\text{GeV}) \tag{4.3}$$

at $\theta = 90°$, where the first term corresponds to the hit position resolution, the second to the multiple scattering within and the third before the CTD.

4.2.3 The Micro-vertex Detector

The silicon-strip micro-vertex detector (MVD) [28] has been installed in 2001 during the shutdown period. This component was not available for the data analysed in this thesis. However, it might increase the sensitivity for future searches at ZEUS. It aims to improve tracking and vertexing capabilities significantly, in order to enhance the acceptance for High-Q^2 events and for events with heavy quarks.

Taking into account the physics requirements and the available space inside of the CTD the design requirements for the MVD are:

- polar angular coverage of $10° > \theta > 150°$
- measurement of three points per track, in two projections each
- at least 20μm hit resolution
- two-tracks separation of 200μm
- inner and outer radius limited by the inner volume of the CTD and the beam-pipe volume
- hit efficiency better than 95%
- noise occupancy better than 10^{-3}

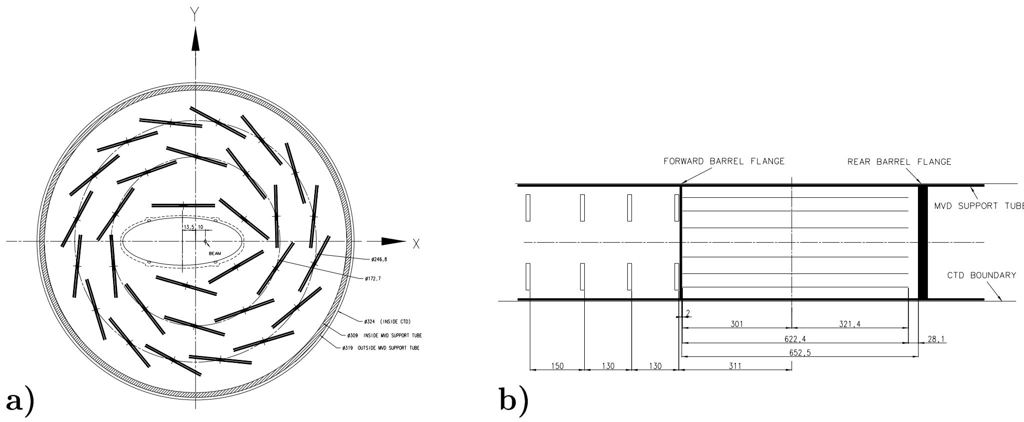

Figure 4.9: Layout of the MVD in the xy-view (a) and along the beam direction (b).

The MVD is divided into a barrel (BMVD) and a forward part (FMVD). Schematic pictures of the MVD are shown in Figure 4.9.

The barrel section is about 640 mm long and has a radial extension of about 310 mm. The single sided silicon sensors in the BMVD have the dimensions $64 \times 64\,\mathrm{mm}^2$ with a thickness of $320\,\mu\mathrm{m}$. Each sensor has 512 readout strips with a pitch of $120\,\mu\mathrm{m}$ alternated by five intermediate strips. The capacitive charge division between two readout strips can be used to determine the one-dimensional position of a hit very precisely. Under test beam environment a single hit resolution of about 8 µm has been determined. Two sensors are glued together with the strips perpendicular to each other to form a module providing two-dimensional position information. The modules are mounted on ladders building three layers around the elliptically shaped beam pipe.

The FMVD consists of four planes (wheels) mounted perpendicular to the beam line. A wheel is made of two layers of 14 silicon planes of the same type of the barrel sensors, having a wedge shape. The sensor strips of two overlapping planes are tilted by 13° providing r-ϕ information for particles traversing a wheel. The FMVD extends the polar angular coverage to $\theta = 0.015\,\mathrm{rad}$.

4.2.4 The Luminosity Monitor

The luminosity at ZEUS is measured via the theoretically well known bremsstrahlung process $ep \to e\gamma p$. The very high cross section for this reaction ($\sigma_{\mathrm{brems}} \approx \mathcal{O}(20\ \mathrm{mb})$), provides a fast and continuous monitoring of the event rate. The luminosity is determined by measuring the rate of the detected photons in the photon calorimeter. It is defined as:

$$\mathcal{L} = \frac{\dot{N}_{\mathrm{brems}}}{\sigma_{\mathrm{brems}}}, \tag{4.4}$$

where $\dot{N}_{\mathrm{brems}}$ is the photon rate and σ_{brems} is the cross section, corrected for detector acceptance.

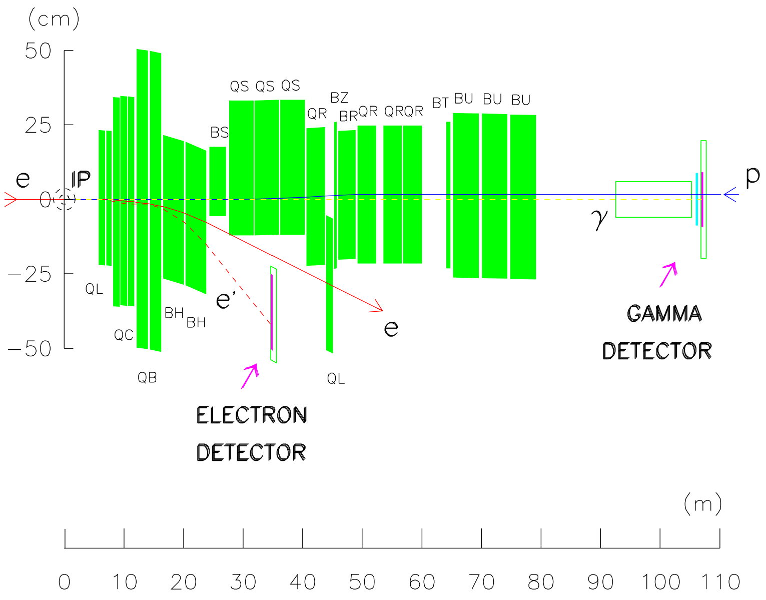

Figure 4.10: Schematic view of the luminosity monitoring system.

After the photons exit the beam pipe at small angles $\theta < 0.6$ mrad, they hit the γ detector (LUMI) [29], located at z= -107 m from the nominal interaction point and shielded by a carbon-lead filter to absorb synchrotron radiation (see Figure 4.10). The acceptance of the lead-scintillator photon calorimeter is about 98% and the effective resolution is $23\%/\sqrt{E(\mathrm{GeV})}$. Since the photon rate is very high, the statistical uncertainty is small. The systematic uncertainty is mainly due to the bremsstrahlung of the electrons on the residual gas molecules. The overall systematic uncertainty is in the order of $1.0 - 2.5\%$.

4.2.5 Trigger System and Data Acquisition

The task of the ZEUS trigger system [30] is to select the interesting events amongst the many background events. The bunch crossing frequency of 10.4 MHz (96 ns between two bunch crossings) and the high rate of minimum bias events is a challenge for the trigger system. This leads to the requirement of fast processors and algorithms.

The total event rate is dominated by proton beam gas interactions ($\sim$ 10 kHz) and proton beam halo events ($\sim$ 10 kHz) traversing the detector ($\sim$ 1 kHz). In comparison the physics DIS event rate is several orders of magnitude smaller. E.g. for NC DIS events ($Q^2 > 100\,\mathrm{GeV}^2$) the event rate is about 0.1 Hz and for CC DIS the event rate is in the order of 1 mHz, where the given rates correspond to an instantaneous luminosity of $2 \cdot 10^{31}\,\mathrm{cm}^{-2}\,\mathrm{s}^{-1}$. The ZEUS trigger system has three levels. A schematic overview of the data flow is shown in Figure 4.11.

The first level trigger (FLT), which is based on logical circuits, is designed to have an output rate of 1 kHz. The decision time is limited to 4.4 μs after one bunch crossing, which corresponds to 46 bunch crossings between two decisions. To avoid dead time the data of the detector components and the electronics are buffered to the pipeline, where they are processed with a rate of 10.4 MHz. Each detector component has its own trigger logic, based on fast computable global variables like energy sums and timing information. All individual decisions are stored in the global first level trigger (GFLT) and the accepted events are passed to the second level trigger (SLT).

The SLT is based on a network of programmable transputers. The data can be calculated more precisely and correlations of the information between different components are taken into account more accurately, such as track momenta, vertex position, electron and jet finding. The decisions are made after a time of 10 ns and are stored in the global second level trigger. This requires a pipeline buffering in the component readout systems. The data is reduced by a factor of 10 and is sent to the event-builder (EVB), where it is accessible to the third level trigger (TLT).

The TLT runs on a powerful processor farm. It has to cope with an event rate of about 100 Hz and reduces it to $\sim$ 10 – 15 Hz. The TLT makes a complete

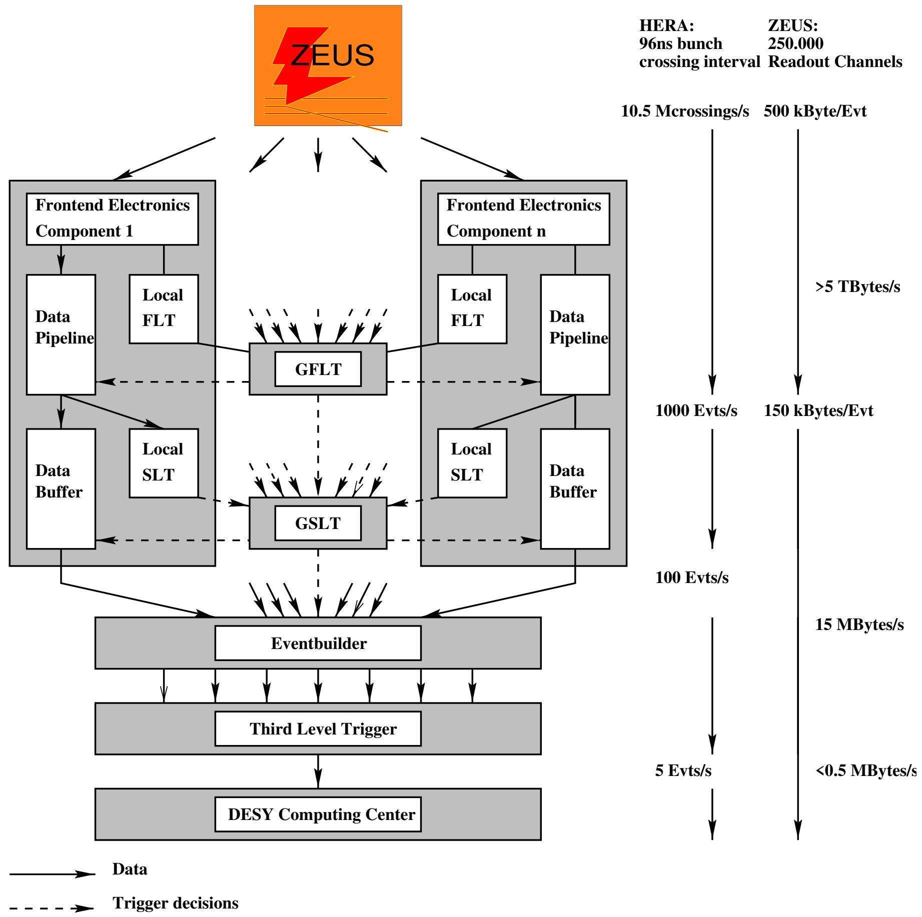

Figure 4.11: The ZEUS trigger and data acquisition system.

reconstruction of the event variables (tracking, muon, electron and jet finding etc.), using algorithms which are similar to that used in the offline code.

The fully reconstructed events are stored at the DESY computing centre, always accessible for further analysis purposes. During this process a pseudo fourth level trigger is introduced by assigning DST (data summary tapes) bits, which indicate whether an event fulfil a set of requirements or not. This mechanism ensures a fast access to a given class of events.

Chapter 5

Event Simulation

The simulation of physical processes plays an essential role for the understanding of the data achieved at high energy scattering experiments. Moreover, the physics simulations help to design selection criteria and to estimate detector acceptance. Monte Carlo (MC) programmes are tools used to simulate physics processes on the basis of statistical models. Since the complexity of high energy physics processes does not allow an analytical treatment of all theoretical and experimental effects, statistical models are designed to simulate the complete process. Usually, different MC programmes are used to simulate different stages of a full process in order to obtain the characteristic quantities of an event. This chapter describes the different programmes and models used to simulate SUSY and background events including the detector and trigger simulation.

5.1 MC Event Generators

The simulation of strong interactions at *ep* colliders can be divided into three parts: The parton level interaction, QCD radiation and hadronisation. The first two parts are simulating the hard subprocesses, which can be described by perturbative QCD, while the third one is modelling the the non-perturbative phase.

On the parton level, the interaction between the incoming electron and a parton, extracted from the proton, can be calculated in fixed order from the exact matrix elements and using the PDFs.

QED Radiation

The initial and final state radiation of photons from the incoming electron in first order QED processes can have a significant effect on the event topology and should be taken into account in the simulations or by applying correction factors. For initial state radiation (ISR), the effective energy of the incoming electron is lowered, causing a shift in the mean of the reconstructed kinematic variables. Although the emitted photons are collinear with respect to the outgoing lepton in final state radiation (FSR), it leads to a tail to larger opening angles of the measured final states, which can produce shifts in the kinematic variables. Radiative QED effects for the electron as well as for the proton, including ISR, FSR, vertex loops and self energy corrections also changes the cross section for a given x and Q^2. If not simulated, correction factors have to be applied in order to retrieve the Born cross section.

QCD radiation

Similarly to QED corrections, the initial and final state emission of gluons in higher order QCD processes can lead to additional hard jets. These radiative QCD effects are usually simulated by different MC programmes.

The initial and final state radiation of gluons in higher order QCD processes can be treated perturbatively. Two different approaches are commonly used to model these QCD corrections: The colour dipole model (CDM) [31] and the matrix element plus parton shower (MEPS) model.

The idea of the CDM is to treat $q\bar{q}$ pairs as colour dipoles which can emit gluons, where the initial $q\bar{q}$ pairs come from the quark struck by the exchanging boson and the quarks from the proton remnant. Radiated gluons can form further colour dipoles leading to a cascade of gluon emission until a minimal cut off energy has been reached.

In the MEPS model the parton shower is generated according to the Altarelli-Parisi splitting functions using the DGLAP leading log approximation [32]. Quarks and gluons evolve by successive branchings until all the partons reach some minimum energy.

Hadronisation

The hadronisation of coloured partons to colourless hadrons is a non-perturbative process and is yet not completely understood. Phenomenological models based on experimental data were designed to simulate the fragmentation of partons to observable hadrons. The two most common approaches are the Lund string model [33] and the clustering model [34].

In the Lund model, the colour field between a quark and a anti-quark is regarded as a string of constant energy density. With growing distance of the two partons the energy increases linearly until the energy is large enough to produce a new $q\bar{q}$ pair. These splitting processes continue until the energy of the initial $q\bar{q}$ pair is exhausted.

The cluster hadronisation model is based on the colour pre-confinement property of the angular-ordered parton shower. After that phase, the gluons are split non-perturbatively into $q\bar{q}$ pairs. All $q\bar{q}$ pairs combine to low mass colour singlet clusters, which decay into observable hadrons, according to the available phase space.

5.2 Background Simulation

NC DIS, CC DIS, photoproduction, di-muon production and single W boson production are considered as possible background sources.

Neutral and Charged Current DIS

High Q^2 NC DIS events having two or more hard jets in the final state are the main background for the electron channel search. For the neutrino channel search the main background is expected to come from di- and multi-jet CC DIS.

Period	Generator	PDF	kin. Cuts	$\mathcal{L}(\mathrm{pb}^{-1})$	Events
e^+p 97	DJANGO6/ ARIADNE	CTEQ4D	$Q^2 > 1 \cdot 10^4\,\mathrm{GeV}^2$	$5.1 \cdot 10^3$	11.7k
e^+p 97	DJANGO6/ ARIADNE	CTEQ4D	$Q^2 > 2 \cdot 10^4\,\mathrm{GeV}^2$	$52.1 \cdot 10^3$	11.6k
e^+p 97	DJANGO6/ ARIADNE	CTEQ4D	$Q^2 > 100\,\mathrm{GeV}^2$	26.4	14k
e^+p 97	DJANGO6/ ARIADNE	CTEQ5D	$Q^2 > 400\,\mathrm{GeV}^2$	38.5	10k
e^+p 99	DJANGOH/ ARIADNE	CTEQ5D	$Q^2 > 100\,\mathrm{GeV}^2$	150.4	2.4M
e^+p 99	DJANGOH/ ARIADNE	CTEQ5D	$Q^2 > 400\,\mathrm{GeV}^2$	171.3	200k
e^+p 97	DJANGO6/ MEPS	CTEQ4D	$Q^2 > 1 \cdot 10^4\,\mathrm{GeV}^2$	$5.1 \cdot 10^3$	11.7k
e^+p 97	DJANGO6/ MEPS	CTEQ4D	$Q^2 > 2 \cdot 10^4\,\mathrm{GeV}^2$	$52.1 \cdot 10^3$	11.6k
e^+p 99	DJANGOH/ MEPS	CTEQ4D	$Q^2 > 100\,\mathrm{GeV}^2$	20.5	228k
e^-p 99	DJANGOH/ MEPS	CTEQ4D	$Q^2 > 100\,\mathrm{GeV}^2$	20.5	228k
e^-p 99	DJANGOH/ MEPS	CTEQ4D	$Q^2 > 400\,\mathrm{GeV}^2$	51.4	60k

Table 5.1: Neutral current DIS Monte Carlo samples.

NC and CC DIS events are simulated with the DJANGOH 1.1 generator [35] which acts as an interface between the LEPTO 6.5.1 [36] and the HERACLES 4.6.1 generators [37][1].

HERACLES simulates initial state photon emission from the incoming electron as well as self energy and one-loop weak corrections. The LEPTO programme simulates the hard scattering process between the incoming electron and the parton in leading order. The parton density functions used are the CTEQ5D [38] parametrisation and the CTEQ4D [39] parametrisation for some older samples. First order QCD matrix elements for gluon radiation are implemented and higher order QCD radiation is treated using optionally the MEPS model or the CDM, as implemented in ARIADNE 4.10 [31]. Hadronisation is performed using the Lund string model, as implemented in JETSET 7.4. The generated NC and CC DIS MC samples used in this thesis are listed in Tables 5.1 and 5.2, respectively. The MC samples generated in the ARIADNE CDM are primarily used for this analysis, the samples generated in the MEPS model are used for a check of systematic uncertainties. Simulation of the HERA running periods before 1998 correspond to a centre of mass energy of $\sqrt{s} = 300\,\mathrm{GeV}$, whereas runs since 1998 correspond to $\sqrt{s} = 318\,\mathrm{GeV}$.

Photoproduction

Photoproduction events can fake the signal topology due to detector mismeasurements in both search channels. Since the cross section for photoproduction is large compared to the SUSY signal process, the number of faked electron or neutrino plus multi-jet events are not negligible. Table 5.3 shows the generated photoproduction MC samples.

The HEWRWIG 6.1 [34] and the PYTHIA 6.2 [33] MC programmes are used to simulate both, direct and resolved photoproduction events. HERWIG and Pythia simulate the hard scattering based on leading order matrix elements and use the parton shower approach for initial and final state QCD radiation. In HERWIG the transition from partons to hadrons is performed with the cluster fragmentation model, whereas in PYTHIA the hadronisation is based on the Lund string model. For all photoproduction MC samples the CTEQ4L parametrisation are used for the proton density functions and the GRV-G leading order parametrisation for the photon structure function. In order to reduce the number of events coming from soft interactions, cuts on the total transverse energy E_T and the missing transverse momentum P_T are applied.

[1] Also an older version of DJANGOH, called DJANGO6 2.4, which interfaces HERACLES 4.5.2 and LEPTO 6.5 are used for some samples. In the following all versions of DJANGOH and DJANGO6 are denoted as DJANGOH, unless stated otherwise.

Period	Generator	PDF	kin. Cuts	$\mathcal{L}(\mathrm{pb}^{-1})$	Events
$\boldsymbol{e^+p}$ ***97***	DJANGO6/ ARIADNE	CTEQ4D	$Q^2 > 10\,\mathrm{GeV}^2$	602.2	25k
$\boldsymbol{e^+p}$ ***99***	DJANGOH/ ARIADNE	CTEQ5D	$Q^2 > 10\,\mathrm{GeV}^2$	553.1	25k
$\boldsymbol{e^-p}$ ***99***	DJANGOH/ ARIADNE	CTEQ5D	$Q^2 > 10\,\mathrm{GeV}^2$	316.1	25k
$\boldsymbol{e^+p}$ ***99***	DJANGOH/ ARIADNE	CTEQ5D	$Q^2 > 100\,\mathrm{GeV}^2$	628.6	25k
$\boldsymbol{e^-p}$ ***99***	DJANGOH/ ARIADNE	CTEQ5D	$Q^2 > 100\,\mathrm{GeV}^2$	343.4	25k
$\boldsymbol{e^+p}$ ***99***	DJANGOH/ ARIADNE	CTEQ5D	$Q^2 > 5 \cdot 10^3\,\mathrm{GeV}^2$	$4.7 \cdot 10^3$	15k
$\boldsymbol{e^+p}$ ***97***	DJANGO6/ ARIADNE	CTEQ4D	$Q^2 > 5 \cdot 10^3\,\mathrm{GeV}^2$	$5.9 \cdot 10^3$	15k
$\boldsymbol{e^-p}$ ***99***	DJANGOH/ ARIADNE	CTEQ5D	$Q^2 > 5 \cdot 10^3\,\mathrm{GeV}^2$	$1.0 \cdot 10^3$	15k
$\boldsymbol{e^+p}$ ***99***	DJANGOH/ ARIADNE	CTEQ5D	$Q^2 > 1 \cdot 10^4\,\mathrm{GeV}^2$	$7.3 \cdot 10^3$	5k
$\boldsymbol{e^-p}$ ***99***	DJANGOH/ ARIADNE	CTEQ5D	$Q^2 > 1 \cdot 10^4\,\mathrm{GeV}^2$	$1.8 \cdot 10^3$	10k
$\boldsymbol{e^+p}$ ***99***	DJANGOH/ MEPS	CTEQ5D	$Q^2 > 10\,\mathrm{GeV}^2$	553.1	25k
$\boldsymbol{e^+p}$ ***99***	DJANGOH/ MEPS	CTEQ5D	$Q^2 > 100\,\mathrm{GeV}^2$	628.6	25k
$\boldsymbol{e^+p}$ ***99***	DJANGOH/ MEPS	CTEQ5D	$Q^2 > 5 \cdot 10^3\,\mathrm{GeV}^2$	$4.7 \cdot 10^3$	15k
$\boldsymbol{e^+p}$ ***99***	DJANGOH/ MEPS	CTEQ5D	$Q^2 > 1 \cdot 10^4\,\mathrm{GeV}^2$	$7.3 \cdot 10^3$	5k
$\boldsymbol{e^-p}$ ***99***	DJANGOH/ MEPS	CTEQ5D	$Q^2 > 10\,\mathrm{GeV}^2$	316.1	25k
$\boldsymbol{e^-p}$ ***99***	DJANGOH/ MEPS	CTEQ5D	$Q^2 > 100\,\mathrm{GeV}^2$	343.4	25k
$\boldsymbol{e^-p}$ ***99***	DJANGOH/ MEPS	CTEQ5D	$Q^2 > 5 \cdot 10^3\,\mathrm{GeV}^2$	$1.0 \cdot 10^3$	15k
$\boldsymbol{e^-p}$ ***99***	DJANGOH/ MEPS	CTEQ5D	$Q^2 > 1 \cdot 10^4\,\mathrm{GeV}^2$	$1.8 \cdot 10^3$	10k

Table 5.2: Charged current DIS Monte Carlo samples.

Period	Generator	PDF	kin. Cuts	$\mathcal{L}(\text{pb}^{-1})$	Events
***e*$^+$*p* 99**	HERWIG dir.	CTEQ4L	$E_T > 40\,\text{GeV}^2$ $P_T > 10\,\text{GeV}^2$	352.8	100k
***e*$^+$*p* 99**	HERWIG res.	CTEQ4L	$E_T > 40\,\text{GeV}^2$ $P_T > 10\,\text{GeV}^2$	352.8	100k
***e*$^+$*p* 97**	PYTHIA dir.+res.	CTEQ4L	$E_T > 15\,\text{GeV}^2$ $P_T > 6\,\text{GeV}^2$	35.1	40k
***e*$^+$*p* 99**	PYTHIA dir.+res.	CTEQ4L	$E_T > 15\,\text{GeV}^2$ $P_T > 6\,\text{GeV}^2$	155.0	200k

Table 5.3: Direct and resolved photoproduction Monte Carlo samples.

Di-Muon Production

Di-muon events, where one muon is not detected lead to an energy imbalance in the calorimeter. The energy deposition of the remaining muon or the proton remnant can be misinterpreted as hard jets from the gaugino decay. Hence, di-muon events are potential background source for the neutrino channel search. The generated di-muon MC samples used in this analysis are listed in Table 5.3. It is required that at least one muon has a transverse momentum greater than 10 GeV and lies in the polar angle range $5° < \theta < 175°$.

Period	Generator	PDF	kin. Cuts	$\mathcal{L}(\text{pb}^{-1})$	Events
***e*$^+$*p* 99**	GRAPE	MRSG	DIS, $P_T^\mu > 10\,\text{GeV}^2$ $5° < \theta^\mu < 175°$	$1.85 \cdot 10^5$	47k
***e*$^+$*p* 99**	GRAPE	MRSG	qel, $P_T^\mu > 10\,\text{GeV}^2$ $5° < \theta^\mu < 175°$	$5.0 \cdot 10^5$	8k
***e*$^+$*p* 99**	GRAPE	MRSG	el, $P_T^\mu > 10\,\text{GeV}^2$ $5° < \theta^\mu < 175°$	$2.3 \cdot 10^4$	30k

Table 5.4: Di-muon Monte Carlo samples.

Di-muon events are generated with the di-lepton MC programme GRAPE 1.1 [40]. The cross section calculation of GRAPE is based on the exact matrix elements, where all the electroweak diagrams at tree level are included. For the parton density functions the MRSG parametrisation is used. The Bethe-Heitler process, QED Compton and Z^0 production as well as initial and final state radiation are considered. The kinematic phase space can be divided into three regions: Elastic (el) and quasi-elastic (qel) scattering and DIS. GRAPE is interfaced to JETSET 7.4 [41] to simulate the hadronisation of the partonic final states.

Single W Boson Production

Single W production in the leptonic decay mode is a potential background source for the neutrino search channel, if the electron or the muon is misidentified. The typical topology of this process in this case would be: missing transverse momentum and jets.

Period	Generator	PDF	kin. Cuts	$\mathcal{L}(\,\mathrm{pb}^{-1})$	Events
e^+p *99*	W^- EPVEC dis	CTEQ4D	$u_{\mathrm{cut}} > 25\,\mathrm{GeV}^2$	$24.9 \cdot 10^3$	10k
e^+p *99*	W^- EPVEC res	CTEQ4D	$u_{\mathrm{cut}} > 25\,\mathrm{GeV}^2$	$82.9 \cdot 10^3$	10k
e^+p *99*	W^+ EPVEC dis	CTEQ4D	$u_{\mathrm{cut}} > 25\,\mathrm{GeV}^2$	$20.4 \cdot 10^3$	10k
e^+p *99*	W^+ EPVEC res	CTEQ4D	$u_{\mathrm{cut}} > 25\,\mathrm{GeV}^2$	$65.8 \cdot 10^3$	10k

Table 5.5: Single W production Monte Carlo samples, where the W decays to an electron and a neutrino or a muon and a neutrino.

The MC generator program EPVEC [42] is used to generate the $W^{\pm}$ boson production events. In order to increase the generation rate in EPVEC the produced $W^{\pm}$ boson is forced to decay into a lepton neutrino pair, where the lepton is an electron or a muon. EPVEC is a leading order program and includes no QCD radiation. The hadronisation of the final state is based on the LUND string model, as implemented in JETSET 7.4.

The phase space for W production can be divided into two regions, defined by $u = (p_q - q_W)^2$, where p_q and q_W are the four momenta of the incoming quark and the final state $W^{\pm}$ boson, respectively. In the resolved photon region, where u is small, the photon is almost on shell and can fluctuate into a massless quark anti-quark pair. In comparison, in the DIS region u is comparatively large and the photon highly virtual. The cut $u_{\mathrm{cut}} > 25\,\mathrm{GeV}^2$ is applied to all samples. The generated single W production MC samples are summarised in Table 5.5.

5.3 SUSY Simulation

The programme SUSYGEN 3.0 [18] is used to generate the signal events within the framework of the $\not{R}_P$ MSSM. SUSYGEN can calculate any $eq \to \tilde{x}q'$ process including the s-, t- and u-channel contributions using the full matrix elements, where $\tilde{x}$ denotes a sparticle. Also all two- and three-body decays of a sparticle are simulated from the exact first order matrix elements. Initial and final state gluon radiation are treated in the parton shower approach, whereas initial and final state QED radiation is not simulated by SUSYGEN. SUSYGEN is interfaced to JETSET 7.4 in order to simulate hadronisation effects according to the Lund string model. The CTEQ5M parametrisation for the parton densities in the proton are used.

Generator	**Parameter**	$\mathcal{L}(\mathrm{pb}^{-1})$	**Events**
SUSYGEN	$\mu = -400\,\mathrm{GeV},\ M_2 = 150\,\mathrm{GeV}$ $M_{\tilde{l}} = 100\,\mathrm{GeV},\ \tan\beta = 30$	$2.4 \cdot 10^4$	50k
SUSYGEN	$50 < \lvert\mu\rvert < 400\,\mathrm{GeV},\ 50 < M_2 < 250\,\mathrm{GeV}$ $M_{\tilde{l}} = 100\,\mathrm{GeV},\ \tan\beta = 2$		126 × 5k
SUSYGEN	$50 < \lvert\mu\rvert < 400\,\mathrm{GeV},\ 50 < M_2 < 250\,\mathrm{GeV}$ $M_{\tilde{l}} = 120\,\mathrm{GeV},\ \tan\beta = 2$		126 × 5k
SUSYGEN	$50 < \lvert\mu\rvert < 400\,\mathrm{GeV},\ 50 < M_2 < 250\,\mathrm{GeV}$ $M_{\tilde{l}} = 140\,\mathrm{GeV},\ \tan\beta = 2$		126 × 5k
SUSYGEN	$50 < \lvert\mu\rvert < 400\,\mathrm{GeV},\ 50 < M_2 < 250\,\mathrm{GeV}$ $M_{\tilde{l}} = 100\,\mathrm{GeV},\ \tan\beta = 6$		126 × 5k
SUSYGEN	$50 < \lvert\mu\rvert < 400\,\mathrm{GeV},\ 50 < M_2 < 250\,\mathrm{GeV}$ $M_{\tilde{l}} = 120\,\mathrm{GeV},\ \tan\beta = 6$		126 × 5k
SUSYGEN	$50 < \lvert\mu\rvert < 400\,\mathrm{GeV},\ 50 < M_2 < 250\,\mathrm{GeV}$ $M_{\tilde{l}} = 140\,\mathrm{GeV},\ \tan\beta = 6$		126 × 5k
SUSYGEN	$50 < \lvert\mu\rvert < 400\,\mathrm{GeV},\ 50 < M_2 < 250\,\mathrm{GeV}$ $M_{\tilde{l}} = 100\,\mathrm{GeV},\ \tan\beta = 30$		126 × 5k
SUSYGEN	$50 < \lvert\mu\rvert < 400\,\mathrm{GeV},\ 50 < M_2 < 250\,\mathrm{GeV}$ $M_{\tilde{l}} = 120\,\mathrm{GeV},\ \tan\beta = 30$		126 × 5k
SUSYGEN	$50 < \lvert\mu\rvert < 400\,\mathrm{GeV},\ 50 < M_2 < 250\,\mathrm{GeV}$ $M_{\tilde{l}} = 140\,\mathrm{GeV},\ \tan\beta = 30$		126 × 5k

Table 5.6: Generated SUSY Monte Carlo samples. All samples simulate e^+p collisions at $\sqrt{s} = 318\,\mathrm{GeV}$ using CTEQ5M as PDF and with $\lambda'_{111} = 1.0$.

Different sets of MC samples have been generated. One high statistics sample of $50,000$ events are used to estimate efficiency and purity in order to tune the selection cuts. More than one thousand small samples of $5,000$ events each are used to determine the detector acceptance of the selection cuts for the different points in the MSSM parameter space. In this way a large region of the parameter space is covered.

For this parameter scan μ and M_2 are varied by typical steps of $15 - 50\,\mathrm{GeV}$ at three values of $\tan\beta = 2, 6, 30$ and for slepton masses of $M_{\tilde{l}} = 100, 120, 140\,\mathrm{GeV}$. λ'_{111} is set to be 1.0 for all MC samples. All squark masses are set to be large and all slepton masses to be degenerate. It is assumed that the single Yukawa coupling λ'_{111} is dominant and the contributions from the other $\not{R}_P$ Yukawa couplings are negligible. All SUSY MC sets are listed in Table 5.6, simulating e^+p collisions at a cms energy $\sqrt{s} = 318\,\mathrm{GeV}$.

5.4 Detector & Trigger Simulation

The simulated events from the generator programme are processed further by the ZEUS detector and trigger simulation programme MOZART which is based on GEANT [43]. The MOZART package simulates the response of the different detector components and takes into account the detector geometry and the interaction of particles with the inactive material. The output of MOZART is passed to the CZAR code which simulates the trigger logic as implemented in the data taking. The quality of the detector and trigger simulation was maintained with the results from test-beam measurements and is continuously improved with data from the running experiment. Finally, the simulated events are sent to the reconstruction package ZEPHYR which is also used for the reconstruction of data events.

Chapter 6

Event Reconstruction

6.1 Reconstruction of Energies

The total energy of the event, E, is defined as the sum of all energy deposits in the calorimeter cells.

$$E = \sum_{i}^{\text{cells}} E_i \tag{6.1}$$

The components of the total momentum in Cartesian coordinates are given by:

$$p_x = \sum_{i}^{\text{cells}} E_i \sin\theta_i \cos\phi_i \tag{6.2}$$

$$p_y = \sum_{i}^{\text{cells}} E_i \sin\theta_i \sin\phi_i \tag{6.3}$$

$$p_z = \sum_{i}^{\text{cells}} E_i \cos\theta_i \tag{6.4}$$

The total transverse energy, E_T, is the scalar sum of the transverse energies of the individual cells:

$$E_T = \sum_{i}^{\text{cells}} \sqrt{p_{x,i}^2 + p_{y,i}^2} \tag{6.5}$$

$$= \sum_{i}^{\text{cells}} E_i \sin\theta_i \tag{6.6}$$

The missing transverse momentum, P_T, is defined as the magnitude of the vector sum:

$$P_T = \sqrt{p_x^2 + p_y^2} \tag{6.7}$$

The longitudinal energy variable can now be identified as

$$E - p_z = \sum_i^{\text{cells}} E_i(1 - \cos\theta_i). \tag{6.8}$$

The corresponding variables using the information of the hadronic system only are denoted as P_T^h and $(E - p_z)_h$.

Energy Correction

In order to reduce noise in the calorimetric cells caused by the radioactive uranium and the readout electronics, energy cuts of 100 and 150 GeV are applied on EMC and HAC cells, respectively.

Random discharges of the photomultipliers can result in fake energy deposits in the calorimeter (sparks). This effect can be avoided by discarding cells from the reconstruction which have a large energy imbalance between the two different photomultipliers:

$$\frac{|E_L - E_R|}{E_L + E_R} > 0.8, \tag{6.9}$$

$$\frac{E_L + E_R}{2} > 1.0\,\text{GeV}, \tag{6.10}$$

where E_L (E_R) is the energy measured by the left (right) side photomultiplier. The thresholds are obtained from studies using randomly triggered events.

Energies also have to be corrected for inactive materials in front of the CAL. The correction factors are estimated using a map of inactive materials and are parametrised as functions of polar and the azimuthal angles. Hadronic and electromagnetic energies are treated differently according to their different interaction in material.

The energy loss in the boundary regions between the different parts of the CAL (super-crack) are corrected using results from studies of the calorimeter response for hadronic energies.

Particles which are deflected backwards from the CAL surface or materials in front of the CAL can also lead to energy mismeasurements. This effect is usually small, however, it can cause a significant shift in the $E - p_z$ distribution. The correction factors of this effect were also obtained from studies of the calorimeter response for hadronic energies.

The scale of the measured energies and the simulated ones show a discrepancy by a factor which depend on the type and the position of the cell. Studies comparing data and MC energies propose the following corrections:

CAL Section	Cell Type	Energy Correction
FCAL	EMC	+4%
	HAC	-5%
BCAL	EMC	+4%
	HAC	+8%
RCAL	EMC	+2.5%
	HAC	+2.5%

Table 6.1: Correction factors for the electromagnetic and hadronic parts of the FCAL, BCAL and RCAL to correct for the energy scale difference between data and MC.

6.1.1 Clustering

Particles interacting with the calorimeter material will shower and usually deposit their energy in more than one cell. The purpose of a clustering algorithm is to combine the information of all cells which very likely belong to the shower of a single particle.

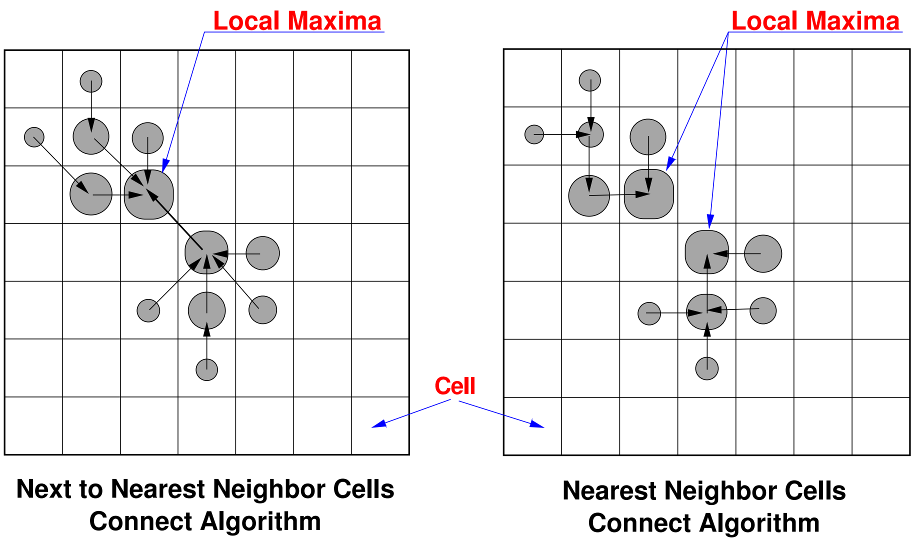

Figure 6.1: A schematic illustration of the clustering algorithm for cell islands. Cells are connected to the highest neighbouring cell. Two different definitions of neighbourhood are shown.

The clustering algorithm proceeds in two steps [44]. Local islands (cell islands) are formed in the first step, followed by the determination of global islands (cone islands) obtained from the cell islands.

After removing noisy cells by applying the noise threshold and the energy imbalance cuts, cell islands are formed in each of the different layers (EMC, HAC1, HAC2) and physical sections of the CAL (FCAL, BCAL, RCAL) separately. Each cell is connected to the highest energy cell in the neighbour, and the procedure is repeated until every cell is assigned to an island (see Figure 6.1).

In the next step the cell islands are combined to cone islands according to probability functions based on the (η,ϕ)[1] separation, which are derived from single pion MC events. The matching goes from the outer layers (HAC2) inwards to the inner layers (EMC). Also different EMC islands and islands from different CAL sections can be connected to each other. The position of the cluster is defined by the centre of gravity of the cone island taking into account the energy imbalance of each cell. Cluster energies are corrected for backsplashing effects, inactive material absorption and super-crack energy losses. Finally, the correction factors for data-MC discrepancies are applied

Energy Flow Objects

The accuracy of position and energy measurement can be significantly improved, combining tracking and calorimeter information. In general, the energy resolution of charged particles is better when using the CTD, in particular for low energy particles and if the particle goes through inactive material after the tracking detector and before the calorimeter. In addition, the position of clusters can be better determined using also tracking information.

The EFO (energy flow objects) algorithm tries to match cone islands with good tracks from the CTD. Good tracks have to fulfil a certain set of requirements which ensure a reliable measurement of the track. Details of the track matching requirements and the algorithm can be looked up in [45]. The matching procedure can have several outcomes:

1. Unmatched track: Good track which is not associated with any island object. The energy is determined from assuming the particle is a pion.

2. Unmatched island: Island which is not associated with any good track. The calorimeter information is chosen.

3. Island which is associated with more than three good tracks: The calorimeter information is chosen.

4. Island which is associated with one good tracks (1-to-1): The decision whether to take track or island information depends on other requirements (position, P_T, E_{cal}, etc.).

5. 1-to-2, 1-to-3, 2-to-1, 2-to-2, etc.: Similar to the 1-to-1 case.

[1]The pseudorapidity is defined as $\eta = -\ln\left(\tan\frac{\theta}{2}\right)$, where the polar angle, θ, is measured with respect to the proton beam direction.

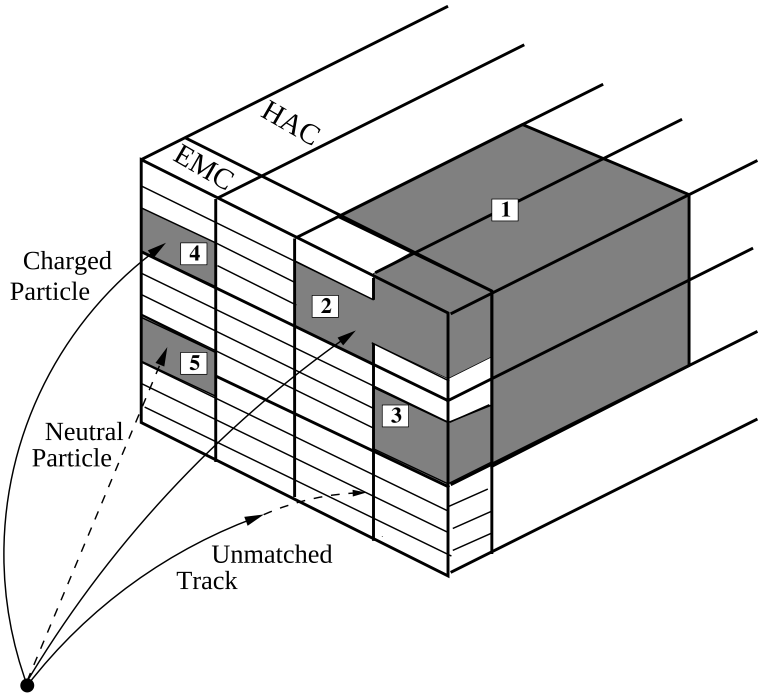

Figure 6.2: A schematic representation of the matching between tracks and cone islands.

6.2 Reconstruction of kinematic Variables

Double-Angle Method

The double angle (DA) reconstruction method [46] can be used to estimate the kinematic variables of neutral current DIS events. Q^2, x and y are determined from the polar angle of the scattered electron θ_e and the one of the hadronic system γ_h.

$$Q^2_{\mathrm{DA}} = (2E_e^{\mathrm{b}})^2 \frac{\sin\gamma_h(1+\cos\theta_e)}{\sin\gamma_h + \sin\theta_e - \sin(\theta_e+\gamma_h)}, \tag{6.11}$$

$$x_{\mathrm{DA}} = \frac{E_p}{E_e^{\mathrm{b}}} \frac{\sin\gamma_h + \sin\theta_e + \sin(\theta_e+\gamma_h)}{\sin\gamma_h + \sin\theta_e - \sin(\theta_e+\gamma_h)}, \tag{6.12}$$

$$y_{\mathrm{DA}} = \frac{Q^2_{\mathrm{DA}}}{s \cdot x_{\mathrm{DA}}}, \tag{6.13}$$

where E_e^{b} and E_p are the energies of the incoming electron and the incoming proton, respectively. γ_h can be calculated as:

$$\cos\gamma_h = \frac{P_T^2 - (E-p_z)_h^2}{P_T^2 + (E-p_z)_h^2} \tag{6.14}$$

The electron energy can be estimated by using the DA variables:

$$E_{\mathrm{DA}}^{e} = 2E_e^{\mathrm{b}} \frac{\sin\gamma_h}{\sin\gamma_h + \sin\theta_e - \sin(\theta_e + \gamma_h)} \tag{6.15}$$

Jaquet-Blondel Method

In charged current DIS events the kinematic variables are determined from the hadrons, since the neutrino information is not accessible. The method by Jacquet and Blondel (JB) [47] are used in this case:

$$y_{\mathrm{JB}} = \frac{(E - p_z)_h}{2E_e^{\mathrm{b}}}, \tag{6.16}$$

$$Q^2_{\mathrm{JB}} = \frac{P_T^2}{1 - y_{\mathrm{JB}}}, \tag{6.17}$$

$$x_{\mathrm{JB}} = \frac{P_T^2}{s \cdot y_{\mathrm{JB}}(1 - y_{\mathrm{JB}})}. \tag{6.18}$$

6.3 Vertex & Track Reconstruction

The primary interaction vertex is measured by extrapolating the tracks, reconstructed with the CTD, to the beam axis. The typical resolution in z direction is 0.4 cm . The resolution in transverse direction is typically 0.1 cm, which is larger than the typical size of both beams. Hence, the x and y position of the primary vertex are not measured, but were set to the nominal coordinates $(x, y) = (0, 0)$ cm. Secondary interactions of particles with material in the beam pipe lead to events with large track multiplicities, where many of them can point to the interaction region. By considering secondary vertices for the fitting procedure the bias in the primary vertex is reduced and the reconstruction of the primary vertex can be improved.

Directions and momenta of tracks are reconstructed with the CTD. To avoid noise in the tracking chambers or the readout electronics, tracks with transverse momentum below 100 MeV and the ones which are not fitted to the primary vertex are removed from the event reconstruction.

For the track reconstruction a track candidate is fitted to a five parameter helix model. These five helix parameters, a_μ, specify the trajectory at the closest approach to an arbitrarily chosen reference point in the (x,y)-plane (see Figure 6.3):

1. $a_1 = \phi_H$ (angle tangent to the helix in the (x,y)-plane)
2. $a_2 = Q/R$ (Q is the charge, and R the local radius)
3. $a_3 = QD_H$ (D_H connects the helix to the reference point)

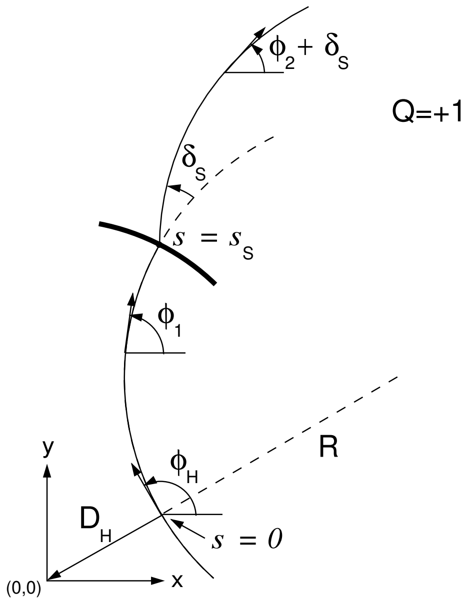

Figure 6.3: Track helix in (x,y)-plane.

4. $a_4 = z_H$
5. $a_5 = \cot\theta$

A 5×5 covariance matrix $c_{\mu\nu}$ is extracted from that fit. Hence, the charge of the particles are determined from this fit and its significance can be obtained from the corresponding covariance matrix. The significance of a charge measurement, cov(Q/R)/(Q/R), depends on the transverse momentum and the direction of the particle passing through the detector. A deviation of the reconstructed curvature from a nominal curvature of a imaginary neutral particle is harder to determine for high P_T tracks than for low P_T tracks. Very forward tracks pass only a few number of CTD super-layers and also suffer from higher background. From comparison of CTD momentum and CAL energy for isolated positrons, one knows that the diagonal element corresponding to the momentum error tends to be an over-estimate for well-measured tracks. This also affects the chi-squared, which tends to come out too small, i.e. well below the number of degrees of freedom. It follows that using the covariance matrix to estimate the significance of the determination of the sign of charge, for example, will give too low a significance.

A detailed description of the vertex and track reconstruction can be found in [48].

6.4 Jet Finding

The jet reconstruction algorithm used is the inclusive k_T algorithm (KTCLUS), which is invariant under boosts along the z-direction, as described in [49]. The algorithm is based on the transverse energy $E_{T,i}$, pseudorapidities η_i and azimuthal angles ϕ_i of the particles, where a particle can be any kind of calorimetric object. In this analysis, jets are defined as massless objects and are reconstructed using EFOs:

$$E_T^{\rm jet} = \sum_i E_{T,i}, \tag{6.19}$$

$$\eta^{\rm jet} = \frac{\sum_i E_{T,i}\eta_i}{\sum_i E_{T,i}}, \tag{6.20}$$

$$\phi^{\rm jet} = \frac{\sum_i E_{T,i}\phi_i}{\sum_i E_{T,i}}, \tag{6.21}$$

where the index i runs over all EFOs associated with the jet.

An outline of the KTCLUS algorithm is given in the following:

1. Start with a list of particles and an empty list of jets.
2. For each particle i as well as for each pair of particles (i, j) the distances d_i and d_{ij} are calculated, where

   $$d_i = E_{T,i}^2 R_0^2 \text{ and } d_{ij} = R_{ij}^2 \min(E_{T,i}^2, E_{T,j}^2), \text{ with } R_{ij}^2 = \Delta\eta_{ij}^2 + \Delta\phi_{ij}^2 \tag{6.22}$$

   The free parameter R_0 is set to $R_0 = 1.0$.
3. The smallest value of all the d_i and d_{ij} is labelled d_{min}.
4. If d_{min} belongs to the set of d_{ij}, the particles i and j are merged into a new particle using the recombination prescription in Equations (6.19)–(6.21) and removed from the list of particles.
5. If d_{min} belongs to the set of d_i, the particle i is removed from the list of particles and added to the list of jets.
6. When no particles are left (i.e. all particles are included in jets) the procedure is finished.

In addition, usually a cut on the transverse jet energy is applied to select hard jets.

6.5 Electron Finding

The EM finder [50] is based on detailed parametrisations of the detector response for electrons. It is optimised for the BCAL, FCAL and RCAL separately. Four calorimeter and three CTD variables are used to evaluate the probability of a calorimeter cluster to come from an electron.

1. $f_{\rm HAC}$, the fraction of energy in HAC1 and HAC2.

2. $f_{\rm CLeak}$, the fraction of EMC energy outside the highest energy cell strip pair. A cell strip is a set of EMC cells which have the same tower number cell type and calorimeter.

3. $f_{\rm MLeak}$, the fraction of energy, in the highest CAL module pair.

4. $E_{\rm cone}$, the energy which is not assigned to the candidate. but which lies within an (η, ϕ) cone of radius 0.8, which is centred on the candidate.

5. $\delta\theta = |\theta_{\rm Trk} - \theta_{\rm Cal}|$.

6. $\delta\phi = |\phi_{\rm Trk} - \phi_{\rm Cal}|$.

7. $\delta_{1/P} = |1/E - 1/P_{\rm Trk}|$.

For candidates which are outside of the tracking acceptance, or which do not have a matching track, only the first four quantities are used. All calorimeter quantities are derived from corrected cell islands, which means that all energy corrections, mentioned earlier in this chapter, are applied on cell islands.

Calculation of Probabilities

Each of the variables x is transformed into a sub-probability $f(x)$. The corresponding probability $P(x)$ is given by

$$P(x) = \int_{x}^{x_{\rm max}} {\rm d}x' f(x'). \tag{6.23}$$

$P(x)$ is uniformly distributed between 0 and 1 for real electrons. A higher value of $P(x)$ corresponds to a lower x and therefore a better electron candidate, since fake electrons tend to have larger values for each of the variables. The combined sub-probabilities can be transformed into the variable Q,

$$Q = P_k \sum_{k=0}^{N-1} \frac{(-\log P_k)^k}{k!}. \tag{6.24}$$

The variable Q is uniformly distributed between 0 and 1.

Outline of the Algorithm

Here is an outline of the algorithm which EM applies to an event.

1. Group calorimeter cells in clusters using cell islands.

2. Loop over islands. Accept the island, if a candidate passes these three cuts:
   - The energy of the island exceeds 4 GeV.
   - f_{HAC} is less than (0.3, 0.5, 0.3) for (FCAL, BCAL, RCAL).
   - The calorimeter probability $P_{\mathrm{Cal}}(f_{\mathrm{HAC}}, f_{\mathrm{MLeak}}, f_{\mathrm{CLeak}})$ exceeds 10^{-5}.
3. If the polar angle of the candidate satisfies $0.3 < \theta_e < 2.85$, check for a matching track. Only tracks which satisfy the following criteria are considered:
   - $P_T > 0.1\,\mathrm{GeV}$,
   - distance of closest approach to the beam-line is less than 2 cm,
   - distance of closest approach to the CAL position is less than 50 cm,
   - $|\delta\theta| < \pi/4$,
   - $|\delta\phi| < \pi/4$.

   For tracks passing these cuts, the track match is accepted if $P_{\mathrm{Trk}}(\delta\theta, \delta\phi, \delta_{1/P})$ exceeds 10^{-3}.
4. The grand probability is calculated as follows:

   (a) If $(0.3 < \theta_e < 2.85)$ **AND** $(P_{\mathrm{Trk}}(\delta\theta, \delta\phi, \delta_{1/P}) > 10^{-3})$
   $\Rightarrow P_{\mathrm{Grand}} = P(f_{\mathrm{HAC}}, f_{\mathrm{MLeak}}, f_{\mathrm{CLeak}}, E_{\mathrm{cone}}, \delta\theta, \delta\phi, \delta_{1/P})$.

   (b) If $(0.3 < \theta_e < 2.85)$ **AND NOT**$(\ P_{\mathrm{Trk}}(\delta\theta, \delta\phi, \delta_{1/P}) > 10^{-3})$
   $\Rightarrow P_{\mathrm{Grand}} = (1 - \varepsilon_{\mathrm{trk}})P(f_{\mathrm{HAC}}, f_{\mathrm{MLeak}}, f_{\mathrm{CLeak}}, E_{\mathrm{cone}})$.

   (c) If **NOT** $(0.3 < \theta_e < 2.85)$
   $\Rightarrow P_{\mathrm{Grand}} = P(f_{\mathrm{HAC}}, f_{\mathrm{MLeak}}, f_{\mathrm{CLeak}}, E_{\mathrm{cone}})$,

   where $\varepsilon_{\mathrm{trk}}$ is the track matching efficiency.

The performance of the EM finder compared to the neural network SIRA5 finder [51] is shown in Figure 6.4, and in Figure 6.5 for low energy electrons, for the RCAL region and for low Q^2. The different algorithms were tested for NC DIS and photoproduction MC simulations [52]. Both finders have efficiencies of 99% and above within the BCAL region. At the RCAL and the FCAL edges the EM finder suffers from a drop of 3% and 4%, respectively, which is slightly better than the ones of SIRA5. In general, the EM finder shows a better performance in the forward region than the SIRA5 finder, whereas SIRA5 is better towards the RCAL region.

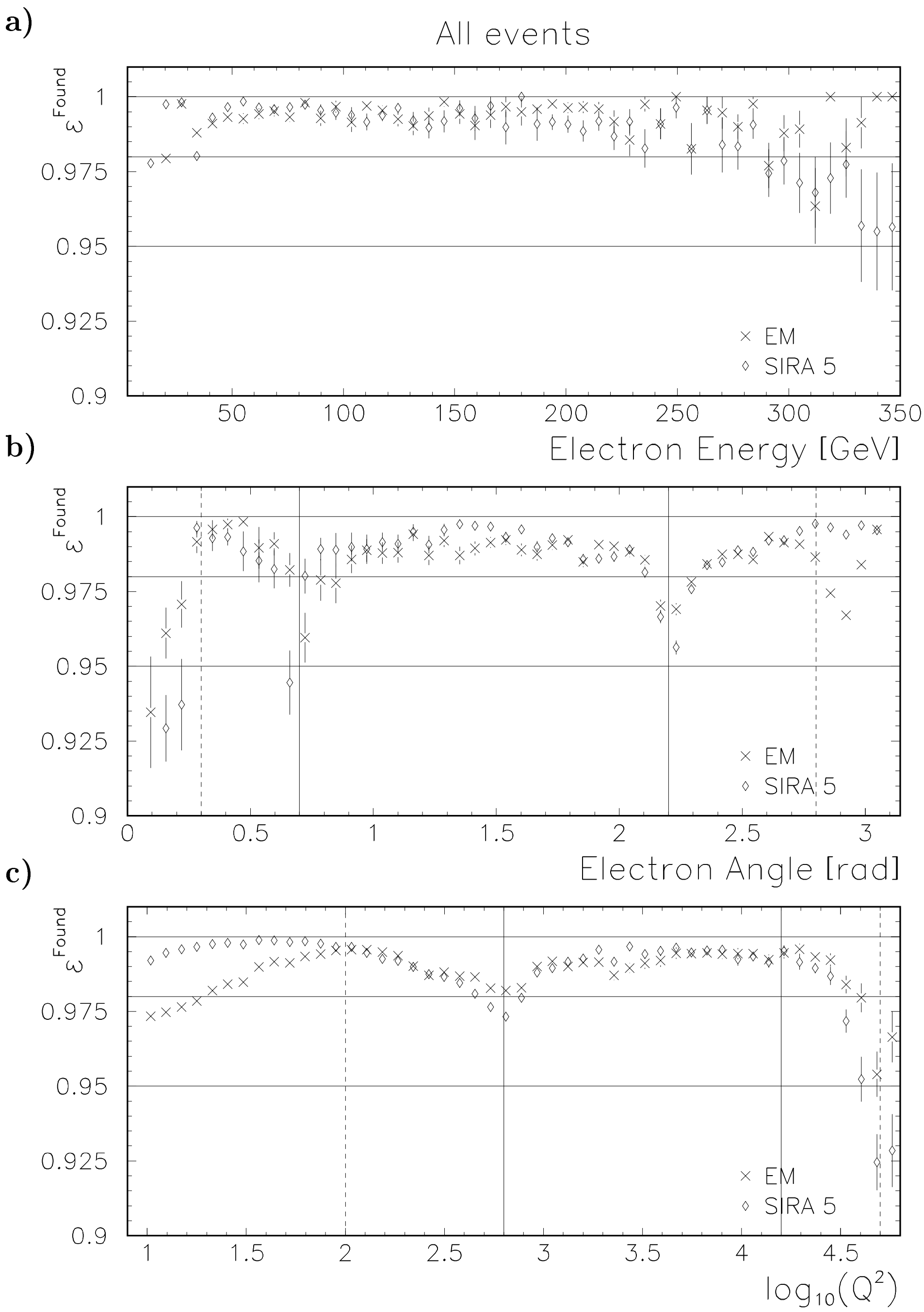

Figure 6.4: Electron efficiency of the EM (crosses) and the SIRA5 (diamonds) finders versus the energy (a), polar angle (b) and $log_{10}(Q^2)$ (c) of the true electron [52]. Horizontal lines represent 2% loss (upper line) and 2% loss (lower line). Vertical full lines denote CAL limits and vertical dashed lines indicate CTD end. On the $log_{10}(Q^2)$ plot the positions of the calorimeter are approximate.

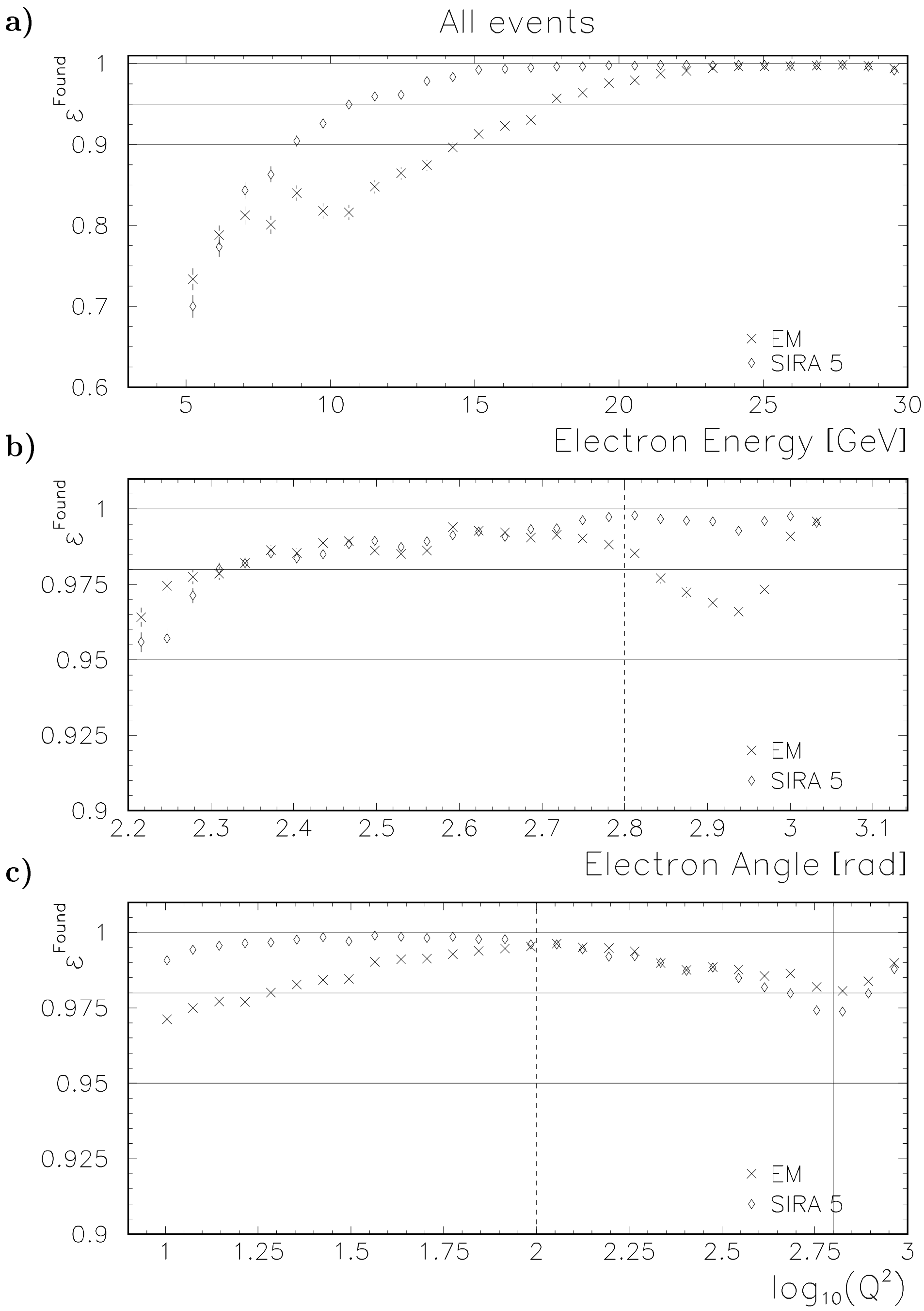

Figure 6.5: Efficiency of the EM (crosses) and the SIRA5 (diamonds) finders for low energy electrons (a), RCAL regions (b) and low Q^2 (c) of the true electron [52]. Horizontal lines represent 2% loss (upper line) and 2% loss (lower line). Vertical full lines denote CAL limits and vertical dashed lines indicate CTD end. On the $log_{10}(Q^2)$ plot the positions of the calorimeter are approximate.

6.6 Circularity

The circularity is the two-dimensional equivalent to sphericity which is defined elsewhere [53]. It is a measure for the distribution of calorimeter energy deposits in the plane transverse to the beam-line. The circularity (circ.) is defined as

$$\text{circ.} = 2 \cdot (1 - \max(\lambda_1, \lambda_2)), \tag{6.25}$$

where λ_1 and λ_2 are the eigenvalues of the 4×4 matrix

$$M_{ij} = \frac{\sum_k P_{i,k} P_{j,k}}{\sum_k (P_{1,k}^2 + P_{2,k}^2)}, \tag{6.26}$$

with $i(j) = 1, 2$. $P_{1,k}$ ($P_{2,k}$) is the x(y)-component of the four-vector of the k^{th} object and k runs over all jets and final state electrons (in the electron channel) or over all jets and the energy imbalance four-vector (in the neutrino channel), respectively.

The circularity is defined between 0 and 1. Events with uniformly distributed objects typically have circularity close to 1, while events, for instance, containing only one object have typically values close to 0.

6.7 Energy Measurement & Simulation

6.7.1 Energy Calibration

In order to examine the accuracy of the energy measurement a comparison of corrected E^e from the EM finder with the respective DA variable in NC DIS data is performed. The NC DIS data are selected as described in Section 8.3.1 from the same data set used in this analysis.

Figure 6.6 shows the ratio E^e/E^e_{DA} in bins of E^e for both NC DIS data and MC. The distributions show a peak around one, indicating that the corrected electron energy is well reconstructed. The overall agreement between data and MC indicates that the calorimeter calibration is consistent for data and MC. Within statistical errors, also the bins of large E^e are described fairly. Figure 6.8a shows the mean of E^e/E^e_{DA} as a function of E^e_{DA}, the error bars indicate the root-mean-square (rms) of the distributions.

The hadronic energy measurement is checked by comparing the electron transverse momentum (P_T^e) with the transverse momentum of the hadronic system (P_T^h).

The ratio P_T^e/P_T^h in bins of P_T^e is shown in Figure 6.7. Also here the distributions peak at unity. In bins with sufficient statistics the agreement between data and MC is good. At the two highest P_T^e bins the data suffers from small statistics.

But also here the data is fairly described by the MC. Figure 6.8b shows the mean of P_T^e/P_T^h as a function of P_T^e with the error bars indicating the rms of the distributions.

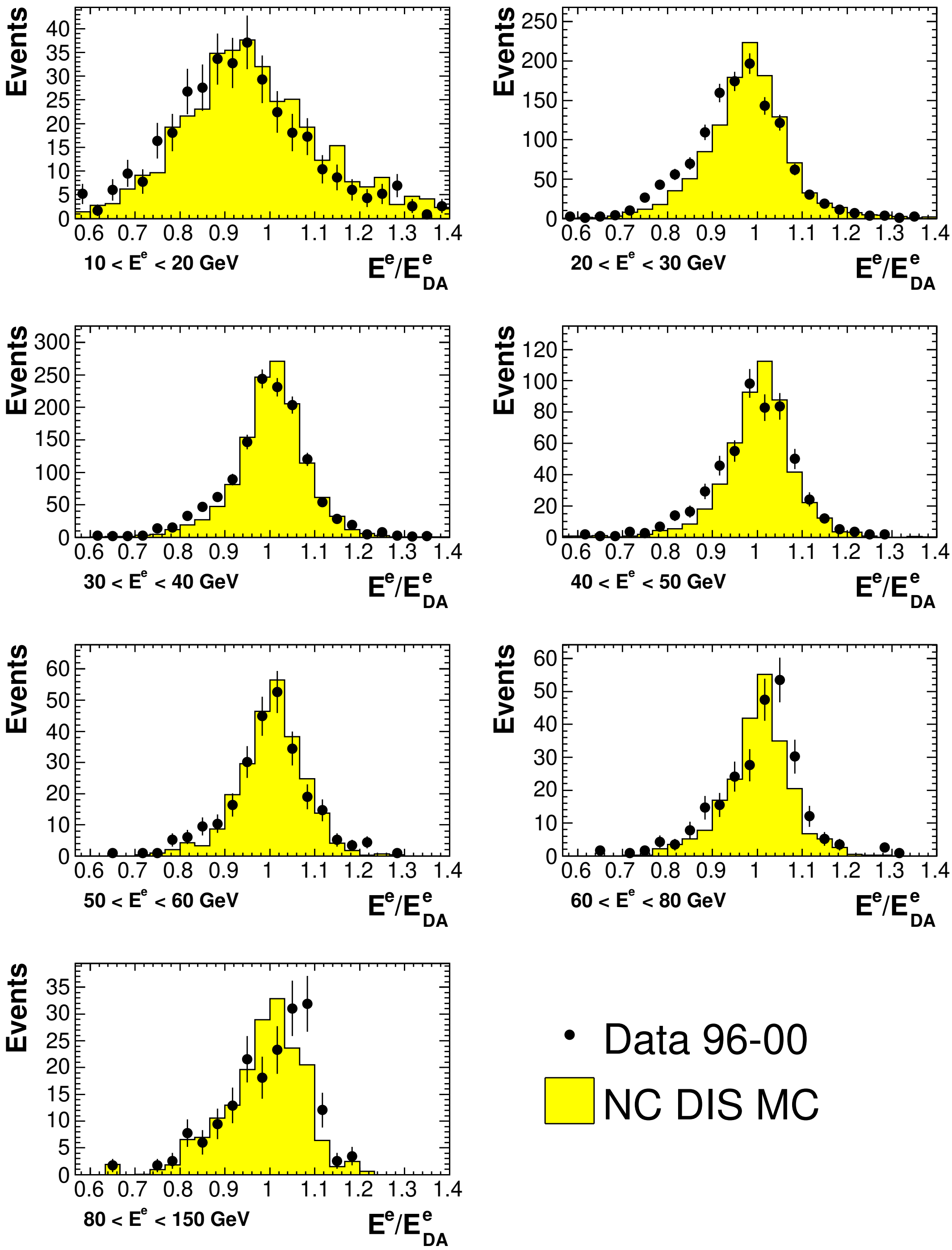

Figure 6.6: Comparison of corrected electron energies E^e with the respective DA varibale in bins of E^e using NC DIS data (dots) and NC DIS MC (histograms).

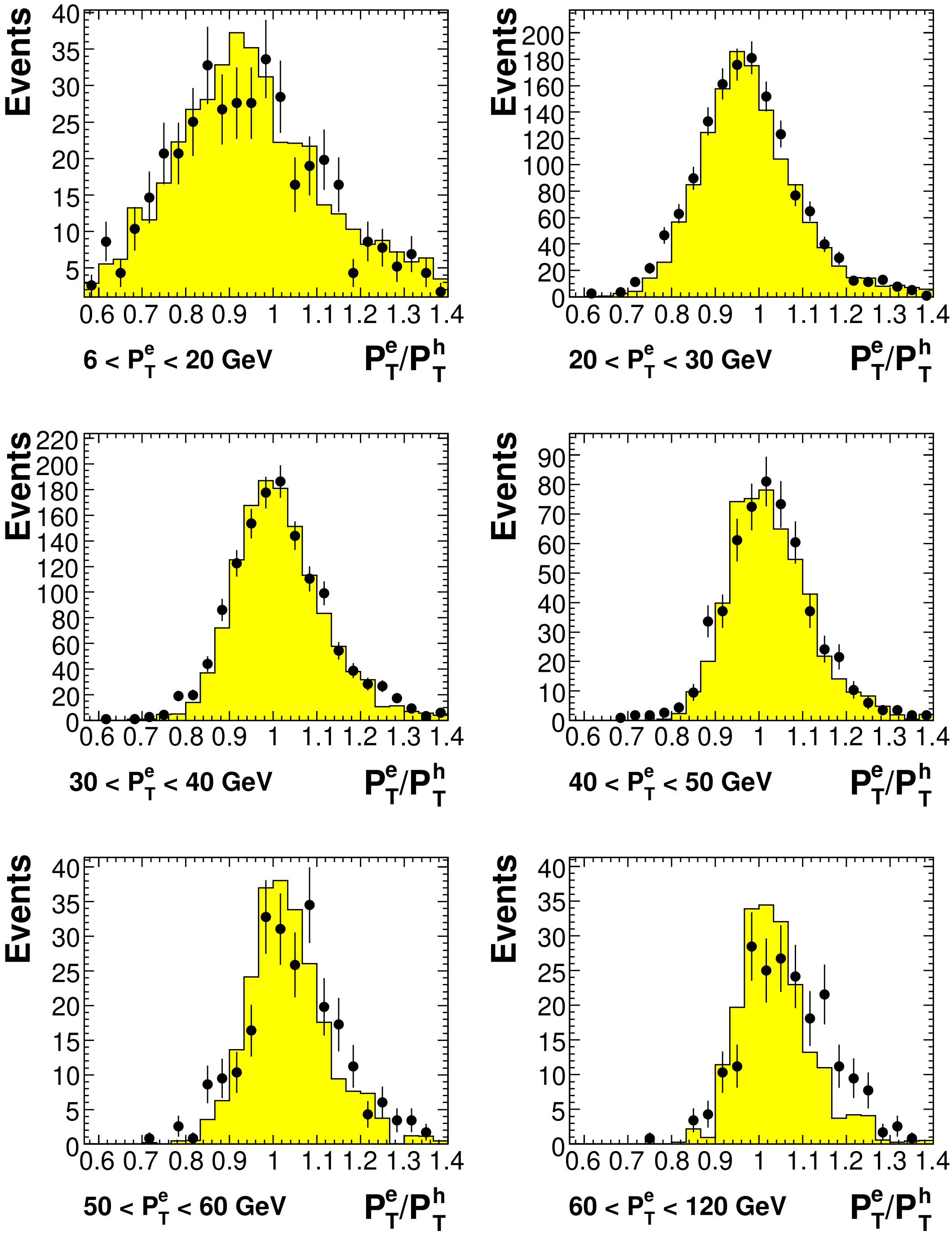

Figure 6.7: P_T^e/P_T^h in bins of P_T^e for CC DIS data and CC DIS MC.

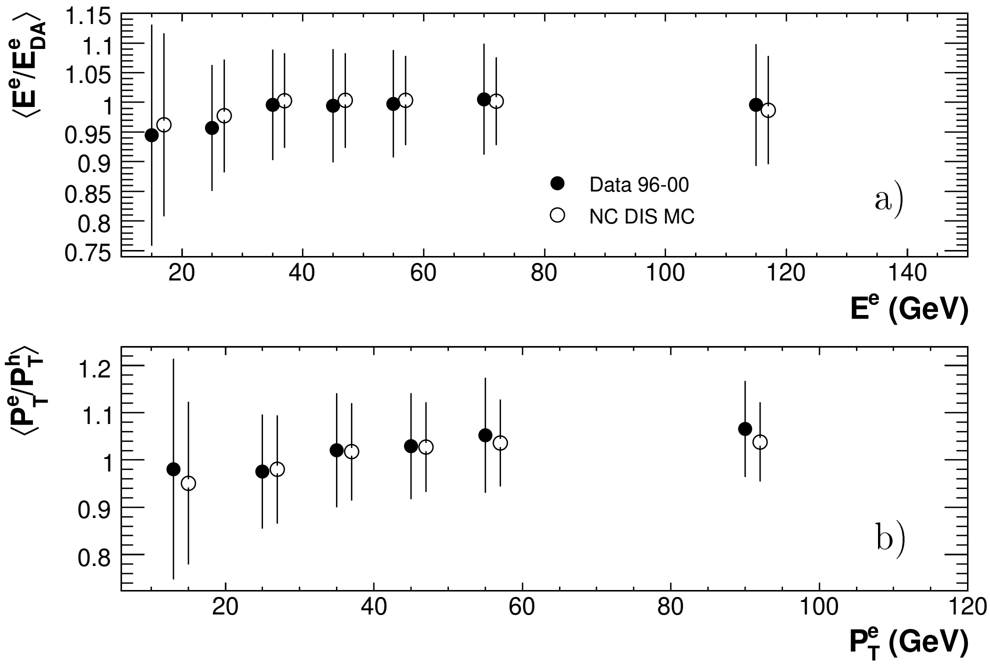

Figure 6.8: Mean of E^e/E^e_{DA} (a) and P^e_T/P^h_T (b) as a function of E^e and P^e_T, respectively. The error bars indicate the rms of the distributions.

6.7.2 Kinematic Variables

The quality of the NC DIS kinematic reconstruction is evaluated by using NC DIS MC events with $Q^2_{\mathrm{true}} > 100\,\mathrm{GeV}^2$. Figure 6.9 shows the mean of $Q^2_{\mathrm{DA}}/Q^2_{\mathrm{true}}$, $y_{\mathrm{DA}}/y_{\mathrm{true}}$ and $x_{\mathrm{DA}}/x_{\mathrm{true}}$ as a function of the true variables. The error bars indicate the rms of the distributions. The reconstructed variables agree well with the respective true variables.

Similar plots are shown for CC DIS MC events with $Q^2_{\mathrm{true}} > 100\,\mathrm{GeV}^2$ in Figure 6.10, where the JB variables are compared with the respective true variables. Also here, a good reconstruction of the kinematic variables is achieved.

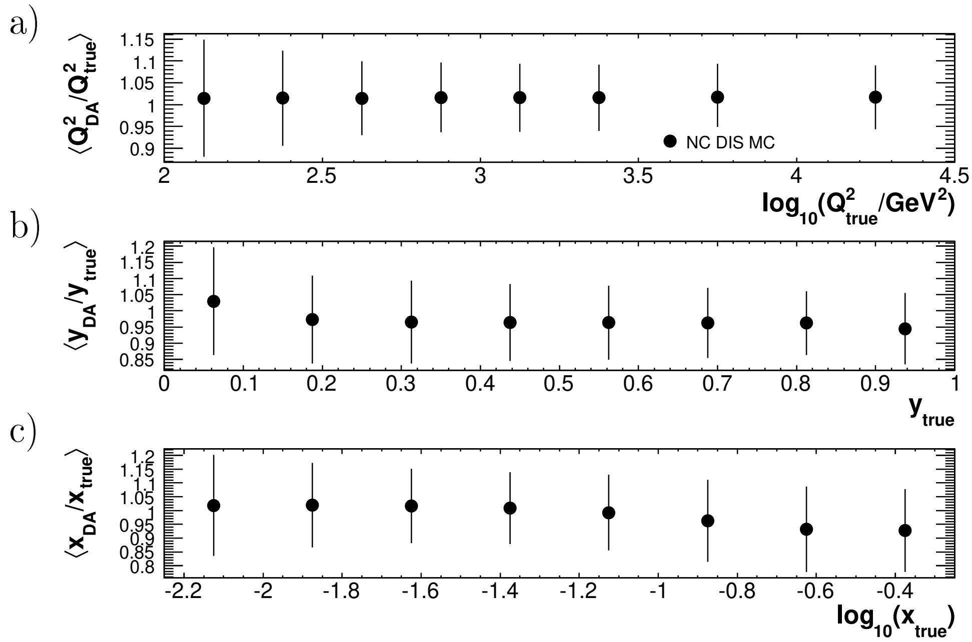

Figure 6.9: Mean of $Q^2_{\mathrm{DA}}/Q^2_{\mathrm{true}}$ (a), $y_{\mathrm{DA}}/y_{\mathrm{true}}$ (b) and $x_{\mathrm{DA}}/x_{\mathrm{true}}$ (c) in NC DIS MC as a function of the respective true variables. The error bars indicate the rms of the distributions.

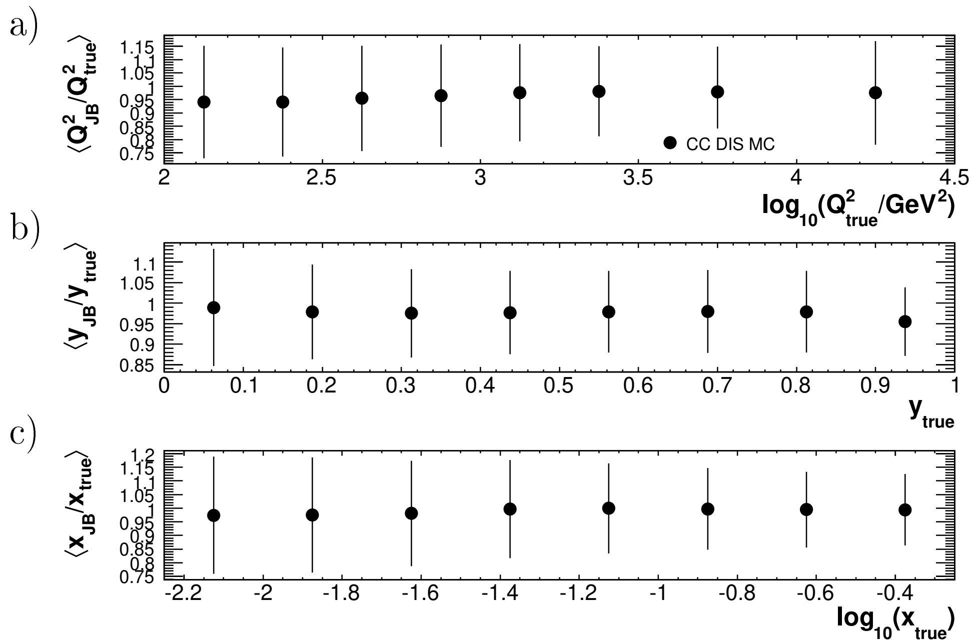

Figure 6.10: Mean of $Q^2_{\mathrm{DA}}/Q^2_{\mathrm{true}}$ (a), $y_{\mathrm{DA}}/y_{\mathrm{true}}$ (b) and $x_{\mathrm{DA}}/x_{\mathrm{true}}$ (c) in CC DIS MC as a function of the respective true variables. The error bars indicate the rms of the distributions.

Chapter 7

Statistical Event Classification

A common task in high energy physics is the search for a distinctive class of events (signal) and, at the same time, the suppression of background, in order to aquire high purity of the signal.

There are many approaches to encounter this problem. The most straight forward one is the use of linear cuts on variables, which characterise the signal and background events. The cut method can also be extended to more than one dimension and its advantages are obvious: The implementation is fast and simple and the physics interpretation is usually straight forward.

In many complex cases, especially when the characterising variables have unknown non-linear correlations, more elaborated multivariate techniques are needed. In the following I will briefly summarise the properties of some example, commonly used techniques.

Fisher's Linear Discriminant (FLD)

The basic idea of the FLD is to construct a separating hyperplane between the signal and background classes in the variable space. The best separating hyperplane is defined as the one that maximises the distance between the means of the two classes classes while minimising the distance within each class.

Artificial Neural Network (ANN)

ANNs are mathematical models, which mimic the functioning of neurons in biological systems. The concept of ANNs is based on the processing of information within and the interaction between nodes. Each node receives input data and performs a simple operation on these data (weighted sum and some kind of threshold function). The results are passed to other nodes for further processing. A network of nodes can be constructed in order to obtain a decision output for a given input and a given problem. ANNs can learn from training samples of different classes by adjusting the weights associated to all input connections until some overall function is maximised which characterises the quality of the decision mechanism.

Decision Trees (DT)

DTs are usually implemented as binary trees, where in each node a cut on a specific variable is imposed. The cut separates the variable space into signal-like and background-like parts. The input data is transfered successively from node to node down to the last decision branch. The number of nodes can be chosen according to desired complexity of the problem.

Probability Density Estimation (PDE)

The idea of the PDE is to estimate an unknown probability density for a given class from the training data.

Some likelihood methods extract the distributions for each input variable and each class from the training data, which are interpreted as sub-probability densities. This process corresponds to a projection of the total probability density to the axes of each input variable. The probability of one specific event is calculated from the product of the sub-probabilities, assuming no correlations between the variables. In practice, the latter assumption is never true. Moreover, during the projection process, the information about the correlations of the input variables is lost, which is probably useful for the decision.

The range searching method avoids this problem. It is the method of choice for this analysis and is explained in Section 7.1.

Summary

There is much debate about which approach is superior. It seems that there is no 'best method' for all problems, in general. For a given problem, the best choice is that which yields the most accurate estimate of the physical quantities of interest for given computational resources. In fact, it is often much more time consuming to find the 'best method' than to do the analysis itself. On the other hand, many surveys [54, 55] have shown that there are no big differences in the performance of the different multivariate methods discussed in this chapter. For this analysis the choice fall on the PDE approach using the range searching algorithm.

7.1 Multivariate Probability Density Analysis

In this thesis the technique used to discriminate signal events from background is the probability density estimation method based on range searching (PDE-RS)

[55].

An event can be classified by the probability of the event to be of the signal class $p(\vec{\boldsymbol{x}})$, when measuring n input variables $\vec{\boldsymbol{x}} = (x_1, ..., x_n)$. $p(\vec{\boldsymbol{x}})$ is given by the probability densities of the background $\rho_b(\vec{\boldsymbol{x}})$ and the signal $\rho_s(\vec{\boldsymbol{x}})$: $p(\vec{\boldsymbol{x}}) = \rho_s(\vec{\boldsymbol{x}})/(\rho_b(\vec{\boldsymbol{x}}) + \rho_s(\vec{\boldsymbol{x}}))$.

The real $\rho_s(\vec{\boldsymbol{x}})$ and $\rho_b(\vec{\boldsymbol{x}})$ are usually unknown. However, an estimate of $p(\vec{\boldsymbol{x}})$ can be obtained from MC simulations of the signal and the background. By sampling the n-dimensional variable space with simulated events, one can approximate probability densities of the signal ($\tilde{\rho}_s(\vec{\boldsymbol{x}}) \approx \rho_s(\vec{\boldsymbol{x}})$) and background ($\tilde{\rho}_b(\vec{\boldsymbol{x}}) \approx \rho_b(\vec{\boldsymbol{x}})$). The discriminant $D(\vec{\boldsymbol{x}})$ gives an estimate for the probability of an event to be signal or background:

$$D(\vec{\boldsymbol{x}}) = \tilde{p}(\vec{\boldsymbol{x}}) = \frac{\tilde{\rho}_s(\vec{\boldsymbol{x}})}{\tilde{\rho}_b(\vec{\boldsymbol{x}}) + \tilde{\rho}_s(\vec{\boldsymbol{x}})} \approx p(\vec{\boldsymbol{x}}) = \frac{\rho_s(\vec{\boldsymbol{x}})}{\rho_b(\vec{\boldsymbol{x}}) + \rho_s(\vec{\boldsymbol{x}})}. \tag{7.1}$$

One way to obtain $\tilde{\rho}_s(\vec{\boldsymbol{x}})$ and $\tilde{\rho}_b(\vec{\boldsymbol{x}})$ is counting the number of signal (N_s) and background events (N_b) in a small volume $V(\vec{\boldsymbol{x}})$ around the reference point $\vec{\boldsymbol{x}}$ (see Figure 7.1c). The discriminant from these local probability densities is defined as:

$$D(\vec{\boldsymbol{x}}) := \frac{N_s/V(\vec{\boldsymbol{x}})}{N_s/V(\vec{\boldsymbol{x}}) + N_b/V(\vec{\boldsymbol{x}})}, \tag{7.2}$$

In order to reduce statistical uncertainties for sufficiently small $V(\vec{\boldsymbol{x}})$, a large amount of MC events are needed.

Counting a large number of events in high dimensionality can be a very memory and time consuming task. Some likelihood methods avoid this problem by using projections with the disadvantage, that the correlations between the input variable are not taken into account. The range searching algorithm provides a fast way to compute the probability densities without losing higher dimensional information.

7.1.1 Range Searching Algorithm

The problem of counting the number of neighbours in a certain vicinity ($V(\vec{\boldsymbol{x}})$) of a reference point in n-dimensional space is known as 'range searching'. Range searching algorithms have been developed which allow a search time $\sim \log_2(N!) \approx N \cdot \log_2(N)$, where N is the number of points that have to be searched. In this algorithm the events are pre-ordered and stored in a binary tree [56].

The MC events are successively filled into the nodes of two binary trees, one for the signal and one for the background, respectively. A two-dimensional example for the filling and searching process is illustrated in Figure 7.1a-c.

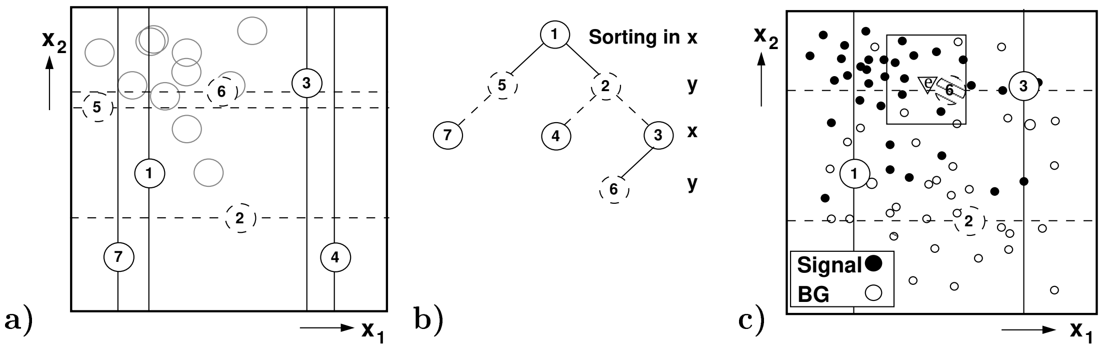

Figure 7.1: a-b) Two-dimensional example of a binary tree storing seven events according to their position in the (x_1, x_2)-plane, starting with the first event on the top node of the tree. Note that in b) x corresponds to x_1 and y corresponds to x_2. c) Signal and background events in the (x_1, x_2)-plane. The open triangle represents the event to be classified and the box around it depicts the volume $V(\vec{\mathbf{x}})$, which defines the region where events are considered to calculate the discriminant. All plots are from [55].

While descending the tree the decision quantity cycles through all input variables $x_i = x_1, \ldots, x_n$, starting with x_1 of the first event, then x_2 etc. After processing x_n of the first event, again x_1 of the second event is processed and so on, ending with x_n of the last event. The decision whether to descend to the left or to the right of a node depends on the value of the current input variable. If the value of the current variable x_i is smaller than x_i of the event stored in the actual node, then one descends to the left branch, otherwise to the right branch. If the end of a branch is reached, a new node is created at that position and the current event is stored in that node. After filling, the position of every event in the tree is given by its coordinates in the variable space and the order of events during the filling process.

The searching in the trees is done in the same manner as the filling. If x_i of the current event to be classified is smaller than x_i of the the first stored event e_1, only the events at the left to e_1 have to be considered for further searching, otherwise, one descends to the right subtree, etc. Hence, after each step the number of searched nodes will be halved, if the tree is well-balanced.

7.1.2 Regularisation & Optimisation

Having two training samples, one for signal and one for background, every event can now be classified with Equation (7.2), for a given $V(\vec{\mathbf{x}})$. The PDE-RS programme package used in this analysis[1] allows to define $V(\vec{\mathbf{x}})$ as a rectangular box with adjustable edge lengths centred at the coordinates of the event to be

[1]The code used is a modified version of the implementation by B. Koblitz [55].

classified. The optimal choice for the box dimensions is usually left to trial and error, but there are some crucial aspects to consider and which will be discussed in the following sections.

Statistical Uncertainties

From Equation (7.2) the statistical uncertainty on the discriminant $\Delta D(\vec{\boldsymbol{x}})$ is given by:

$$\Delta D(\vec{\boldsymbol{x}}) = \sqrt{\left(\frac{N_b}{(N_s+N_b)^2}\Delta N_s\right)^2 + \left(\frac{N_s}{(N_s+N_b)^2}\Delta N_b\right)^2}, \tag{7.3}$$

In order to regularise statistical uncertainties an additional parameter, N_{min}, is introduced. N_{min} is the minimal number of background plus signal events needed inside of a $V(\vec{\boldsymbol{x}})$ to classify the event, otherwise the event is declared as not classified. Since the box size and N_{min} are highly correlated, one can study the

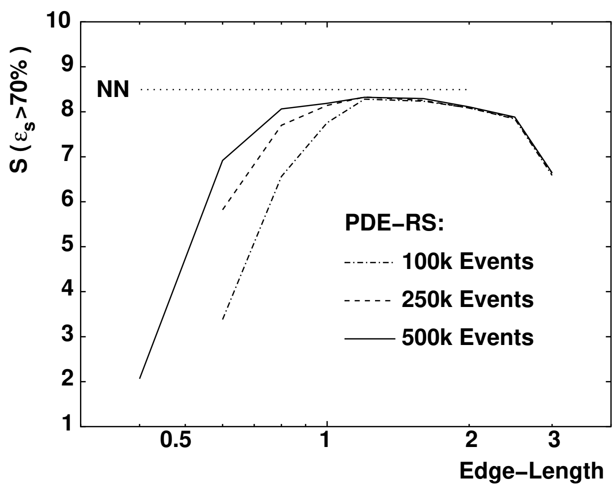

Figure 7.2: The separation power, $S = \epsilon_s/\epsilon_b$, as a function of the edge length for a five-dimensional example (from [55]). The signal efficiency was fixed to 70% and different numbers of training events were evaluated. PDE-RS performance is compared to the ANN method (pointed line).

performance of PDE-RS as function of only one of these parameters. In [55] the authors have shown that the separation power ($S := \epsilon_s/\epsilon_b$) for fixed signal efficiency has only a small dependence on the edge length (see Figure 7.2), if N_{min} and the number of training events are fixed. Figure 7.2 shows that S has a broad plateau and varies only within 20%, when the box size is changed over a large range. The drop at lower edge length is due to the N_{min}-cut, which can be partly compensated by using more training events. The drop towards larger edge lengths is due to the less accurate estimation of the local probability density: The larger the box sizes the more global becomes the estimated probability density.

Normalisation

In general, the normalisation of the signal and background trees is not trivial. In the most simple case, there is only one type of signal class and one type of background class, which means that one class is defined only by a sample of events of the same process and the same kinematic cuts. In this case, signal and background events have to be weighted such that the integrals over the event weights are equal.

In the case, where signal and/or background events consist of different samples corresponding to different luminosities, the weighting factors have to be adjusted according to the luminosities within one class and the overall class weights have to ensure that the weighted integrals over the event weights of the different classes are still equal.

Training & Testing Samples

The most crucial decision in order to achieve an optimal discrimination of signal and background is the choice of the input variables. In general, there is no strict rule, how to find the best (and minimal) set of variables. The choice of input data is usually left to trial and error. But it is important to compare different settings and verify the performances.

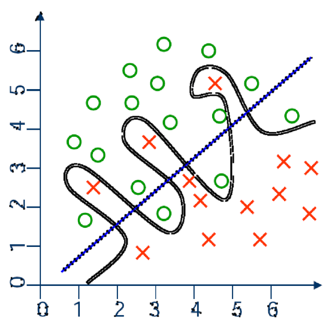

Figure 7.3: Simple example for 'over-learning'. Two different classes are indicated as crosses and open circles. The solid line denotes a cut from a correct generalisation and the open line illustrates a cut from a 'over-learned' algorithm.

For this purpose one should distinguish between the training and the testing samples, otherwise there is a higher risk of 'over-learning'. The algorithm probably identifies artificial or noise structures in the training samples (see Figure 7.3), which gives an incorrect, non-general description of the class phase space. This over-learning can be avoided by using testing samples, which is different from the training sample.

Chapter 8

Event Selection

This chapter describes in detail the selection criteria for the search for neutralino and chargino production. First, a discussion about the expected signal and background topologies is given leading to the general search strategy.

8.1 Search Strategy

In this analysis an inclusive search for neutralino and chargino production is performed. The main production processes are: $e^{\pm}q \rightarrow \tilde{\chi}^0_1 q$, $e^{\pm}q \rightarrow \tilde{\chi}^0_2 q$ and $e^{\pm}q \rightarrow \tilde{\chi}^{\pm}_1 q$. As discussed in Chapter 3 and summarised in Table 3.3 the considered topologies for neutralino and chargino production can be divided into two classes: The electron and the neutrino decay channel. In both event classes at least two high energetic jets are expected in final state. The electron channel is characterised by an electron which can be measured with the calorimeter and the CTD, whereas the neutrino channel is characterised by a neutrino which leaves the detector unobserved and causes an imbalance of the measured energy.

The large masses of the gauginos and the sleptons leave large energy depositions in the calorimeter leading to high total E_T and high E_T jets. These are the main signatures to discriminate SUSY from SM events in both decay channels. Figure 8.1 shows the distributions of the transverse momenta and polar angles of the two jets coming from the neutralino or chargino decay as simulated by SUSYGEN[1]. The highest P_T jet often comes from the struck quark in the proton (see Figure 8.2c-d) and sometimes also the proton remnant can cause a low P_T jet as indicated by the left peak in Figure 8.2c. The η and the ϕ distributions of the jets are also good quantities to discriminate SUSY from DIS and photoproduction

[1]From now on, if not stated otherwise, the sample 'SUSYGEN MC', 'SUSY MC' or 'SUSY sample' refers to a test sample generated with SUSYGEN having the following parameters: $\tan\beta = 30$, $\lambda'_{111} = 1.0$, $M_2 = 150\,\mathrm{GeV}$, $\mu = -400\,\mathrm{GeV}$ and $M_{\tilde{l}} = 100\,\mathrm{GeV}$. For this setting the $\tilde{\chi}^0_1$ is the LSP and has large photino content. The gaugino masses are given as: $M_{\tilde{\chi}^0_1} = 74.6\,\mathrm{GeV}$, $M_{\tilde{\chi}^0_2} \approx M_{\tilde{\chi}^{\pm}_1} = 144.7\,\mathrm{GeV}$.

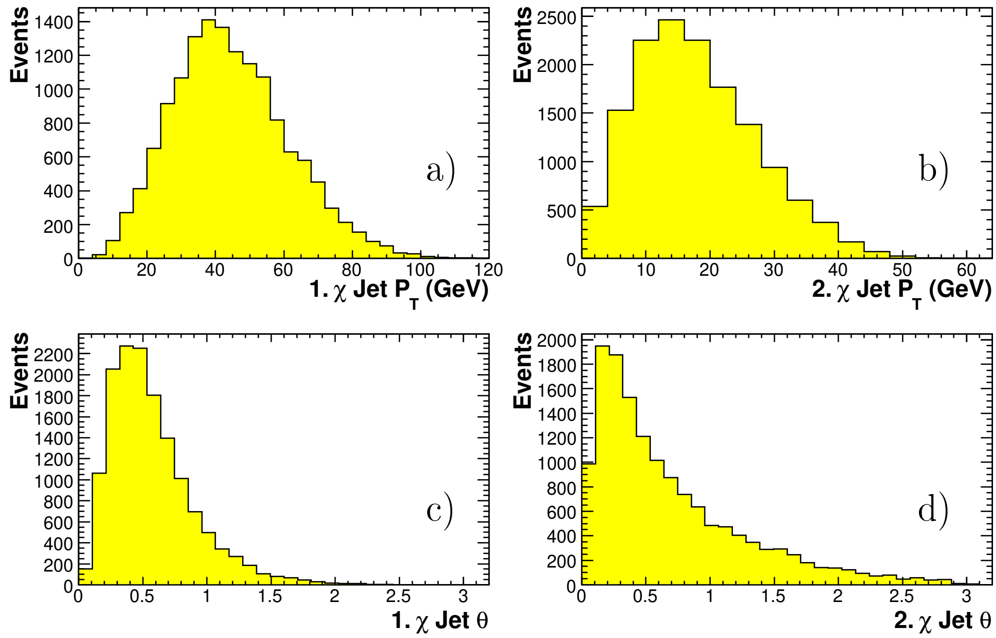

Figure 8.1: Transverse momenta and polar angles of the two jets coming from the gaugino decay as simulated by SUSYGEN. Sleptons and gauginos are generated with masses of $M_{\tilde{l}} = 100\,\text{GeV}$ and $M_{\tilde{\chi}_1^0} = 74.6\,\text{GeV}$, $M_{\tilde{\chi}_2^0} \approx M_{\tilde{\chi}_1^\pm} = 144.7\,\text{GeV}$, respectively.

events. SUSY events typically contain more forward jets than DIS events. The difference in the ϕ distribution can be exploited by the circularity as defined in Section 6.6.

The main background for SUSY events in the electron channel are di-jet and multi-jet NC DIS events, but also photoproduction events, where mismeasurements can fake an electron in the final state. Due to the many forward electrons with very low P_T (see Figure 8.2a), and the ones which are not isolated from hadronic activity (see Figure 8.3), it is not possible to perform a typical NC DIS selection[2] without losing significant signal efficiency. Hence, for this channel the following search strategy is chosen: First, one selects an inclusive high E_T NC DIS sample in the data without so strict requirements for the electron candidate. This sample can be used to control the measurement and the simulation of the energies and angles. Second, di- and multi-jet events are selected from this sample to significantly enhance the potential SUSY content. In order to optimise efficiency and separation power the best discriminating variables are searched for and are given as input for the PDE-RS method.

The 'wrong sign' signature of the final state electron in the electron channel is not exploited in this analysis, since the significance of the track curvature is not well described by the MC. For details see Section 8.3.5.

[2]An example for a typical electron selection at ZEUS can be found in [57].

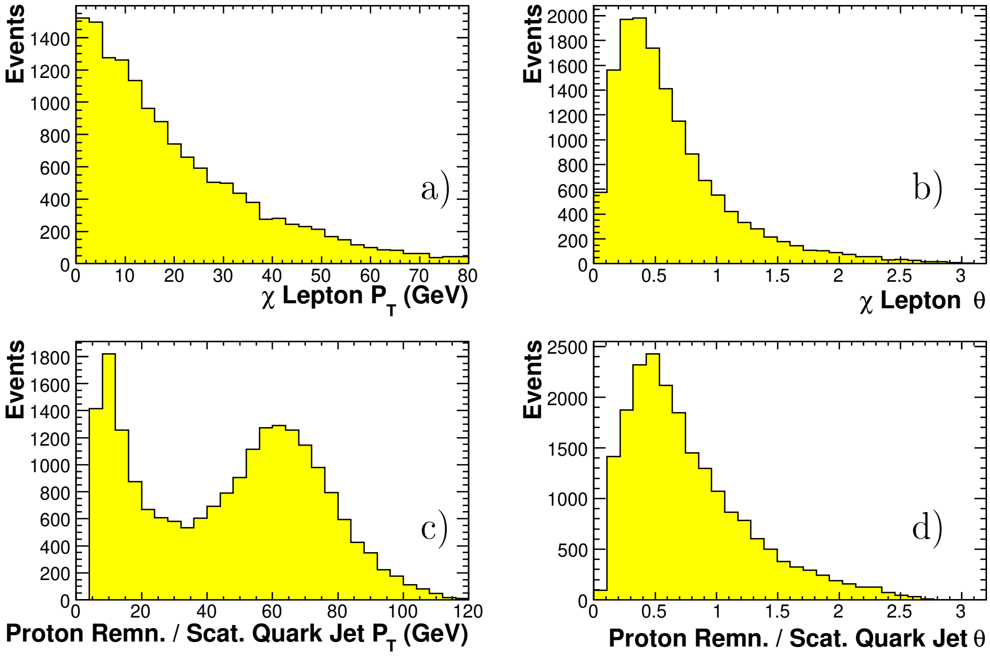

Figure 8.2: Transverse momentum and polar angle of the lepton (electron or neutrino) coming from the gaugino decay (a-b) and the ones caused by the scattered quark or the proton remnant (c-d) as simulated by SUSYGEN. The left peak in c) is dominated by jets from the proton remnant, whereas the right one is dominated by jets caused by the struck quark.

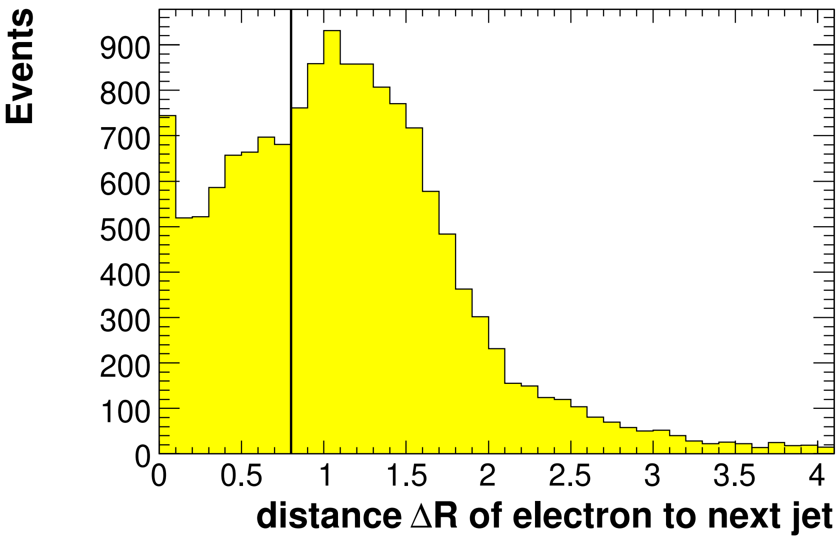

Figure 8.3: The distance $\Delta R(\eta, \phi)$ of the electron candidate to the next jet. The vertical line indicates a typical isolation cut of $\Delta R = 0.8$. Due to a significant efficiency loss, no isolation cut is applied in this analysis.

CC DIS events and photoproduction events, where mismeasurements can fake missing transverse momentum, are the main background for SUSY events in the neutrino channel. The general strategy in this channel is to select an inclusive high E_T CC DIS sample in the data and to find discriminating variables, in order to distinguish SUSY events from SM events. These variables will be used as input for the PDE-RS method to optimise efficiency and separation power.

8.2 Data Set

The analysed data includes events from e^+p and e^-p collisions at a cms energy of 300 and 318 GeV. They were taken in the years 1996 – 2000 and correspond to an integrated luminosity of $\mathcal{L} = 121.1$ pb^{-1}. Table 8.1 shows the energies and luminosities for each run period.

Year	$\boldsymbol{E_e}$(GeV)	$\boldsymbol{E_p}$(GeV)	$\boldsymbol{E_{cms}}$(GeV)	**ZEUS gated** $\mathcal{L}$ (pb^{-1})
96 – ***97*** e^+p	27.5	820	300	38.6
98 – ***99*** e^-p	27.5	920	318	16.7
99 – ***00*** e^+p	27.5	920	318	65.8

Table 8.1: Summary of the data samples used for this analysis.

In the following two Sections 8.3 and 8.4 the selection requirements for the electron and the neutrino channel are described, where the cuts are applied in the same manner to both, data and MC simulations. The normalisation of data and MC distributions is based on the measured luminosities for each run period and the cross section information from the corresponding MC generators, respectively. The ratio of e^+p/e^-p and $E_{cms} = 300/318$ GeV events to the total number of data events are considered by using appropriate weighting factors for the different MC files.

Experimental Background

Apart from SM physics events which are treated as background for SUSY processes, also processes which do not originate from ep interactions are a potential background for searches.

Beam gas reactions are induced by upstream reactions of electrons or protons with the residual gas nuclei or with beam pipe elements. Sometimes, e.g., if the measured vertex is shifted in such a way that the relation between energy and transverse energy is modified with respect to an event at the nominal interaction vertex, they can produce high E_T clusters.

Halo muons originate from the muonic decays of the hadronic products in the beam gas reactions. They produce a 'halo' moving in the direction of the proton beam. Halo muon events are characterised by energy deposits aligned in a narrow cylinder parallel to the beam pipe and not crossing the nominal interaction point.

High energy muons are also produced in cosmic showers in the atmosphere. They can traverse the detector and leave traces at two diametrical located positions in the muon detector components without crossing the nominal interaction point.

The HERA clock runs with a frequency of 10.4 MHz leading to potential electron-proton collisions every 96 ns. If non-*ep* processes, as described above, are randomly overlaid with *ep* processes, these events are not rejected at the trigger level.

8.3 Electron Channel

8.3.1 NC DIS Preselection

The NC DIS control selection aims to select an inclusive NC DIS sample from the data, which has potential large SUSY content.

Selection Criteria

The ZEUS data acquisition system pre-classifies the events which passes the three trigger levels and stores the results in so called data summary tapes (DST) bits, which can be considered as a pseudo fourth level trigger bit. These bits allow a fast access to predefined classes of events.

- DST32
  The DST bit 32 (DST32) is used to select NC DIS events in the data. The main criteria is a good electron candidate and a high $E - p_z$, reconstructed at the third trigger level. A detailed description of the DST32 is given in Appendix A.1.

Additional to DST32 the following offline cuts for the NC DIS control selection are applied:

- $|z_{\text{vtx}}| < 40\,\text{cm}$
  This cut reduces background from non-*ep* interactions and is also needed for an accurate calculation of kinematic variables.

- $44\,\text{GeV} < E - p_z < 64\,\text{GeV}$
  In NC DIS and SUSY electron events the $E - p_z$ distribution peaks at

twice the initial electron energy (55 GeV). The lower threshold removes photoproduction events, while the upper one rejects non-ep background.

- $E_T > 60\,\text{GeV}$
  This cut enhances the ratio of signal events within the data and removes general low E_T background.

- $y_{\text{DA}} > 0.3$
  Also this cut enhances the signal and additionally rejects photoproduction events.

- $P_T < 20\,\text{GeV}$
  CC DIS and non-ep background is removed by this criteria.

- $P_T^{\text{trk}} > 100\,\text{MeV}$
  CTD hits caused by noise or mismeasurements can be misinterpreted as tracks. Many of these tracks are discarded by this requirement.

- $\geq$ 1 good jet
  At least one good jet. The jet requirements are listed below.

- $\geq$ 1 good electron candidate
  One good electron candidate. The electron requirements are listed below.

Good Jets

The following criteria are required for all measured jets:

- $E_T^{\text{jet}} > 10\,\text{GeV}$ **AND** $-0.5 < \eta^{\text{jet}} < 2.7$

For the highest and second highest E_T jet these thresholds are required:

- $E_T^{j1} > 25\,\text{GeV}$
- $E_T^{j2} > 12\,\text{GeV}$

Electron Candidates

These are the requirements for an electron candidate using the EM finder:

- $P_{\text{Grand}} > 0.001$ (for the definition of P_{Grand} see Section 6.5)
- $E^e > 10\,\text{GeV}$

- Forward electrons ($3° < \theta^e < 17°$):

- $P_T^e > 15\,\mathrm{GeV}$
  There are no track requirements for the forward region due to the limited acceptance of the CTD. This is compensated by a higher P_T^e cut, which is still below a typical cut of 30 GeV as applied in other analyses.

- Barrel electrons ($17° < \theta^e < 115°$):

  - $P_T^e > 6\,\mathrm{GeV}$

  - Number of CTD super-layers ≥ 3
    In the region covered by the CTD, one track should be pointing to the electron energy cluster in the calorimeter. This track should have traversed at least three super-layers of the CTD.

  - $P_T^{\mathrm{trk}}/E^e > 0.15$
    The measured transverse momentum of the track is required to have at least 15% of the electron energy.

  - trkDCA $< 8\,\mathrm{cm}$
    trkDCA is the distance of closest approach of the track to the primary vertex.

These criteria for electron candidates are less strict than usual NC DIS electron requirements at ZEUS, in order to gain higher signal efficiencies. No isolation requirement for the electron cluster is required and for forward electrons the P_T threshold is relaxed.

The control distributions after these cuts are depicted in Figures 8.4-8.7. They show a good agreement between data and MC, only the η^{j2} distribution shows some deviations. Also the distribution of the circularity (see Figure 8.7b) is acceptable. One should notice that this plot has a logarithmic scale. The difference between data and MC for very low circularity values close to zero originates from only very small systematic variations.

The event statistics is listed in Table 8.2 and Table 8.3. 4908 events are selected in the data, while 4838.8 ± 69.6 (stat.) SM events are expected from MC simulation (see Table 8.3).

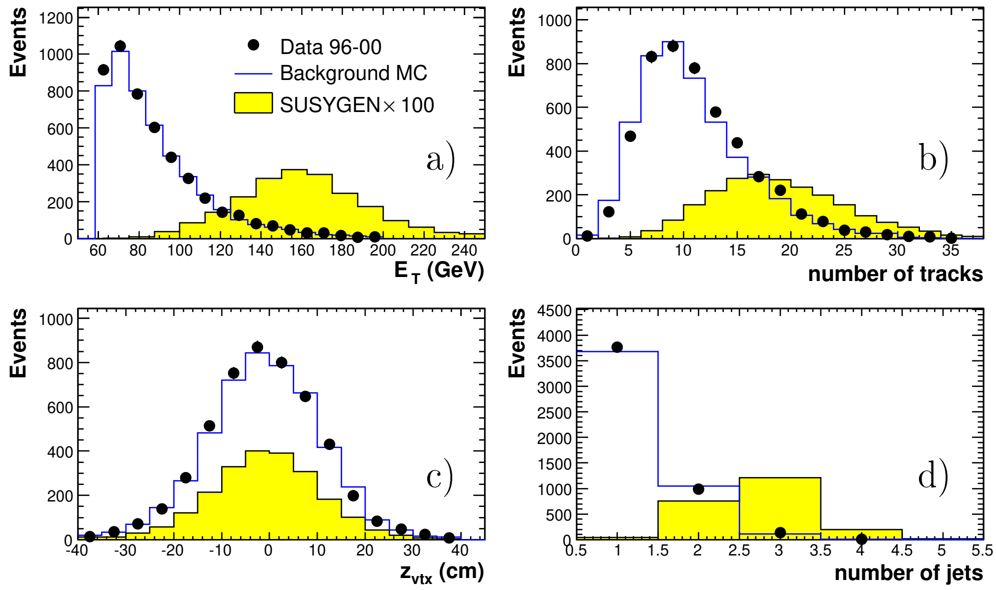

Figure 8.4: Global E_T (a), total number of tracks (b), z position of the vertex (c) and total number of jets (d) after the **NC preselection**. The dots represent data, the open histograms denote the background MC and the filled histograms an example SUSYGEN sample, scaled by 100.

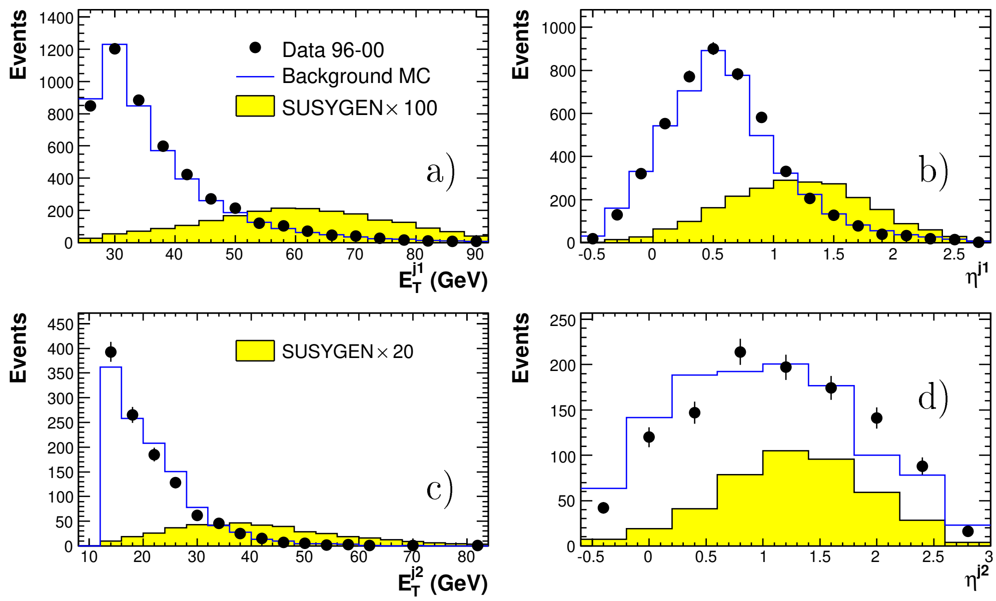

Figure 8.5: Distributions of the transverse energy and pseudo-rapidity for the highest and second highest E_T jet after the **NC preselection**. The dots represent data, the open histograms denote the background MC and the filled histograms an example SUSYGEN sample, scaled by 100.

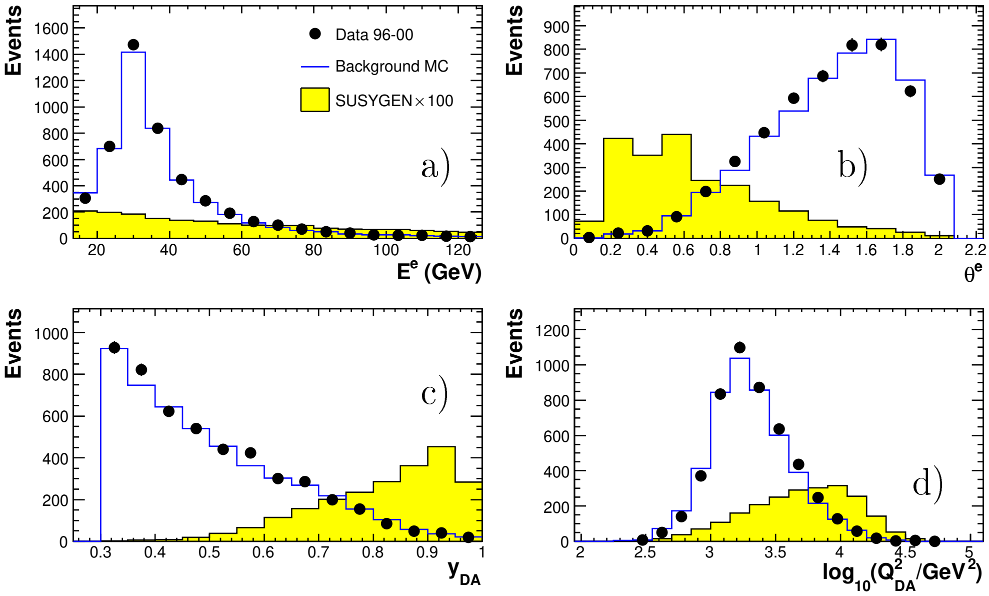

Figure 8.6: Distributions of the electron energy and polar angle, y_{DA} and the logarithm of Q^2 after the **NC preselection**. The dots represent data, the open histograms denote the background MC and the filled histograms an example SUSYGEN sample, scaled by 100.

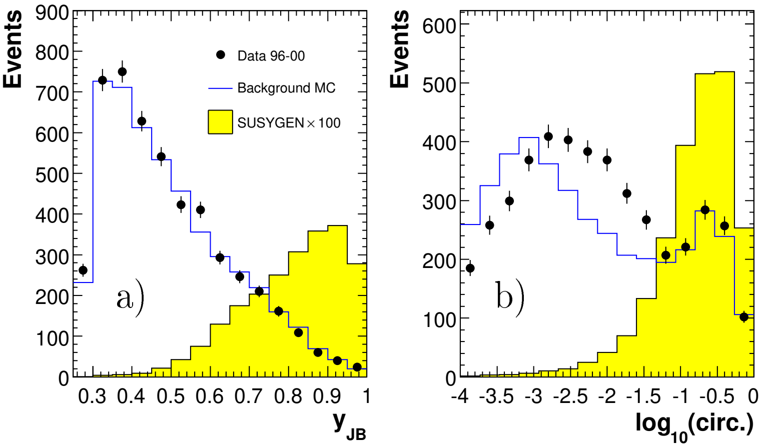

Figure 8.7: Distributions of the hadronic y_{JB} and the logarithm of the circularity after the **NC preselection**. The dots represent data, the open histograms denote the background MC and the filled histograms an example SUSYGEN sample, scaled by 100.

8.3.2 Selection of di- and multi-jet Events

On top of the NC preselection one further cut is applied:

- ≥ 2 good jets

This cut aims to gain a further enhancement of the SUSY signal. Figures 8.8-8.11 show the distribution after the multi-jet selection. The MC simulation is not able to describe the data for the electron energy (see Figure 8.10a), electron polar angle (see Figure 8.10b) and the Q^2_{DA} (see Figure 8.10d) distributions. Also the η^{j2} distribution still shows some deviations, whereas other jet distributions and y_{DA} are well described.

The differences most probably arises from the fact that the NC multi-jet events in this analysis are simulated by a MC which is based on first order of α_s matrix elements and gluon radiation according to the CDM. Higher order effects are not simulated. This may have an effect on the jet and electron angle distributions. But the real reason for this discrepancy has to be investigated in more detail in the future. However, the second jet η and the electron polar angle are not used to discriminate signal from SM events (see Section 8.3.4).

The event statistics is listed in Table 8.2 and Table 8.3. 1139 events are selected in the data, while 1163.3$\pm$34.1 (stat.) SM events are expected from MC simulation. The efficiency times branching ratio for the different SUSY scenarios lie typically between 5% and 35%.

Selection Cut	NC qq400 Eff.	SUSY Eff.×BR	Data Events
DST32	100.0%	100.0%	196,466
$E - p_z$	88.1%	84.5%	152,610
njet$\geq$ ***1***	38.9%	84.3%	98,170
$\boldsymbol{E_T}$	35.9%	84.1%	30,714
$\mathbf{z}_{\mathrm{vtx}}$	34.2%	80.0%	30,341
$\boldsymbol{P_T}$	34.1%	64.1%	30,268
Electron cand.	28.9%	26.3%	22,744
$\boldsymbol{y}_{\mathrm{DA}}$	20.8%	25.0%	20,968
$\boldsymbol{E_T^{j1}}$	12.9%	23.6%	8,144
$\boldsymbol{E_T^{j2}}$	5.5% 4838.8 $\pm$ 69.6 (stat.)	23.1%	4,908
njet$\geq$ ***2***	1.2% 1,163.3 $\pm$ 34.1 (stat.)	22.6%	1139

Table 8.2: MC efficiency and number of events in data which passed the cuts. 'NC qq400' denotes NC DIS MC with the kinematic cut $Q^2 > 400\,\mathrm{GeV}^2$.

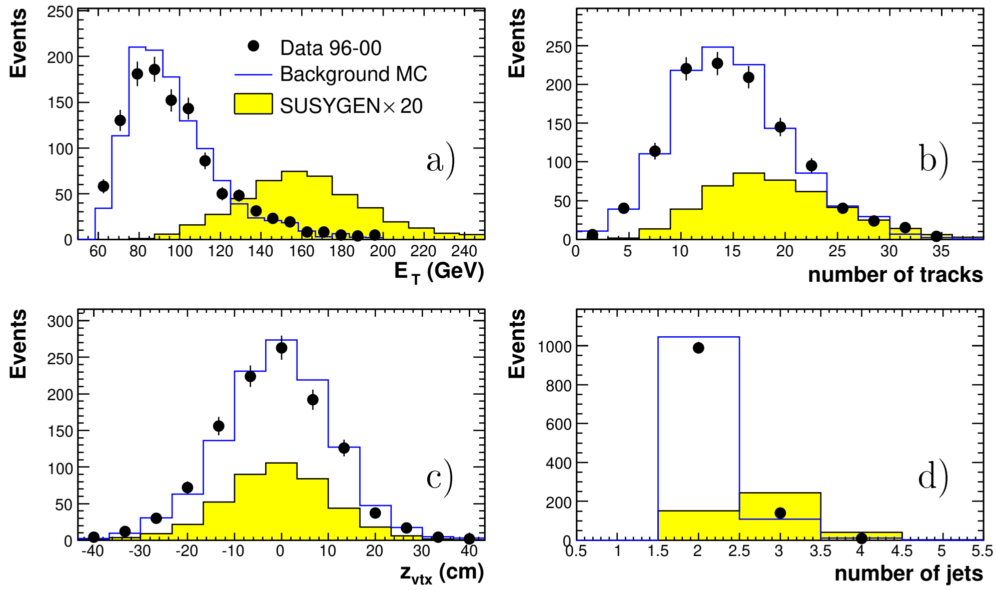

Figure 8.8: Global E_T (a), total number of tracks (b), z position of the vertex (c) and total number of jets (d) after the **NC multi-jet selection**. The dots represent data, the open histograms denote the background MC and the filled histograms an example SUSYGEN sample, scaled by 20.

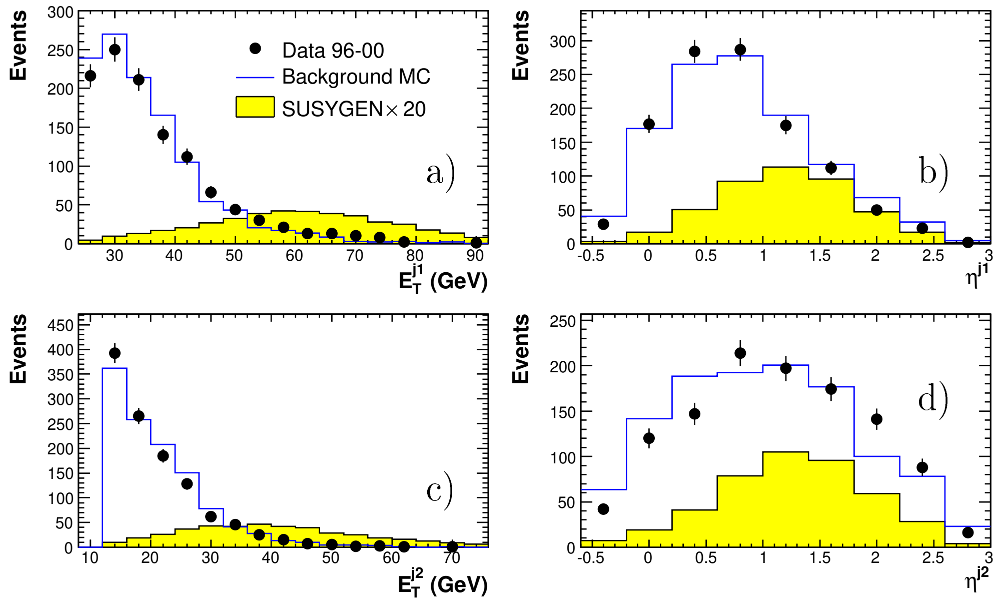

Figure 8.9: Distributions of the transverse energy and pseudo-rapidity for the highest and second highest E_T jet after the **NC multi-jet selection**. The dots represent data, the open histograms denote the background MC and the filled histograms an example SUSYGEN sample, scaled by 20. Notice that c) and d) are identical to Figures 8.5c-d.

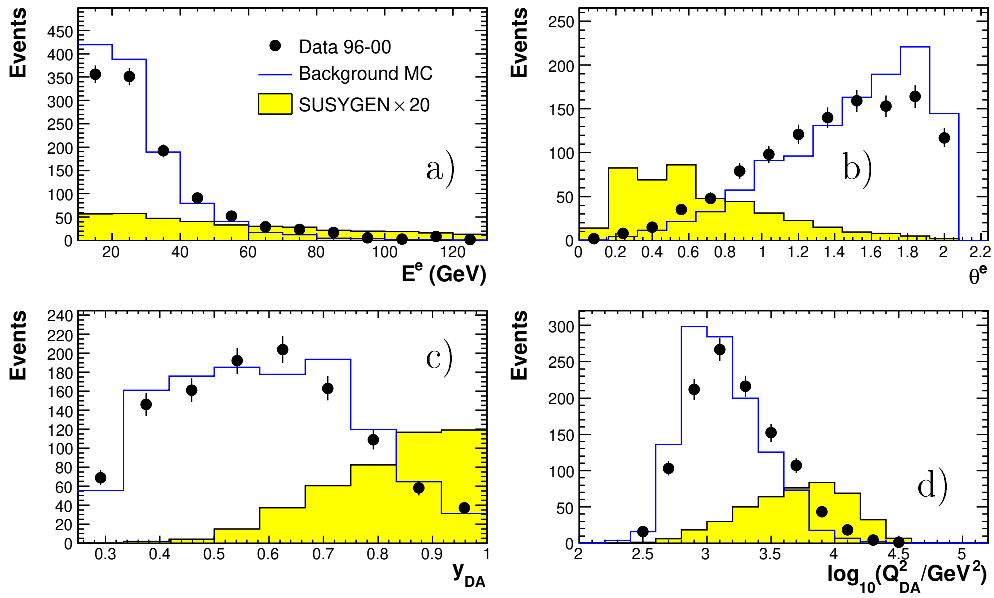

Figure 8.10: Distributions of the electron energy and polar angle, y_{DA} and the logarithm of Q^2 after the **NC multi-jet selection**. The dots represent data, the open histograms denote the background MC and the filled histograms an example SUSYGEN sample, scaled by 20.

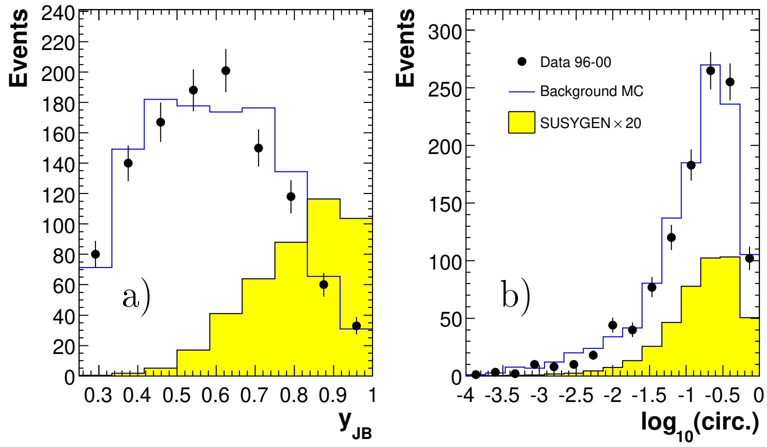

Figure 8.11: Distributions of the hadronic y_{JB} and the logarithm of the circularity after the **NC multi-jet selection**. The dots represent data, the open histograms denote the background MC and the filled histograms an example SUSYGEN sample, scaled by 20.

	Number of expected and observed Events				
	NC DIS	γp	**other**	**SUSY**	**Data**
Control Sel.	4,767.6	70.5	1.2	22.3	4,908
njet$\geq$ 2	1,101.4	60.9	1.0	21.9	1,139

Table 8.3: Number of observed and expected events after the NC preselection cuts.

8.3.3 Reweighting di- and multi-jet Events

Since the MC simulation is not able to describe the data for the electron variables, the MC distributions are reweighted in the way that they fit the electron polar angle distribution of the data (see Figure 8.14b). After the reweighting, also the distributions of the electron energy (see Figure 8.14a) and Q^2 (see Figure 8.14d) agree better now. And there is no big change in all other distributions (see Figures 8.12-8.15).

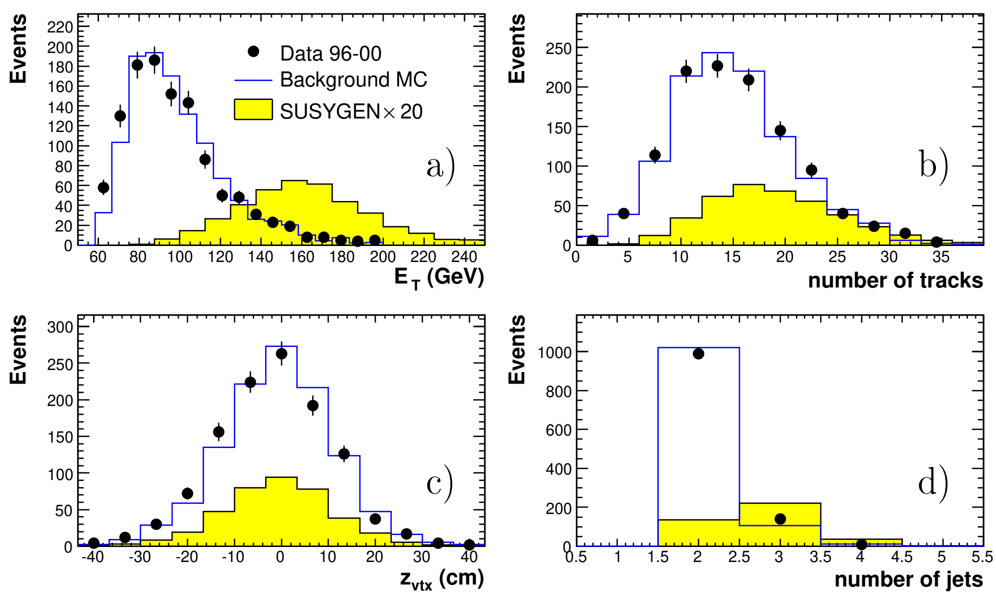

Figure 8.12: Global E_T (a), total number of tracks (b), z position of the vertex (c) and total number of jets (d) after **NC reweighting**. The dots represent data, the open histograms denote the background MC and the filled histograms an example SUSYGEN sample, scaled by one 20.

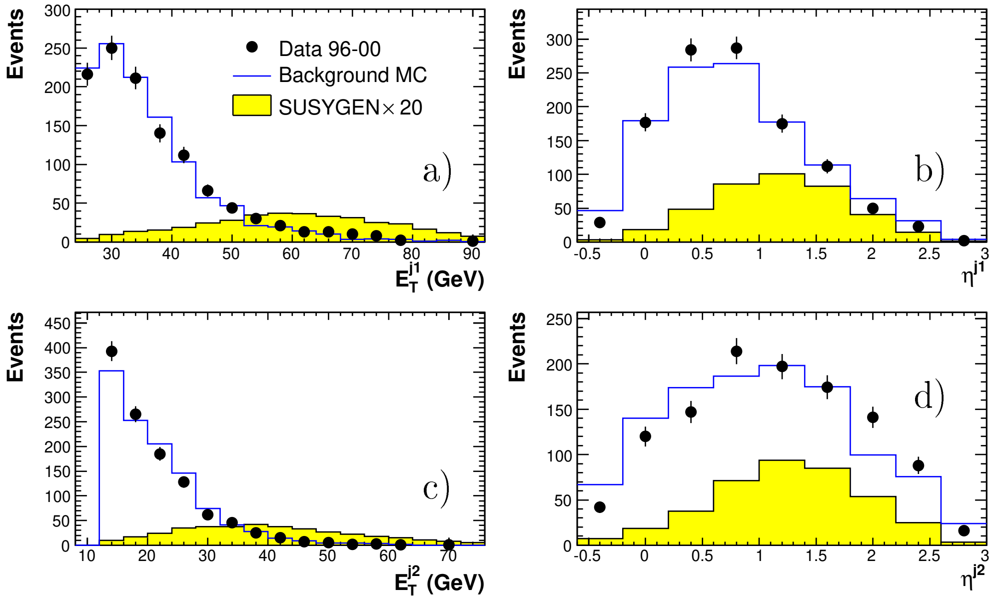

Figure 8.13: Distributions of the transverse energy and pseudo-rapidity for the highest and second highest E_T jet after **NC reweighting**. The dots represent data, the open histograms denote the background MC and the filled histograms an example SUSYGEN sample, scaled by 20.

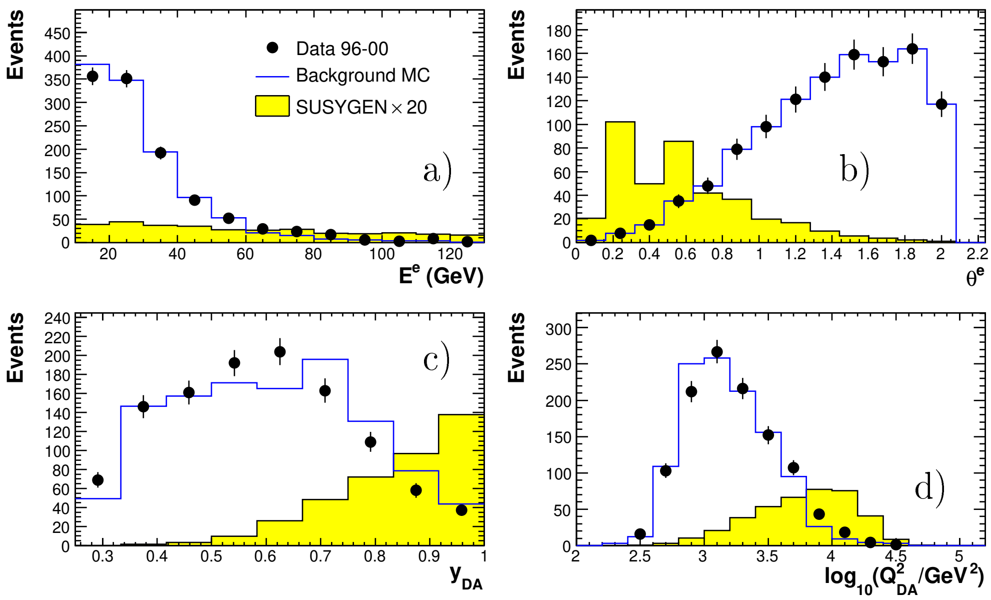

Figure 8.14: Distributions of the electron energy and polar, $y_{\rm DA}$ and the logarithm of $Q^2_{\rm DA}$ after **NC reweighting**. The dots represent data, the open histograms denote the background MC and the filled histograms an example SUSYGEN sample, scaled by 20.

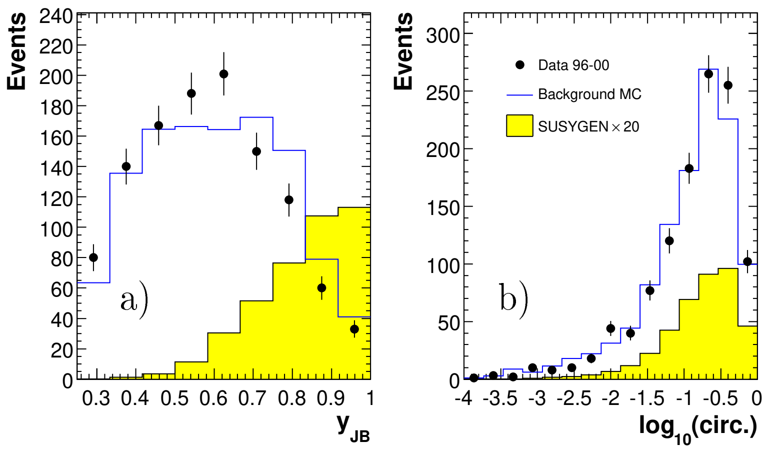

Figure 8.15: Distributions of the hadronic y_{JB} and the logarithm of the circularity after **NC reweighting**. The dots represent data, the open histograms denote the background MC and the filled histograms an example SUSYGEN sample, scaled by 20.

8.3.4 Multivariate Event Classification

In order to optimise separation power and efficiency the PDE-RS method is used to discriminate signal events from background events. For this purpose an extensive study is done to find the best combination of variables and box sizes. The decision for the final set of variables and box sizes is based on trial and error. But the number of parameter settings is constrained by the following requirements:

- Use of non-reweighted events.
  The η^{j2} and the electron polar angle are not used, since they are not well described by the MC. The discrepancies can be partly regularised by the reweighting procedure. However, the non-reweighted events after the multijet selection are used to discriminate SUSY from SM events and the differences in the electron distributions are considered as a source of systematic uncertainties (see Section 9.1).

- The distribution of a single variable should already have some degree of separation power.

- Not more than 7 input variables.

- Global E_T, E_T^{j1} and total number of tracks are fix input variables, since these variables obviously show good separation power.

- If assuming a uniform distribution of signal and background events in the n-dimensional input space, the box sizes are chosen, that each one would contain at least 50 events. This box setting ensures that most of the calculated boxes have at least 30 events.

The best setting is found to be the one summarised in Table 8.4. It may be surprising that this list contains the circularity as it seems not to have any separation power itself. But the survey has shown that it very often increases the separation in combination with other variables. As an example see Figure 8.16. In this figure the rectangular box denotes 1-dim. cuts, while the elliptical curve is an example for a more efficient 2-dim. cut, which is a possible result of the PDE-RS. One can clearly see that this kind of optimisation using the circularity can improve the separation power significantly without losing much efficiency.

Input	E_T	$\log_{10}$(circ.)	y_{JB}	ntrk	E_T^{j1}	E_T^{j2}
Edge length	40 GeV	1.0	0.2	8	20 GeV	16 GeV

Table 8.4: Final PDE-RS setting for the electron channel.

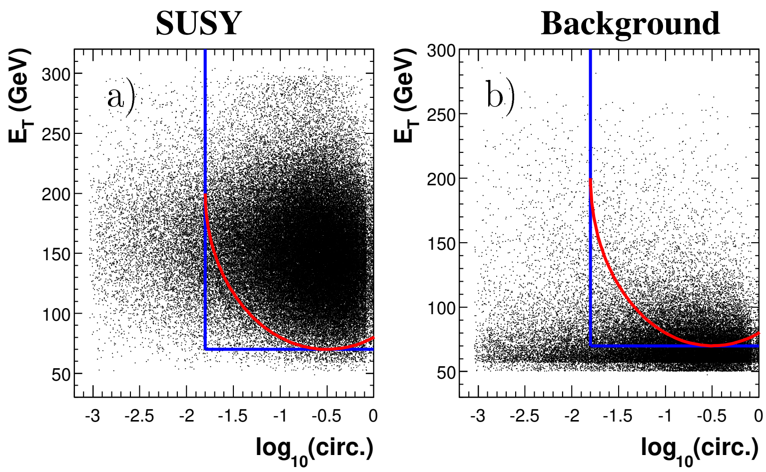

Figure 8.16: Correlation of the global E_T with the circularity for the signal (a) and the background (b). The rectangular box indicates 1-dim. cuts. The elliptical curve is an example for a more efficient 2-dim. cut.

For the training samples most of the preselection cuts are relaxed in order to gain more statistics. The background training sample is a superset of the background test sample, due to statistical limitations. It consists of $48,407$ events selected from all NC DIS, γp and CC DIS MC files. The signal training sample contains a mixture of different parameter points and does not intersect with the signal test sample. It consists of $106,458$ events. The normalisation of the samples is applied as described in Sect. 7.1.2.

The result of the PDE-RS analysis is depicted in Figure 8.17. In this plot the test SUSY sample is scaled by a factor of 6. The performance of the PDE-RS can be seen nicely in Figure 8.18, where efficiency and signal/background ratio are defined as:

$$\text{efficiency} := \frac{\text{number of SUSY events after discriminant cut}}{\text{number of SUSY events after preselection}} \tag{8.1}$$

$$\text{sig./bg.} := \frac{\text{number of SUSY events after discriminant cut}}{\text{number of background events after discriminant cut}} \tag{8.2}$$

The MC and the data distribution agree well in all discriminant regions. There is no significant excess in the data at high discriminant values, which is supposed to be the signal region: 33 events with a discriminant larger than 0.96 are observed in the data, while 29.8 ± 5.5 (stat.) are expected from SM background.

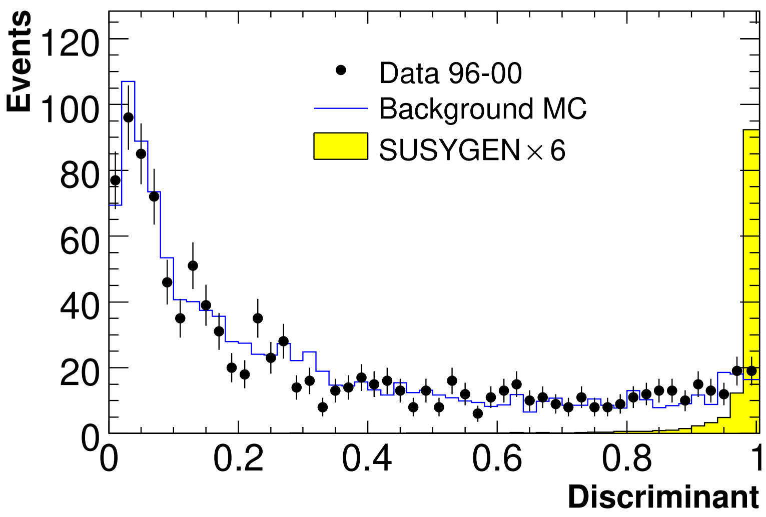

Figure 8.17: Discriminant distribution for the electron channel.

8.3.5 'Wrong' Charge Electron

In fifty percent of the gaugino decays the final state electron has a different charge than the initial electron. This striking signature is expected to be almost background free. The significance of the track charge measurement[3], $\sigma(Q/R) = \text{cov}(Q/R)/(Q/R)$, multiplied with the measured track charge for e^+p collisions is shown in Figure 8.19.

If one requires that a 'wrong' sign electron track candidate should have a significance of at least 2σ (events left to the vertical line in Figure 8.19), 15 events are found in the e^+p data, 12.0 ± 3.5 (stat.) are expected from SM and 2.3 events are expected from a sample SUSY scenario. In the e^-p data, 2 events are observed,

[3] See Section 6.3.

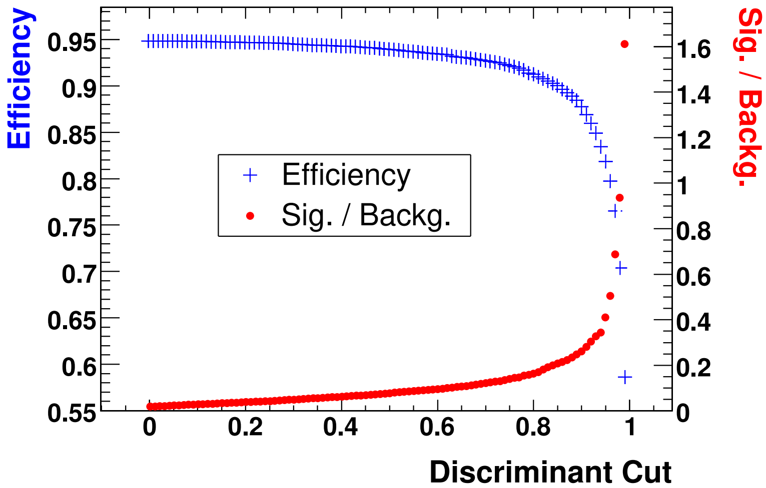

Figure 8.18: Efficiency and signal/background ratio as a function of a discriminant cut in the electron channel.

while 1.1 ± 1.0 (stat.) are expected from SM background and 0.4 events are expected from a sample SUSY scenario. The SM expectations agree well with the observed events in the data.

Since the bin-by-bin description of the data by the MC is rather poor, the exclusive 'wrong' sign electron channel is not considered in the limit setting procedure (see Section 9.2). However, from the given numbers of observed and expected events one does not expect a significantly better sensitivity from an analysis of two separate electron channels than from an inclusive electron channel analysis.

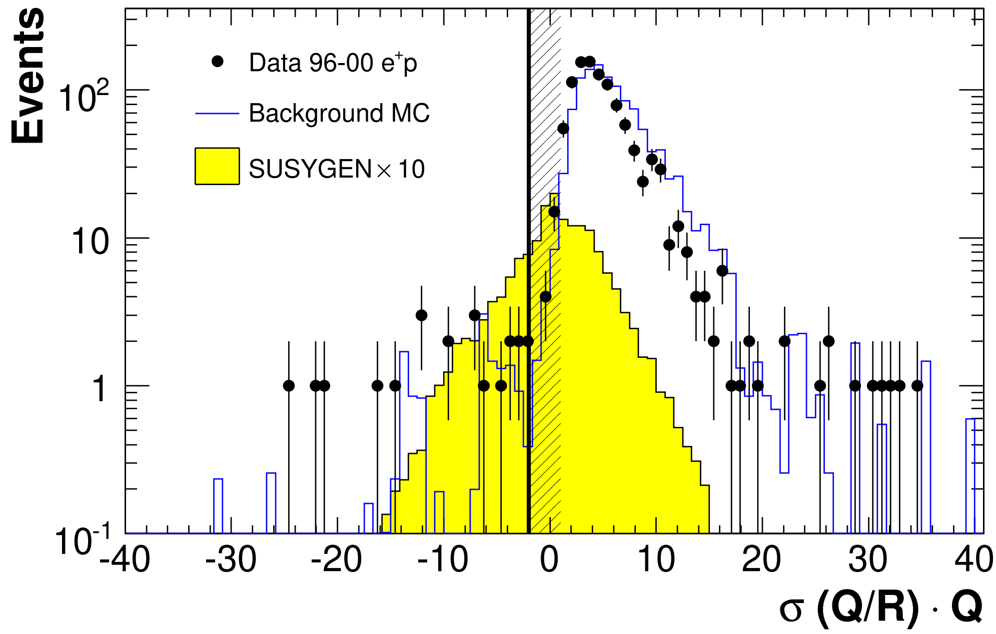

Figure 8.19: The significance of the track charge measurement ($\sigma(Q/R)$) multiplied with the measured track charge for e^+p collisions. The vertical line indicates the cut at 2σ for 'wrong' charge electron candidates.

8.4 Neutrino Channel

8.4.1 Preselection

The neutrino channel preselection aims to select an inclusive CC DIS sample from the data, which has potential large SUSY content.

Selection Criteria

- DST32
  The DST bit 34 (DST32) is used to select CC DIS events in the data. Events with large missing transverse momentum are required and background is rejected at the third level trigger. A detailed description of the DST34 is given in Appendix A.2.

The neutrino channel is much more contaminated with background events than the electron channel. Therefor many cleaning cuts are applied in addition to the physics cuts:

- $|z_{\text{vtx}}| < 40\,\text{cm}$
  This cut reduces background from non-ep interactions and is needed for an accurate calculation of kinematic variables.

- $E_T > 50\,\mathrm{GeV}$
  This cut enhances the ratio of signal events within the data and removes general low E_T background.

- $0.3 < y_{\mathrm{JB}} < 0.98$
  Also this cut enhances the signal and additionally rejects photoproduction events and non-ep background.

- $P_T > 20\,\mathrm{GeV}$ **AND** $P_T^{\mathrm{ex1ir}} > 18\,\mathrm{GeV}$
  The neutrino leaves the detector unobserved leading to missing transverse momentum. Analogous to the electron channel, a significant number of neutrinos are expected to have low P_T. Unfortunately, a relatively high missing P_T cut is unavoidable in order to reduce the background, which leads to a significant efficiency loss. P_T^{ex1ir} is the missing transverse momentum excluding the first inner ring of the FCAL. It aims to exclude the energies caused by the proton remnant.

- ≥ 1 good jet
  At least one good jet. The jet requirements are listed below.

- Reject events with electron candidates
  The electron requirements are listed below.

- Good-tracks requirements
  The good-tracks requirements are listed below.

- Cleaning Cuts
  The cleaning cuts are described below.

Good Jets

- $E_T^{\mathrm{jet}} > 10\,\mathrm{GeV}$ **AND** $-0.5 < \eta^{\mathrm{jet}} < 2.7$

Electron Rejection

Electron requirements are relaxed compared to the electron channel.

- $P_{\mathrm{Grand}} > 0.001$ (for the definition of P_{Grand} see Section 6.5)
- Forward electrons ($3^\circ < \theta^e < 17^\circ$):
  - $P_T^e > 6\,\mathrm{GeV}$
- Barrel electrons ($17^\circ < \theta^e < 115^\circ$):
  - $P_T^e > 6\,\mathrm{GeV}$

– Number of CTD super-layers ≥ 3
– $P_T^{\mathrm{trk}} > 1\,\mathrm{GeV}$
  The matched track is required to have a tranverse momentum of at least 1 GeV.
– trkDCA $< 8\,\mathrm{cm}$

Good-tracks Requirements

All tracks are required to be assigned to the primary vertex. The tracks are classified as 'normal' or 'good' tracks, if their transverse momentum is at least 100 or 200 MeV, respectively:

- $P_T^{\mathrm{trk}} > 100\,\mathrm{MeV}$
- $P_T^{\mathrm{goodtrk}} > 200\,\mathrm{MeV}$

For two different kinematic regions, all events which do not fulfil the following requirements are rejected:
$P_T > 30\,\mathrm{GeV}$

- $N_{\mathrm{good}}^{\mathrm{trk}} \geq 1$
- $N_{\mathrm{good}}^{\mathrm{trk}} > \frac{1}{4}(N^{\mathrm{trk}} - 20)$

$P_T < 30\,\mathrm{GeV}$

- $N_{\mathrm{good}}^{\mathrm{trk}} \geq 3$
- $N_{\mathrm{good}}^{\mathrm{trk}} > (N^{\mathrm{trk}} - 5)$ **AND** $N_{\mathrm{good}}^{\mathrm{trk}} > 10$

A beam gas event tends to contain many tracks, but only a few of them have a transverse momentum larger than 200 MeV and are assigned to the primary vertex. For more details about the good-tracks requirements see [58].

Cleaning Cuts

- HAC Fraction cuts
  These cuts rejects halo muon and cosmic muon events. All events which fulfil the following requirements are vetoed:

$$\begin{array}{lll} E_{\mathrm{CAL}}^{\mathrm{EMC}}/E_{\mathrm{CAL}} & < 0.05 & , \\ E_{\mathrm{BCAL}}^{\mathrm{HAC}}/E_{\mathrm{BCAL}} & > 0.9 & , \text{ if } E_{\mathrm{BCAL}} > 5\,\mathrm{GeV}, \\ E_{\mathrm{RCAL}}^{\mathrm{HAC}}/E_{\mathrm{RCAL}} & > 0.9 & , \text{ if } E_{\mathrm{RCAL}} > 5\,\mathrm{GeV}, \end{array}$$

where HAC denotes all hadronic type cells of the calorimeter (HAC1, HAC2) and EMC corresponds to the electromagnetic cells. RCAL and BCAL indicate the rear and the barrel part of the calorimeter. CAL corresponds to all parts of the calorimeter. Halo muons typically fly parallel to the beam pipe, depositing a characteristic high fraction in the electromagnetic or hadronic parts of the calorimeter.

- Timing Cuts
Events which satisfy one of the following timing requirements are vetoed in order to reject cosmic muon events:

$$\begin{array}{lll}
t_{\mathrm{FCAL}} > -99 \text{ ns} & \textbf{AND } |t_{\mathrm{FCAL}}| > 5 \text{ ns}, & \text{if } \mathrm{E}_{\mathrm{FCAL}} > 4\,\mathrm{GeV}, \\
t_{\mathrm{BCAL}} > -99 \text{ ns} & \textbf{AND } |t_{\mathrm{BCAL}}| > 5 \text{ ns}, & \text{if } \mathrm{E}_{\mathrm{BCAL}} > 4\,\mathrm{GeV}, \\
t_{\mathrm{RCAL}} > -99 \text{ ns} & \textbf{AND } |t_{\mathrm{RCAL}}| > 5 \text{ ns}, & \text{if } \mathrm{E}_{\mathrm{RCAL}} > 4\,\mathrm{GeV}, \\
t_{\mathrm{FCAL}} > -99 \text{ ns} & \textbf{AND } t_{\mathrm{RCAL}} > -99 \text{ ns} & \\
 & \textbf{AND } |t_{\mathrm{FCAL-RCAL}}| > 6 \text{ ns}, & \text{if } \mathrm{E}_{\mathrm{CAL}} > 5\,\mathrm{GeV}, \\
t_u > -99 \text{ ns} & \textbf{AND } t_d > -99 \text{ ns} & \\
 & \textbf{AND } |t_u - t_d| > 6 \text{ ns}, & \text{if } \mathrm{E}_{\mathrm{CAL}} > 5\,\mathrm{GeV},
\end{array}$$

where t_X corresponds to the duration between the time when an ep interaction at the nominal interaction point has occurred and the time, when a particle hits the part X of the calorimeter. For example, $t_u - t_d$ and $t_{\mathrm{FCAL-RCAL}}$ are the durations between a hit in the upper and the lower half of CAL and the time between a hit in the FCAL and the RCAL, respectively. These cuts are made to reject too early or too late cosmic events with respect to the nominal ep collision time.

- Cosmic Muon Rejection
For events with exactly two tracks fitted to the primary vertex, a cut on the opening angle between the two tracks is made.

$$\Delta\Omega\{\vec{\boldsymbol{p}}_{\mathrm{trk1}}, \vec{\boldsymbol{p}}_{\mathrm{trk2}}\} < 178^\circ, \tag{8.3}$$

if $|\vec{\boldsymbol{p}}_{\mathrm{trk1}}|$, $|\vec{\boldsymbol{p}}_{\mathrm{trk2}}| > 200\,\mathrm{MeV}$, with $\cos\Delta\Omega\{\vec{\boldsymbol{p}}_{\mathrm{trk1}}, \vec{\boldsymbol{p}}_{\mathrm{trk2}}\} = \frac{\vec{\boldsymbol{p}}_{\mathrm{trk1}} \cdot \vec{\boldsymbol{p}}_{\mathrm{trk2}}}{|\vec{\boldsymbol{p}}_{\mathrm{trk1}}| \cdot |\vec{\boldsymbol{p}}_{\mathrm{trk2}}|}$, where $|\vec{\boldsymbol{p}}_{\mathrm{trk1}}|$ and $|\vec{\boldsymbol{p}}_{\mathrm{trk2}}|$ are the reconstructed momentum vectors of the CTD tracks.

- Visual Scan
Many cosmic muon and halo muon events, which are not rejected by appropriate background rejection cuts, can relatively easily be identified by a visual scan. Halo muon events are characterised by a trace of energy deposits in the calorimeter parallel to the beam pipe, indicating that they do not originate from the nominal interaction point. High energetic cosmic muons usually fly completely through the detector leaving traces at two diametrical located positions in the muon detector components. Additionally, the interpolation of this trace is distinctly not going through the nominal interaction point. Only seven events are rejected by this scan.

The control distributions after the preselection cuts are depicted in Figures 8.20-8.22 and show a good agreement between data and MC.

The event statistics is listed in Table 8.5. 469 events are selected in the data, while 474.1 ± 21.8 (stat.) SM events are expected from MC simulation (see Table 8.6). The efficiency times branching ratio for the different SUSY scenarios lie typically between 5% and 50%.

Selection Cut	CC qq100 Eff.	SUSY Eff.×BR	Data Events
DST34	98.7%	58.9%	275,065
Visual Scan	—	—	275,058
njet$\geq$ *1*	92.7%	58.8%	174,063
$\boldsymbol{E_T}$	62.0%	58.7%	167,347
$\boldsymbol{z}_{\mathrm{vtx}}$	58.4%	58.6%	158,398
$\boldsymbol{y}_{\mathrm{JB}}$	32.5%	50.4%	112,779
$\boldsymbol{Q^2_{\mathrm{JB}}}$	32.5%	50.3%	81,926
$\boldsymbol{P_T}$	29.0%	27.7%	65,968
$\boldsymbol{P_T^{\mathrm{ex1ir}}}$	28.5%	26.3%	65,533
HAC Frac.	28.5%	26.3%	35,468
Cal Timing	28.5%	26.3%	26,547
ngood trks	25.8%	25.1%	504
Cosmics	25.8%	25.1%	504
Electron rejection	25.2% 474.1 ± 21.8 (stat.)	23.5%	469

Table 8.5: MC efficiency and number of events in data which passed the cuts. 'CC qq100' denotes CC DIS MC with the kinematic cut $Q^2 > 100\,\mathrm{GeV}^2$.

	Number of expected and observed Events				
	CC DIS	γp	**other**	**SUSY**	**Data**
Selection	466.8	4.3	3.0	22.7	469

Table 8.6: Number of observed and expected events after the CC preselection.

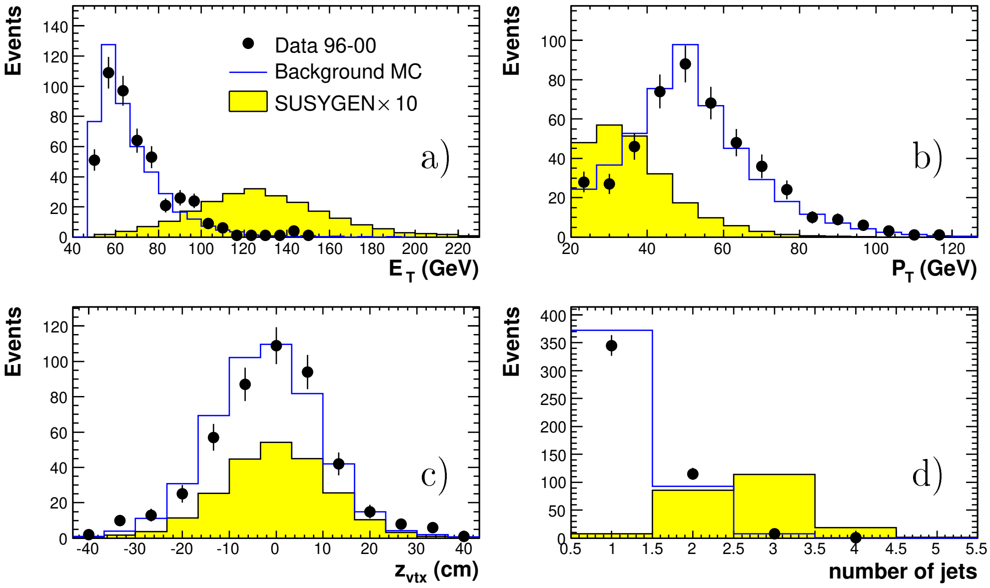

Figure 8.20: Global E_T (a), missing P_T (b), z position of the vertex (c) and total number of jets (d) after the **CC preselection**. The dots represent data, the open histograms denote the background MC and the filled histograms an example SUSYGEN sample, scaled by 10.

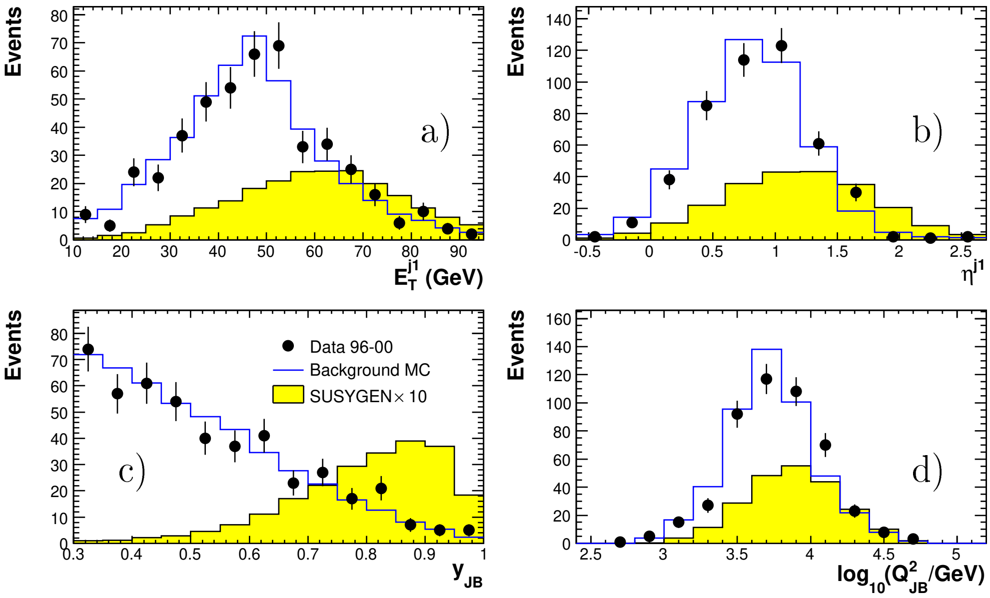

Figure 8.21: Distributions of the transverse energy and pseudo-rapidity for the highest E_T jet and y_{JB} and the logarithm of Q^2_{JB} after the **CC preselection**. The dots represent data, the open histograms denote the background MC and the filled histograms an example SUSYGEN sample, scaled by 10.

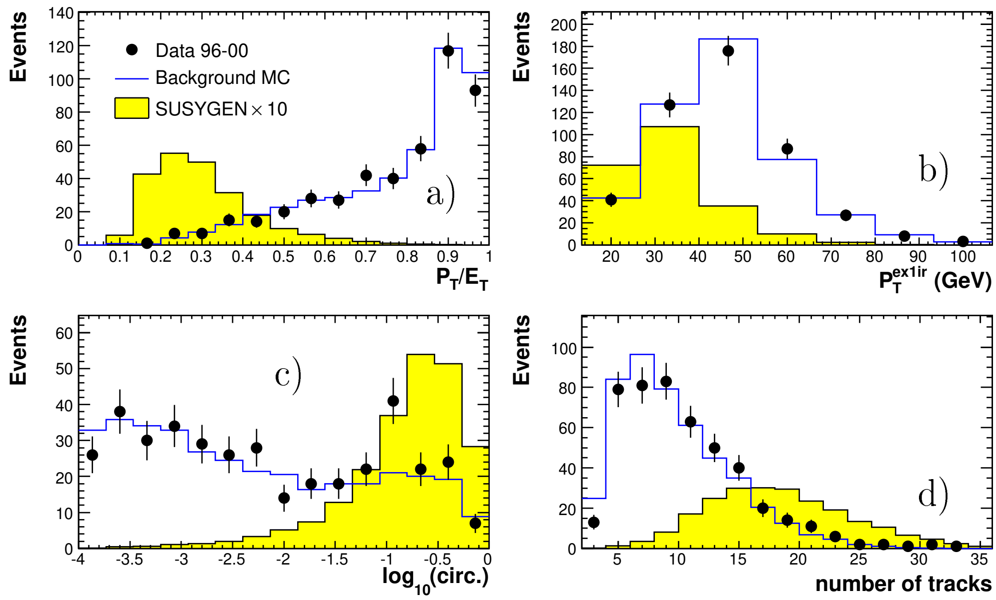

Figure 8.22: P_T/E_T, P_T^{ex1ir}, the logarithm of the circularity and total number of tracks after the **CC preselection**. The dots represent data, the open histograms denote the background MC and the filled histograms an example SUSYGEN sample, scaled by 10.

8.4.2 Multivariate Event Classification

The best input setting for the PDE-RS in the neutrino channel is found to be the one summarised in Table 8.7.

Input	E_T	$\log_{10}(\mathrm{circ.})$	y_{JB}	ntrk	P_T/E_T
Edge length	24 GeV	0.8	0.16	8	0.14

Table 8.7: Final PDE-RS setting for the neutrino channel.

Also in this channel the preselection cuts are relaxed for the training samples in order to gain higher statistics. The background training sample is a superset of the background test sample, due to statistical limitations. It consists of 45,220 events selected from all CC DIS and γp files. The signal training sample contains a mixture of different parameter points and does not intersect with the signal test sample. It contains 75,006 events. The normalisation of the samples is applied as described in Sect. 7.1.2.

The result of the PDE-RS analysis is depicted in Figure 8.23. The performance of the PDE-RS can be seen in Figure 8.18. The MC and the data distribution agree well in all discriminant regions. There is no significant excess in the data at high discriminant values, which is supposed to be the signal region: 10 events with a discriminant larger than 0.94 are observed in the data, while 6.8 ± 2.6 (stat.) are expected from SM background.

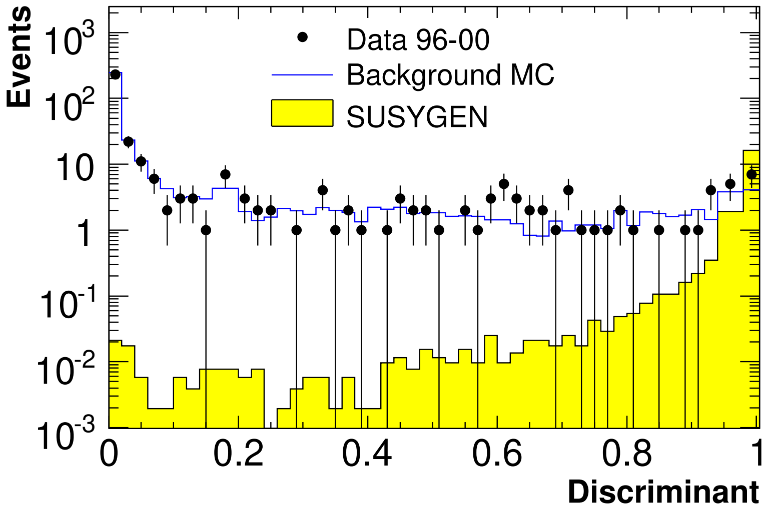

Figure 8.23: Discriminant distribution for the neutrino channel.

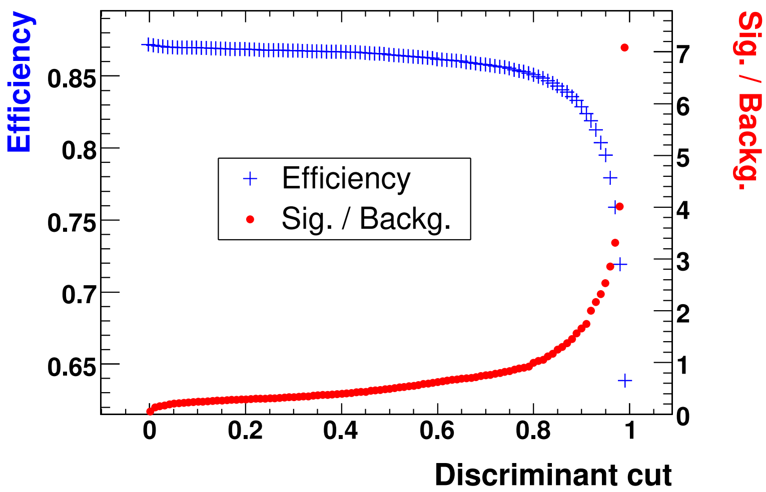

Figure 8.24: Efficiency and signal/background ratio as a function of a discriminant cut in the neutrino channel.

Chapter 9

Interpretation of Results

Since no deviation from the SM is observed in the discriminant distributions, in particular not in the high discriminant region, where the signal is expected to appear, a parameter scan is performed in order to constrain the parameters of the MSSM.

A semi-Bayesian likelihood approach as described in Section 9.2. is used to constrain the parameters μ, M_2 and the masses of the left-handed selectron and the lightest neutralino. In order to maximise the sensitivity, the confidence level (C.L.) values are obtained by a multi-bin evaluation of the discriminant distributions of the data, the SM background and the different SUSY samples after a discriminant cut at 0.75. Systematic uncertainties are taken into account in the limit setting procedure and the considered uncertainty sources are presented in Section 9.2. An interpolation of the C.L. results is performed to obtain the limit contours. The final results are presented in Sections 9.3.1 and 9.3.2 and will be discussed in Chapter 10.

9.1 Systematic Uncertainties

The limit calculation method takes into account each single uncertainty source via a statistical Gaussian variation as described in Section 9.2. All uncertainties are treated as systematics of the MC, due to the low statistics of the data. The following sources of systematic uncertainties are considered in the limit setting procedure:

Experimental Uncertainties

- Luminosity measurement
  The maximal uncertainty on the luminosity measurement is estimated as 2.25% (see Section 4.2.4).

Source	Bg. ($e^{\pm}qq$)	Sig. ($e^{\pm}qq$)	Bg. (νqq)	Sig. (νqq)
Luminosity	2.25%	2.25%	2.25%	2.25%
Energy scale	6.0%	6.0%	6.0%	6.0%
Reweighting	4.0%	4.0%	—	—
$\boldsymbol{E_T}$	$< 0.1\%$	$< 0.1\%$	6.0%	6.0%
$\boldsymbol{z}_{\rm vtx}$	1.5%	1.5%	5.0%	4.0%
$\boldsymbol{E - p_z}$	1.0%	1.0%	—	—
$\boldsymbol{P_T}$	—	—	3.0%	7.0%
$\boldsymbol{P_T^{\rm ex1ir}}$	—	—	5.0%	5.0%
Theory	13.0%	15.0%	10.5%	15.0%

Table 9.1: Systematic effects of the different uncertainty sources.

- Energy scale
  The energy scale of each calorimeter cell is varied by $\pm 1.5\%$ for EMC, $\pm 2.0\%$ for FHAC/BHAC and $\pm 3.0\%$ for RHAC cells. The differences are found not to be larger than 6.0%.

- Reweighting
  The differences in the electron distributions are considered as a source of systematic uncertainties. It is taken into account by the comparison of the discriminant distribution of the reweighted and the non-reweighted events. The differences at large discriminant values ($D > 0.75$) are around 4.0%.

- E_T cut variation
  The E_T cut is varied by ± 5 GeV. There are no significant changes after this variation in the electron channel. In the neutrino channel the uncertainty is estimated as 6.0%.

- $z_{\rm vtx}$ threshold variation
  The $z_{\rm vtx}$ thresholds are varied by ± 10 cm. The differences for this variation are between 1.5% and 5.0%.

- $E - p_z$ threshold variation
  The $E - p_z$ thresholds are varied by ± 2 GeV. Only small changes of around 1.0% are found in the electron channel after this threshold variation.

- P_T cut variation
  The P_T cut is varied by ± 2 GeV. The differences in the neutrino channel are found to be 3.0% and 7.0% for the background and the signal, respectively.

- $P_T^{\rm ex1ir}$ cut variation
  The $P_T^{\rm ex1ir}$ cut is varied by ± 1.5 GeV. The maximal uncertainty found after this variation is smaller than 5.0%.

Theoretical Uncertainties

- Signal cross section

  Three sources for the uncertainty on the signal cross sections are considered:

  - Signal PDF
    SUSYGEN calculates the cross section using the CTEQ5M parametrisation of the parton densities. The effect on the cross section is studied using the newer version CTEQ6M [59] instead. The difference is smaller than 5%.
  - Cross Section Calculation
    Since no NLO calculations are available, the difference to the LO cross sections evaluated by SUSYGEN is estimated as 10%, which is a value, typically obtained in other analyses, where NLO cross section were available. Additionally, the cross sections calculated by SUSYGEN are checked for some points in the parameter space with COMPHEP [60]. The differences found are not larger than 9%. Hence, the uncertainty on the cross section calculation is assumed to be 10%.
  - Interpolation/Cross Section Factors
    The systematic effects from the interpolation procedure and the application of cross section factors to account for the different lepton beams and cms energies are estimated as 10%.

  The uncertainties of all three sources are added in quadrature and the result is taken as the overall theoretical uncertainty on the signal cross sections (15.0%).

- NC DIS Background

  - Up quark PDF
    In $e{+}p$ collisions NC DIS processes are dominated by γ/Z^0 interactions with the up quark in the proton. The uncertainty on the up quark PDF is estimated as 3% [61].
  - MEPS MC
    The colour dipole model as implemented by ARIDANE are used as standard DIS MC in this analysis. If using MEPS MC instead of ARIADNE the differences are up to 7.5% for the NC background.
  - NLO Jets
    The uncertainty of measuring multi-jet events in higher order α_s processes is estimated as 10% [61].

Also here the uncertainties of the three sources are added in quadrature leading to an overall theoretical uncertainty of the NC background cross sections of 13.0%.

- CC DIS Background

  - Down quark PDF
    In $e+p$ collisions CC DIS processes are dominated by $W^{\pm}$ interactions with the down quark in the proton. The uncertainty on the down quark PDF is estimated as 7% [61].
  - MEPS MC
    If using MEPS MC instead of ARIADNE the differences are up to 7.5% for the CC background.

  The uncertainties of both sources are added in quadrature which leads to an overall theoretical uncertainty of the CC background cross sections of 10.5%.

The effects of the considered systematic uncertainties are summarised in Table 9.1.

9.2 Confidence Level Calculation

An efficient way to combine the results of two or more independent search channels and to calculate confidence levels has been presented by T. Junk in [62]. The method is based on the multi-bin strategy proposed by A. Favara and M. Pieri [63]. Systematic uncertainties are taken into account using a generalisation of the method proposed by R.D. Cousins and V.L. Highland [64], and a similar approach by C. Giunti [65]. The T. Junk method has been implemented in the framework of the ROOT analysis package [66].

For the case of n independent searches, one may define an estimator function X_i for each search channel i. X_i is identified as the likelihood ratio:

$$X_i = \frac{e^{-(s_i+b_i)}(s_i+b_i)^{d_i}}{d_i!} \quad / \quad \frac{e^{-b_i}b_i^{d_i}}{d_i!}, \tag{9.1}$$

where s_i is the number of expected signal events, b_i the number of expected background events and d_i the number of observed events in the i^{th} search channel.

The joint estimator of n channels is just the product of all estimator functions:

$$X_{\text{tot}} = \prod_{i=1}^{n} X_i. \tag{9.2}$$

The probability of simultaneous presence of signal and background ($s+b$ hypothesis) is given by:

$$P_{s+b} = \sum_{X(\{d'_i\}) \leq X(\{d_i\})} \prod_{i=1}^{n} \frac{e^{-(s_i+b_i)}(s_i+b_i)^{d'_i}}{d'_i!}, \tag{9.3}$$

where $X(\{d_i\})$ is the estimator function computed for the observed set of events in each channel $\{d_i\}$, and the sum runs over all possible final outcomes $\{d'_i\}$ which have an estimator less than or equal to the observed one.

The C.L. for the exclusion of a scenario is defined as:

$$CL = 1 - P_{s+b}/P_b, \tag{9.4}$$

where P_b gives the probability for the background only hypothesis. This definition safes against cases with low statistics in small search regions in which even the background only hypothesis can be ruled out, due to statistical fluctuations. Equation (9.4) is a generalisation of the classical single-channel Bayesian approach from the particle data book [67]. The one channel case of Equation (9.4) is identical to the Bayesian formula.

The task of summing the terms of Equation (9.4) is carried out with a Monte Carlo. The different systematic uncertainty sources are included by averaging the quantities X_i and P_i over possible values of the signal and the background, where the uncertainties are assumed to be Gaussian distributed, with a cut off at zero. For example, X_i is computed N times with a Gaussian variation of the expected number of signal and background events, $s_i \pm \sigma^s_{ij}$ and $b_i \pm \sigma^b_{ij}$, where j denotes the different uncertainty sources. The final X_i is obtained from the sum of these values normalised with $1/N$. P_b and P_{s+b} are treated in the same way.

In order to maximise the limits, the confidence levels are obtained by a multi-bin evaluation of the discriminant distributions of the data, the SM background and the different SUSY samples after a discriminant cut at 0.75. This means, every bin with $D \geq 0.75$ in each channel is treated as an independent channel. It has been shown that this strategy maximises the sensitivity of the limit calculation [63], if one takes into account the following considerations:

- Not too small binning:
  Usually, the more analysis bins, the better the sensitivity for the limits. But, if considering systematic uncertainties, in particular the uncertainties on the background estimation, a too small binning can lead to a limit overestimation, due to large fluctuations in some bins.

- Discriminant cut off:
  A cut on the discriminant is often useful, since the limit sensitivity can be worsen for bins with small signal/background ratio ($\lesssim 0.2$). This is also due to systematic uncertainties of the background estimation.

The C.L. presented in the following sections are calculated using the the inclusive electron and the neutrino channel The exclusive 'wrong' sign electron channel is not considered. An overall number of 16 bins, 8 bins for each channel, with $D > 0,75$ ($[0.75, 0.8, 0.85, 0.9, 0.92, 0.94, 0.96, 0.98, 1.00]$) are evaluated. The number of MC experiments is at least $N = 50,000$.

9.3 Constraints on MSSM Parameters

9.3.1 Limits on μ and M_2

A scan of the MSSM parameter space is performed, in order to constrain the parameters μ and M_2. For this purpose, μ and M_2 are varied by typical steps of 15 – 50 GeV in three bins of $\tan\beta = 2, 6, 30$ and for slepton masses of $M_{\tilde{l}} = 100, 120, 140$ GeV, as described in Section 5.3. All squark masses are set to large values of 2 TeV and all slepton masses to be degenerate. It is assumed that one single Yukawa coupling λ'_{1jk} is dominant and the contributions from the other $\not{R}_P$ Yukawa couplings are negligible.

The files listed in Table 5.6 in Section 5.3 are used to estimate the detector acceptances. They are scaled with the cross section obtained from additional SUSYGEN scans with Yukawa couplings of $\lambda'_{111} = 1.0$ and $\lambda'_{121} = 1.0$, respectively. Other possible Yukawa couplings are evaluated but are not shown in the result plots, since their cross sections are so low that no improvement of the LEP limits could be achieved.

Discriminant distributions are computed for all SUSY samples in both search channels. They are evaluated with the corresponding data and background samples and C.L. for all simulated parameter points are calculated by using the limit setting method described in Section 9.2. An interpolation based on Delaunay triangulation[1] is performed to obtain a continuous two-dimensional C.L. coverage in the plane spanned by μ and M_2.

The regions in this plane which can be excluded at 95% C.L. for $\tan\beta = 2, 6, 30$ and slepton masses of 100, 120 and 140 GeV are shown in Figures 9.1-9.9. Also shown are the regions which has been excluded by the ALEPH experiment at LEP. They were obtained from the search for chargino pair production in e^+e^- collisions with cms energies from 189 – 209 GeV. A lower limit of 103 GeV for the $\tilde{\chi}_1^\pm$ mass was derived from this search, which is the most stringent constrain in the gaugino sector to date [69][2]

For photino-like or zino-like gauginos and for slepton masses up to at least

[1]For an introduction and example see [68]. The implementation of the algorithm is part of the ROOT package [66].

[2]The $\tilde{\chi}_1^\pm$ mass limit presented in [69] was derived for large sfermion masses and $\tan\beta = \sqrt{2}$, assuming that only one λ_{ijk}, λ'_{ijk} or $\lambda''{}_{ijk}$ coupling is non-zero.

120 GeV the exclusion limits could be significantly improved. The sensitivity for higgsino-like gauginos is limited, since the production of $\tilde{\chi}^0_{1,2}$ and $\tilde{\chi}^\pm_1$ is suppressed, due to the lower higgsino Yukawa coupling strength with light (s)leptons. Pure higgsinos also have a longer lifetime, which means that they have a higher probability to escape the detector unobserved. This leads to signatures with only one jet and missing P_T or with one jet, missing P_T and a lepton. These cases are not covered by this search. For large $\tan\beta$ the photino content in the $|\mu| \lesssim 100\,\mathrm{GeV}$ band increases and, hence, also the sensitivity in this band increases. The cross sections for a dominant λ'_{111} are larger than for a dominant λ'_{121}, mainly because for the latter case the chargino production channel is not available. This leads to higher exclusion limits for the former case. In cases with other dominant λ'_{ijk} than λ'_{111} or λ'_{121} the cross section is so low that an improvement of existing exclusion limits cannot be obtained. The cross section for λ'_{131} is strongly suppressed, due to the large top mass. For λ'_{112} and λ'_{113} the sensitivity is small, because of the low probability that the slepton interacts with a strange, a bottom, a charm or a top quark in the proton. The same applies to the sensitivity for λ'_{122} and λ'_{133}. Here, additionally, only the chargino production channel is available,

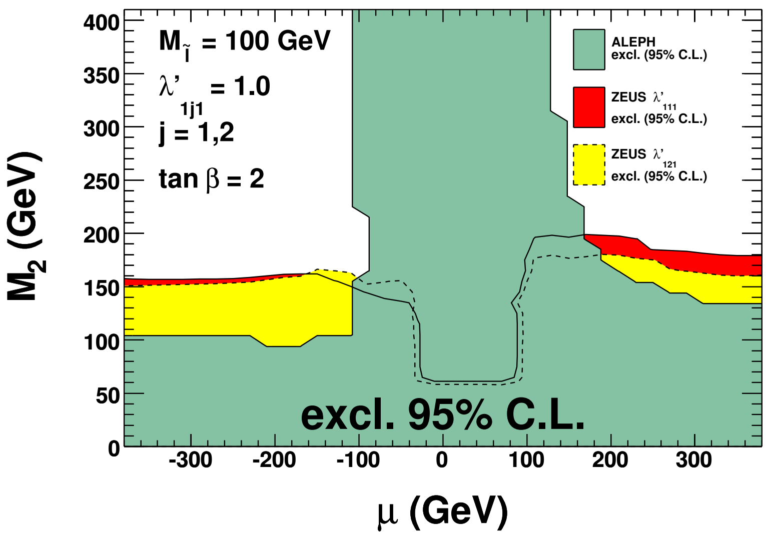

Figure 9.1: Regions in the (μ, M_2)-plane which can be excluded at 95% C.L. by this analysis assuming a $\tan\beta = 2$, slepton masses of 100 GeV and a single dominant Yukawa coupling $\lambda'_{111} = 1.0$ (darkly-shaded area and solid line) or $\lambda'_{121} = 1.0$ (lightly-shaded area and dashed line). Also shown is the region which can be excluded through the lower limit for the $\tilde{\chi}^\pm_1$ mass of 103GeV obtained by the ALEPH experiment at LEP (medium-shaded area) [69].

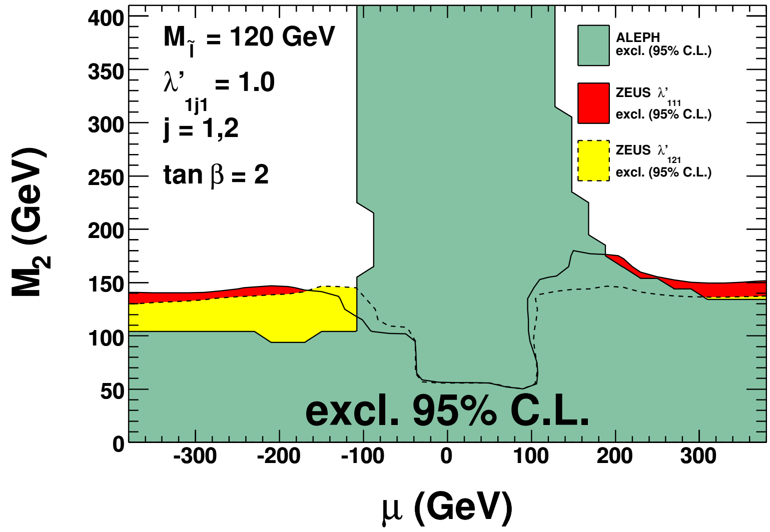

Figure 9.2: Regions in the (μ, M_2)-plane which can be excluded at 95% C.L. by this analysis assuming a $\tan\beta = 2$, slepton masses of 120 GeV and a single dominant Yukawa coupling $\lambda'_{111} = 1.0$ (darkly-shaded area and solid line) or $\lambda'_{121} = 1.0$ (lightly-shaded area and dashed line). Also shown is the region which can be excluded through the lower limit for the $\tilde{\chi}_1^{\pm}$ mass of 103 GeV obtained by the ALEPH experiment at LEP (medium-shaded area) [69].

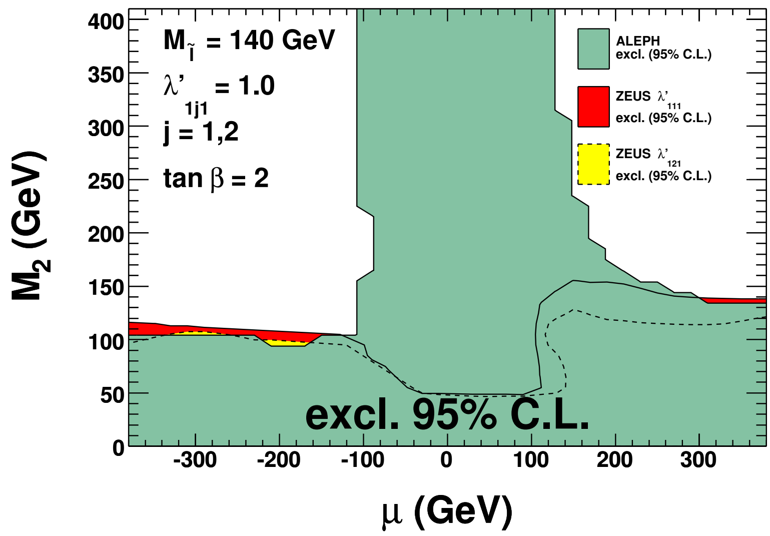

Figure 9.3: Regions in the (μ, M_2)-plane which can be excluded at 95% C.L. by this analysis assuming a $\tan\beta = 2$, slepton masses of 140 GeV and a single dominant Yukawa coupling $\lambda'_{111} = 1.0$ (darkly-shaded area and solid line) or $\lambda'_{121} = 1.0$ (lightly-shaded area and dashed line). Also shown is the region which can be excluded through the lower limit for the $\tilde{\chi}_1^{\pm}$ mass of 103 GeV obtained by the ALEPH experiment at LEP (medium-shaded area) [69].

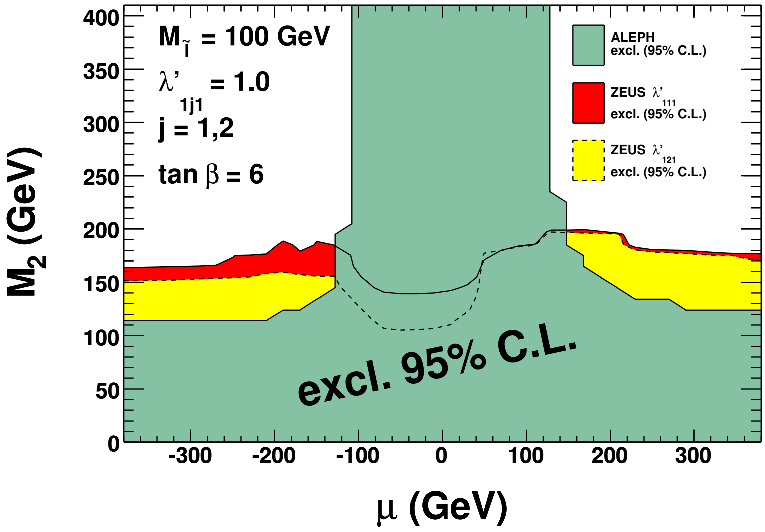

Figure 9.4: Regions in the (μ, M_2)-plane which can be excluded at 95% C.L. by this analysis assuming a $\tan\beta = 6$, slepton masses of 100 GeV and a single dominant Yukawa coupling $\lambda'_{111} = 1.0$ (darkly-shaded area and solid line) or $\lambda'_{121} = 1.0$ (lightly-shaded area and dashed line). Also shown is the region which can be excluded through the lower limit for the $\tilde{\chi}_1^{\pm}$ mass of 103 GeV obtained by the ALEPH experiment at LEP (medium-shaded area) [69].

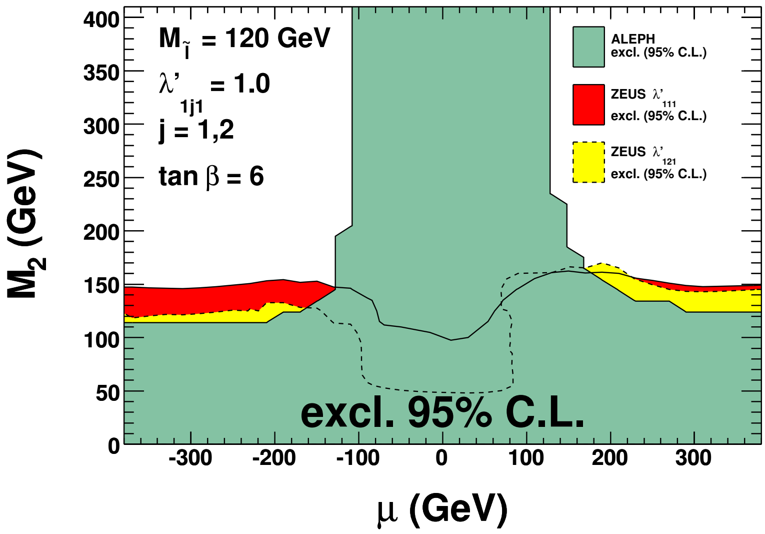

Figure 9.5: Regions in the (μ, M_2)-plane which can be excluded at 95% C.L. by this analysis assuming a $\tan\beta = 6$, slepton masses of 120 GeV and a single dominant Yukawa coupling $\lambda'_{111} = 1.0$ (darkly-shaded area and solid line) or $\lambda'_{121} = 1.0$ (lightly-shaded area and dashed line). Also shown is the region which can be excluded through the lower limit for the $\tilde{\chi}_1^{\pm}$ mass of 103 GeV obtained by the ALEPH experiment at LEP (medium-shaded area) [69].

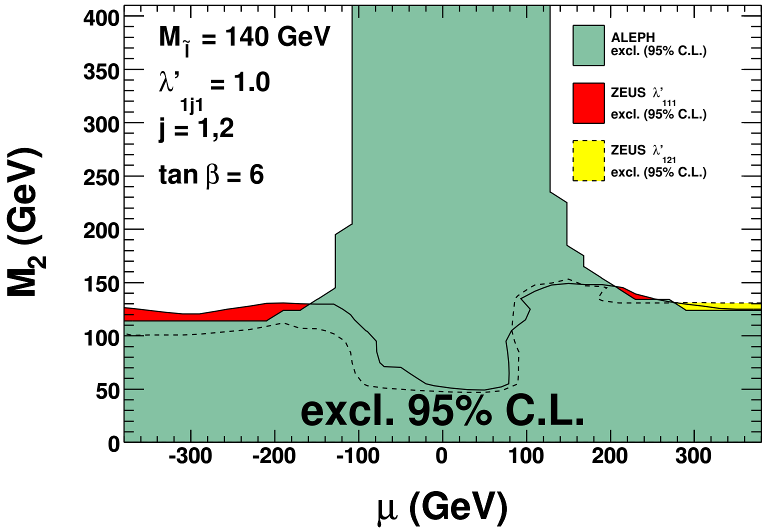

Figure 9.6: Regions in the (μ, M_2)-plane which can be excluded at 95% C.L. by this analysis assuming a $\tan\beta = 6$, slepton masses of 140 GeV and a single dominant Yukawa coupling $\lambda'_{111} = 1.0$ (darkly-shaded area and solid line) or $\lambda'_{121} = 1.0$ (lightly-shaded area and dashed line). Also shown is the region which can be excluded through the lower limit for the $\tilde{\chi}_1^{\pm}$ mass of 103 GeV obtained by the ALEPH experiment at LEP (medium-shaded area) [69].

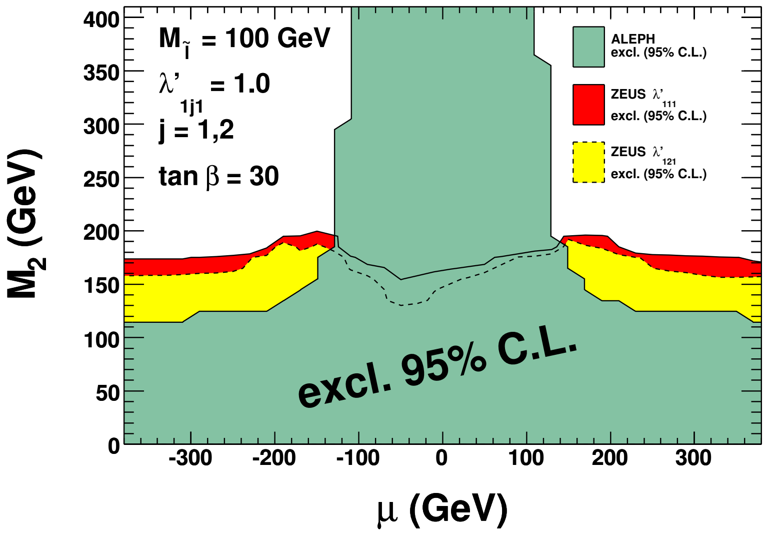

Figure 9.7: Regions in the (μ, M_2)-plane which can be excluded at 95% C.L. by this analysis assuming a $\tan\beta = 30$, slepton masses of 100 GeV and a single dominant Yukawa coupling $\lambda'_{111} = 1.0$ (darkly-shaded area and solid line) or $\lambda'_{121} = 1.0$ (lightly-shaded area and dashed line). Also shown is the region which can be excluded through the lower limit for the $\tilde{\chi}_1^{\pm}$ mass of 103 GeV obtained by the ALEPH experiment at LEP (medium-shaded area) [69].

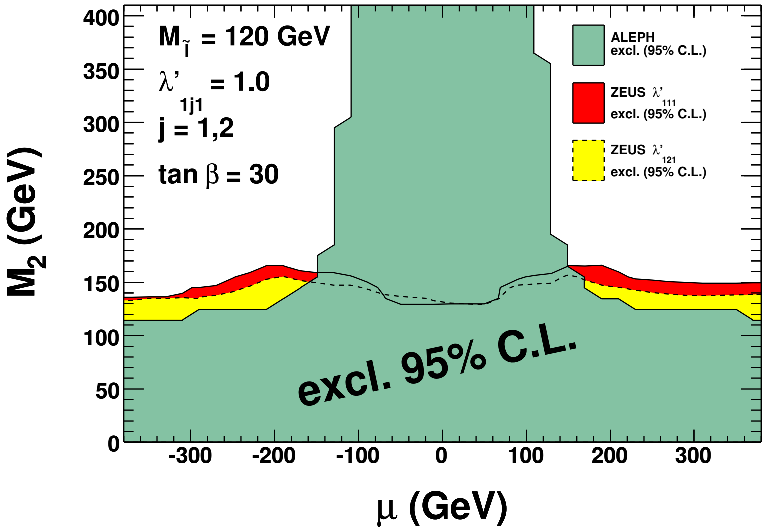

Figure 9.8: Regions in the (μ, M_2)-plane which can be excluded at 95% C.L. by this analysis assuming a $\tan\beta = 30$, slepton masses of 120 GeV and a single dominant Yukawa coupling $\lambda'_{111} = 1.0$ (darkly-shaded area and solid line) or $\lambda'_{121} = 1.0$ (lightly-shaded area and dashed line). Also shown is the region which can be excluded through the lower limit for the $\tilde{\chi}_1^{\pm}$ mass of 103 GeV obtained by the ALEPH experiment at LEP (medium-shaded area) [69].

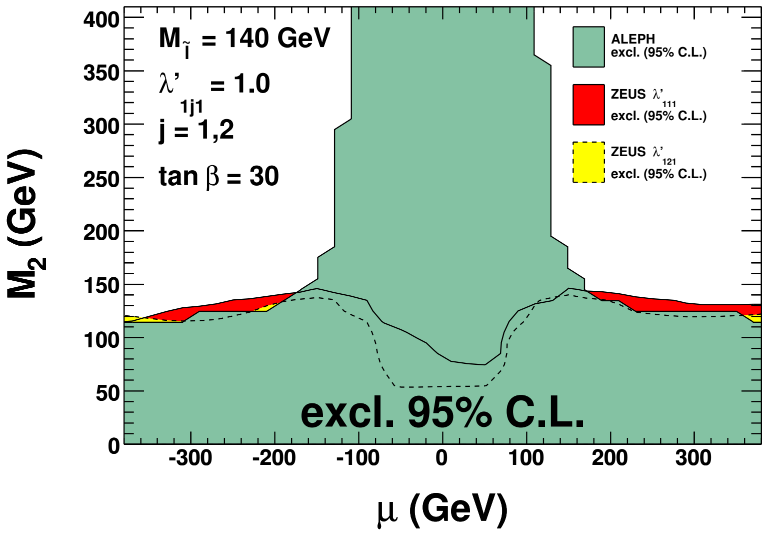

Figure 9.9: Regions in the (μ, M_2)-plane which can be excluded at 95% C.L. by this analysis assuming a $\tan\beta = 30$, slepton masses of 140 GeV and a single dominant Yukawa coupling $\lambda'_{111} = 1.0$ (darkly-shaded area and solid line) or $\lambda'_{121} = 1.0$ (lightly-shaded area and dashed line). Also shown is the region which can be excluded through the lower limit for the $\tilde{\chi}_1^{\pm}$ mass of 103 GeV obtained by the ALEPH experiment at LEP (medium-shaded area) [69].

9.3.2 Limits on $M_{\tilde{\chi}_1^0}$ and $M_{\tilde{e}}$

Additional scans for selectron masses from $40 - 150\,\text{GeV}$ in steps of $10\,\text{GeV}$ and $\tilde{\chi}_1^0$ masses from about $20 - 120\,\text{GeV}$ in typically step of $5 - 10\,\text{GeV}$ are performed with two additional assumptions: The lightest neutralino is the LSP and has a dominant photino component. Exclusion limits in the plane spanned by $M_{\tilde{e}} - M_{\tilde{\chi}_1^0}$ and $M_{\tilde{\chi}_1^0}$ are derived for $\tan\beta = 2, 6, 30$. The contour lines are obtained by a two-dimensional interpolation based on Delaunay triangulation. Figures 9.10-9.12 show the excluded regions for different Yukawa couplings ($\lambda'_{111} = 1.0, 0.5$ and $\lambda'_{121} = 1.0, 0.5$) achieved by this scan[3]. The thick lines in these figures indicate the limits on $M_{\tilde{\chi}_1^0} > 32.5\,\text{GeV}$ [19] and $M_{\tilde{e}_R} > 93\,\text{GeV}$ [69] obtained by the ALEPH and L3 experiments at LEP, respectively. The $\tilde{\chi}_1^0$ mass limit presented in [19] was derived for large sfermion masses and a large $\tan\beta$ range ($0.7 \geq \tan\beta \geq 40$), assuming that only one λ_{ijk}, λ'_{ijk} or λ''_{ijk} coupling is non-zero. The $M_{\tilde{e}_R}$ mass limit shown in [69] was derived for $\tan\beta = 2$, $\mu = -200\,\text{GeV}$ and a dominant λ'_{ijk} coupling.

For $\lambda'_{1j1} = 1.0$, with $j = 1, 2$ the mass limits could be improved significantly by this analysis. LSP masses up to $89\,\text{GeV}$ and left-handed selectron up to 150 GeV can be excluded.

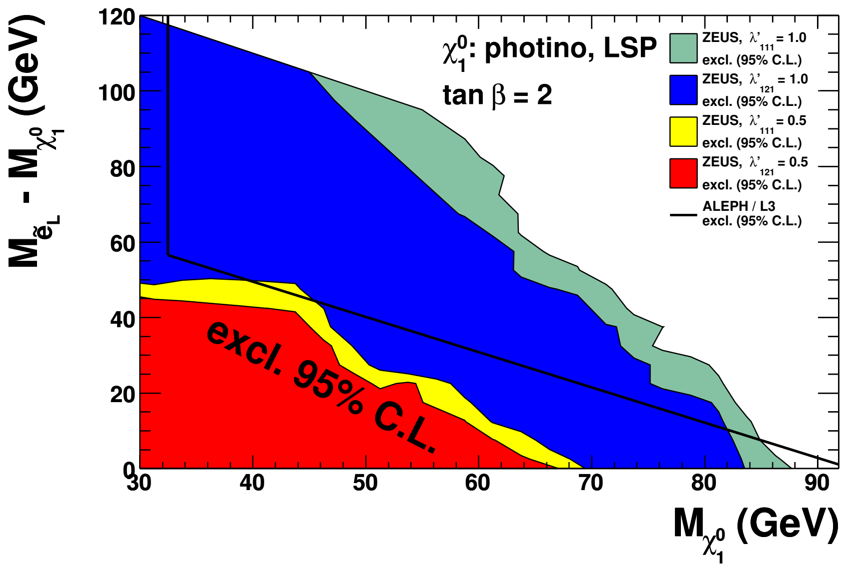

Figure 9.10: Limits in the plane spanned by $M_{\tilde{e}_L} - M_{\tilde{\chi}_1^0}$ and $M_{\tilde{\chi}_1^0}$ for $\tan\beta = 2$, $\lambda'_{111} = 1.0, 0.5$ and $\lambda'_{121} = 1.0, 0.5$. The thick line indicates the limits on $M_{\tilde{e}_L} > 93\,\text{GeV}$ and $M_{\tilde{\chi}_1^0} > 32.5\,\text{GeV}$ obtained by ALEPH and L3 [19, 69].

[3]Here, one should recall that at the hadron level the cross section scales with λ'^2 according to Equations (3.13)–(3.14).

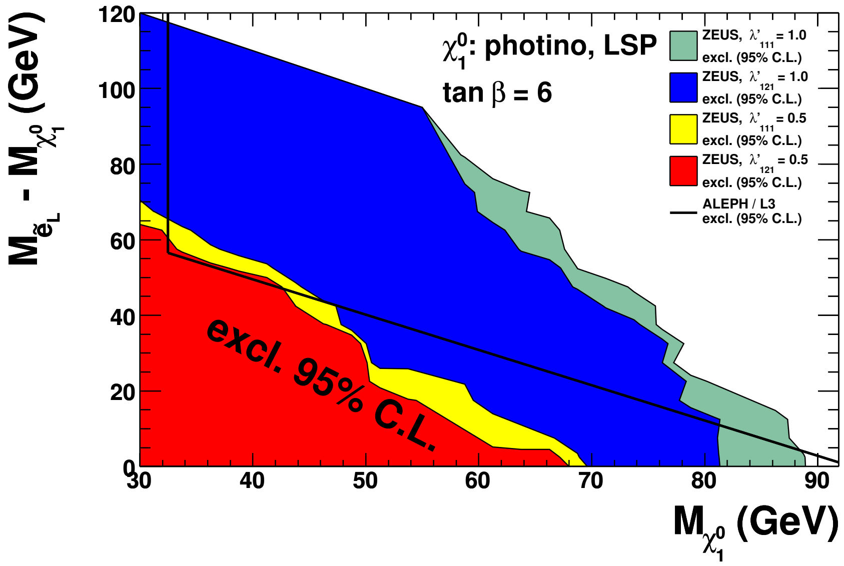

Figure 9.11: Limits in the plane spanned by $M_{\tilde{e}_L} - M_{\tilde{\chi}_1^0}$ and $M_{\tilde{\chi}_1^0}$ for $\tan\beta = 6$, $\lambda'_{111} = 1.0, 0.5$ and $\lambda'_{121} = 1.0, 0.5$. The thick line indicates the limits on $M_{\tilde{e}_L} > 93\,\mathrm{GeV}$ and $M_{\tilde{\chi}_1^0} > 32.5\,\mathrm{GeV}$ obtained by ALEPH and L3 [19, 69].

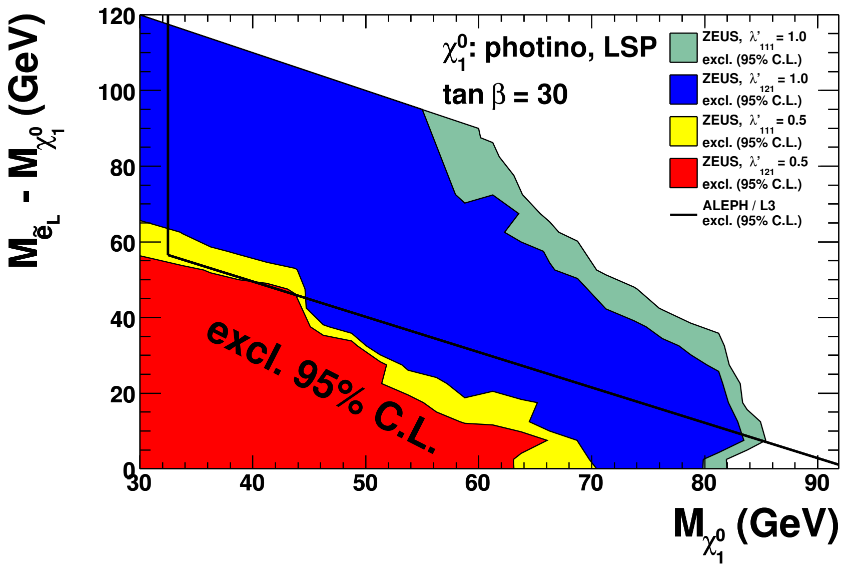

Figure 9.12: Limits in the plane spanned by $M_{\tilde{e}_L} - M_{\tilde{\chi}_1^0}$ and $M_{\tilde{\chi}_1^0}$ for $\tan\beta = 30$, $\lambda'_{111} = 1.0, 0.5$ and $\lambda'_{121} = 1.0, 0.5$. The thick line indicates the limits on $M_{\tilde{e}_L} > 93\,\mathrm{GeV}$ and $M_{\tilde{\chi}_1^0} > 32.5\,\mathrm{GeV}$ obtained by ALEPH and L3 [19, 69].

Chapter 10

Summary & Outlook

Summary

A search for gaugino production in the framework of the R-parity violating MSSM is performed with the ZEUS detector at HERA using a data set corresponding to an integrated luminosity of 121.1 pb^{-1}. The data include events from e^+p and e^-p collisions at a centre of mass energy of 300 and 318 GeV, taken in the years 1996 – 2000.

The analysis makes use of data selections with either an electron or missing P_T in final state, corresponding to neutralino or chargino decays, respectively. The background, which contains mainly of NC DIS and CC DIS events with high momentum transfer, Q^2, is used to control detector effects and the quality of the data selection. A suppression of this background is achieved by exploiting the multi-jet topology of the expected SUSY events in a multi-dimensional likelihood analysis.

No evidence for neutralino or chargino production is found. A parameter scan is performed in the framework of the MSSM in order to constrain the parameters μ, M_2 and the masses of left-handed selectrons and the lightest neutralino $\tilde{\chi}_1^0$.

For tan$\beta = 2, 6, 30$, $\lambda'_{1j1} = 1.0$, with $j = 1, 2$, and for slepton masses up to at least 120 GeV the excluded regions in the (μ, M_2)-plane are extended at 95% C.L. by this analysis compared to previous results from the ALEPH experiment at LEP [69]. The limits in this plane could be improved for regions, where the two lightest neutralinos have dominant photino or zino content, whereas the lightest chargino is wino-like. Regions with dominant higgsino component are not in the reach of this search, due to the small coupling of the higgsino with light (s)leptons.

In addition, limits on the masses of left-handed selectrons and the lightest neutralino are derived assuming that $\tilde{\chi}_1^0$ is the LSP and that it has dominant photino content. The results are presented in the plane spanned by $M_{\tilde{e}_L} - M_{\tilde{\chi}_1^0}$ and $M_{\tilde{\chi}_1^0}$ for $\tan\beta = 2, 6, 30$ and $\lambda'_{1j1} = 0.5, 1.0$, with $j = 1, 2$. Selectron masses up to 150 GeV and LSP masses up to 89 GeV are excluded at 95% C.L. These results are complementary to results from H1 which have searched for gravitinos from a t-channel exchange of an selectron in the framework of GMSB SUSY [70].

All limits obtained are independent of the squark sector and, hence, the strong bounds on squark masses from the Tevatron and low energy experiments do not apply. For example, the coupling λ'_{111} is tightly constrained by the non-observation of neutrinoless double beta decay [5, 6]. However, this limit depends on squark and gluino masses. If $M_{\tilde{u}_L} \gg M_{\tilde{d}_R} \equiv M_{\tilde{q}}$ the limits can be parametrised as follows [6]:

$$\lambda'_{111} \leq 5.6 \times 10^{-4} \left(\frac{M\tilde{q}}{100\,\mathrm{GeV}}\right)^2 \left(\frac{M\tilde{g}}{100\,\mathrm{GeV}}\right)^{1/2} \tag{10.1}$$

The best indirect limits on λ'_{121} and λ'_{131} come from atomic parity violation experiments [7, 71]. The most stringent bounds on λ'_{121} were given as a parametrisation of the left-handed scalar charm or strange quark by H. Dreiner in [7]:

$$\lambda'_{121} \leq 3.5 \times 10^{-2} \left(\frac{M\tilde{q}}{100\,\mathrm{GeV}}\right) \tag{10.2}$$

From the parametrisation, given in Equation (10.1), the coupling λ'_{111}, for gluino and squark masses of 2 TeV, is constrained by the upper limit of 1.0. From Equation (10.2), the upper limit on λ'_{121} becomes 1.0 for squark masses of about 2.85 TeV. This means, for squark and gluino masses of 2.9 TeV and heavier, the low energy constraints do not delimit the results obtained in this analysis.

Future Prospects

At HERA an integrated luminosity of $\sim 700\,\mathrm{pb}^{-1}$ is expected until 2007, shared equally between e^+ and e^-. Since this analysis is background limited, the cross section limit is expected to scale like $\sigma_{\mathrm{limit}} \propto \sqrt{\mathcal{L}}$. With $\sigma_{\mathrm{limit}} \propto \lambda'_{\mathrm{limit}}$, the limit on the Yukawa coupling will scale like $\lambda'_{\mathrm{limit}} \propto \sqrt[4]{\mathcal{L}}$, which will lead to a improvement of the limit on λ' by a factor of $\sqrt[4]{6} \approx 1.5$.

The LHC (Large Hadron Collider), which is supposed to start operation in 2007 and is designed to run at a cms energy of 14 TeV, has a huge potential to discover supersymmetric particles. If SUSY is realised in nature at the TeV energy scale, it is expected that the new experiments at LHC will observe SUSY particles for the first time. If R-parity is conserved, squarks and gluinos can be pair-produced at large rates ($\sim \mathcal{O}(10\,\mathrm{pb})$). Inclusive searches looking for large missing E_T and effective masses would be able to cover a large parameter space very soon. For an integrated luminosity of $1\,\mathrm{fb}^{-1}$ (expected to be achieved within the first two months of design running) the squark and gluino mass reach is estimated as approximately 1.5 TeV at the 5σ discovery level. For an even higher integrated luminosity of $300\,\mathrm{fb}^{-1}$ (expected after three years running at highest design luminosity) the squark and gluino mass reach could be extended to approximately 2.5 – 3.0 TeV [72].

If SUSY would already be discovered by the LHC, the next generation collider, the ILC (International Linear Collider), will then be able to perform precision measurements on parameters for SUSY masses up to $\sim 500\,\mathrm{GeV}$ [73].

Appendix A

Trigger

After events pass the three levels of the ZEUS trigger, they are pre-classified and stored in data summary tapes (DST) bits. These bits allow a fast access to predefined classes of events. In the following the indices FLT, SLT and TLT denote that a quantity is reconstructed at the first, second or third trigger level, whereas the indices FCAL, BCAL and RCAL indicate the different parts of the calorimeter.

A.1 DST B32

The DST bit 32 (B32) is used to select NC DIS events in the data.

These conditions must be satisfied for any electron finder (EM, SIRA95):

1. ExoTLT(4) ***OR*** ExoTLT(5) ***OR*** ExoTLT(7) ***OR*** MuTrig
2. $(E - p_z)^{\mathrm{TLT}} > 32\,\mathrm{GeV}$
3. $E_e^{\mathrm{TLT}} > 4\,\mathrm{GeV}$
4. $Q^2_{e,\mathrm{TLT}} > 160\,\mathrm{GeV}^2$ **OR** $Q^2_{\mathrm{DA,TLT}} > 160\,\mathrm{GeV}^2$
5. $P_{T,e}^{\mathrm{TLT}} > 2\,\mathrm{GeV}$
6. Timing cuts,

where MuTrig denotes the trigger chain, that rejects cosmics and halo muons.

The TLT branches for NC selection are ExoTLT(4), ExoTLT(5) and ExoTLT(7).

For the ExoTLT(4) these conditions has to be fulfilled:

1. ExoSLT(3)

2. $|z^{\mathrm{TLT}}_{\mathrm{vtx}}| < 60$ cm
3. $|t_u - t_d| < 8$ ns,

where $z^{\mathrm{TLT}}_{\mathrm{vtx}}$ indicates the z-position of the CTD vertex. t_u and t_d are the timings measured in the upper and lower half of the calorimeter. Muons produced in atmospheric shower induced by cosmic radiation leave an earlier timing in the upper half of CAL than in the lower half ('earliness'). They are removed by the timing cut.

The requirements for ExoTLT(5) are:

1. $E_T^{\mathrm{TLT}}(ex1ir) > 15\,\mathrm{GeV}$
2. $(E - p_z)^{\mathrm{TLT}} > 32\,\mathrm{GeV}$
3. $E^{\mathrm{TLT}}(\theta > 150^\circ) < 5\,\mathrm{GeV}$
4. $|t_u - t_d| < 8\,\mathrm{ns}$.

These are the requirements for ExoTLT(7):

1. $(E - p_z)^{\mathrm{VC}} > 32\,\mathrm{GeV}$
2. **NOT** BeamGasVertex
3. ≥ 1 electron candidate
4. $(x^{e,\mathrm{TLT}}_{\mathrm{vtx}} + y^{e,\mathrm{TLT}}_{\mathrm{vtx}}) < 30^2$ cm^2
5. $E^e_{\mathrm{TLT}} > 10\,\mathrm{GeV}$
6. $\max(Q^2_{\mathrm{DA,TLT}}, Q^2_{\mathrm{el,TLT}}) > 200\,\mathrm{GeV}^2$.

ExoSLT(3) has the following conditions:

1. $(E - p_z)^{\mathrm{TLT}} > 34\,\mathrm{GeV}$
2. $E_T^{\mathrm{TLT}}(ex2ir) > 16\,\mathrm{GeV}$,

where the terms '$(ex1ir)$' or '$(ex2ir)$' indicate that the transverse energy is calculated excluding the innermost or the two innermost rings of the FCAL, respectively.

A.2 DST B34

The DST bit 34 (B34) is used to select CC DIS events in the data. B34 requires the following conditions:

1. ExoTLT(2) **OR** ExoTLT(6) **OR** $P_T^{\mathrm{TLT}}(ex1ir) > 6\,\mathrm{GeV}$
2. $P_T^{\mathrm{TLT}} > 7\,\mathrm{GeV}$
3. Events which satisfy all of the following eight conditions are vetoed:
   (a) **NOT** ExoTLT(2)
   (b) $P_T^{\mathrm{TLT}}(ex1ir) < 10\,\mathrm{GeV}$
   (c) $P_T^{\mathrm{TLT}} < 25\,\mathrm{GeV}$
   (d) $P_T^{\mathrm{TLT}}/E_T^{\mathrm{TLT}} < 0.7$
   (e) $(E - p_z)^{\mathrm{TLT}} < 10\,\mathrm{GeV}$
   (f) $P_T^{\mathrm{TLT}}/p_z^{\mathrm{TLT}} < 0.08$
   (g) $p_x^{\mathrm{TLT}} < 0\,\mathrm{GeV}$
   (h) $|p_y^{\mathrm{TLT}}| < 4\,\mathrm{GeV}$.

The CC event selection at the TLT is performed by the branches ExoTLT(2) and ExoTLT(6).
For the ExoTLT(2) these conditions has to be fulfilled:

1. $P_T^{\mathrm{FLT}} > 6\,\mathrm{GeV}$
2. $N_{\mathrm{trk}}^{\mathrm{good,TLT}} \geq 1$, with $P_{T,\mathrm{trk}}^{\mathrm{good,TLT}} > 0.5\,\mathrm{GeV}$
   AND DCA $< 1.5\,\mathrm{cm}$ **AND** $|z_{\mathrm{vtx}}^{\mathrm{TLT}}| < 60\,\mathrm{cm}$
3. $|t_u - t_d| < 8\,\mathrm{ns}$.

The requirements of ExoTLT(6) are:

1. ExoSLT(4)
2. $|t_u - t_d| < 8\,\mathrm{ns}$
3. $P_T^{\mathrm{TLT}} > 6\,\mathrm{GeV}$
4. $N_{\mathrm{trk}}^{\mathrm{good,FLT}} \geq 1$ **OR** $E_{\mathrm{FCAL}}^{\mathrm{TLT}} > 10\,\mathrm{GeV}$.

$N_{\mathrm{trk}}^{\mathrm{good,FLT}}$ denote the number of good CTD tracks . For a good track at the FLT the projection of the trajectory in the CTD to the z-direction is required to point to the nominal interaction point.

ExoSLT(4) has the following conditions:

1. $|t_G| < 7\,\mathrm{ns}$
2. $P_T^{\mathrm{SLT}} > 6\,\mathrm{GeV}$
3. $E_T^{\mathrm{SLT}}(ex2ir) > 6\,\mathrm{GeV}$
4. $N_{\mathrm{trk}}^{\mathrm{good,FLT}} \geq 1$ **OR**
   $P_T^{\mathrm{SLT}} > 9\,\mathrm{GeV}$ **AND** $E_T^{\mathrm{SLT}}(ex1ir) > 8\,\mathrm{GeV}$
5. $E_{\mathrm{FCAL}}^{\mathrm{SLT}} > 20\,\mathrm{GeV}$,

where t_G is the global calorimeter timing, which is first available at the SLT. The time zero is calibrated to the electron-proton interaction time.

References

[1] M. Kuze and Y. Sirois, Prog. Part. Nucl. Phys. **50**, 1 (2003); S. Braibant, Preprint hep-ex/0305058, 2003.

[2] J. Butterworth and H. Dreiner, Nucl. Phys. **B 397**, 3 (1993).

[3] H1 Coll., H1 Coll., A. Aktas et al., Eur. Phys. J. **C36**, 425 (2004).

[4] H1 Coll., H1 Coll., A. Aktas et al., Phys. Lett. **B599**, 159 (2004).

[5] R. N. Mohapatra, Phys. Rev. **D34**, 3457 (1986); J. D. Vergados, Phys. Lett. **B184**, 55 (1987); M. Hirsch, H.V. Klapdor-Kleingrothaus and S.G. Kovalenko, *The R-parity violating supersymmetric mechanism of neutrinoless double beta decay.* Prepared for International Workshop on Neutrinoless Double Beta Decay and Related Topics, Trento, Italy, 24 Apr - 5 May 1995; M. Hirsch, H.V. Klapdor-Kleingrothaus and S.G. Kovalenko, Phys. Lett. **B352**, 1 (1995).

[6] M. Hirsch, H.V. Klapdor-Kleingrothaus and S.G. Kovalenko, Phys. Rev. **D53**, 1329 (1996).

[7] H. Dreiner, *Perspectives on Supersymmetry*, G.L. Kane (ed.). World Scientific (1997). Also in preprint hep-ph/9707435.

[8] F. Halzen and A.D. Martin, *Quarks and Leptons: An Introductory Course in Modern Particle Physics.* John Wiley & Sons, Inc, 1984; D. Griffiths, *Introduction to elementary particles.* John Wiley & Sons, Inc., 1987.

[9] S.L. Glashow, Nucl. Phys. **22**, 579 (1961); A. Salam, Phys. Rev. **127**, 331 (1962); S. Weinberg, Phys. Rev. Lett. **19**, 1264 (1967).

[10] A. Mueller (ed.), *Perturbative QCD.* World Scientific, 1989; R.K. Ellis, W.J. Stirling and B.R. Webber, *QCD and Collider Physics*, Cambridge Monographs on Particle Physics, Nuclear Physics and Cosmology, Vol. 8. Cambridge University Press, 1996.

[11] C. Quigg, *Gauge Theories of the Strong, Weak and Electromagnetic Interactions*, in Frontiers in Physics. Benjamin/Cummings, Menlo Park, California, 1983;
T.P. Cheng and L.F. Li, *Gauge Theory of Elementary Particle Physics*. Clarendon Press (Oxford Science Publications), Oxford, UK, 1984.

[12] P.W. Higgs, Phys. Rev. Lett. **13**, 508 (1964);
P.W. Higgs, Phys. Rev. **145**, 1156 (1966).

[13] ZEUS Coll., S. Chekanov, et al., Nucl. Phys. **B627**, 3 (2002).

[14] H1 Coll., A. Aktas et al., Phys. Lett. **B583**, 28 (2004).

[15] ZEUS Coll., J. Breitweg et al., Phys. Lett. **B 471**, 411 (2000).

[16] H.P. Nilles, Phys. Rep. **110**, 1 (1984);
H.E. Haber and G.L. Kane, Phys. Rep. **117**, 75 (1985).

[17] V. Barger, G.F. Giudice and T. Han, Phys. Rev. **D 40**, 2987 (1989).

[18] S. Katsanevas and P. Morawitz, Comput. Phys. Commun. **112**, 227 (1998);
N. Ghodbane, Preprint hep-ph/9909499, 1999;
E. Perez, *Proc. Workshop on Monte Carlo Generators for HERA Physics*, G. Grindhammer, G. Ingelman, H. Jung and T. Doyle (eds.). DESY, Hamburg, Germany (1999). Also in preprint DESY-PROC-1999-02, available on `http://www.desy.de/~heramc/`. (Plenary Starting Meeting), Hamburg, Germany, 27-30 Apr 1998.

[19] L3 Coll., M. Acciarri et al., Eur. Phys. J. **C19**, 397 (2001).

[20] E. Perez, Y. Sirois and H. Dreiner, *Future Physics at HERA*, G. Ingelman, A. De Roeck, R. Klanner (ed.), Vol. 1, pp. 295–311. DESY, Hamburg, Germany (1996). Also in preprint hep-ph/9703444.

[21] H. Dreiner and P. Morawitz, Nucl. Phys. **B428**, 31 (1994).

[22] H. Dreiner, S. Lola and P. Morawitz, Phys. Lett. **B389**, 62 (1996).

[23] G.A. Voss and B.H. Wiik, Ann. Rev. Nucl. Part. Sci. **44**, 413 (1994).

[24] M. Seidel, *The Upgraded Interaction Regions of HERA* (unpublished). DESY-HERA-00-01;
U. Schneekloth (ed.), Preprint HERA-98-05, DESY, 1998, available on `http://www.desy.de/~ahluwali/HERA-98-05`.

[25] ZEUS Coll., U. Holm (ed.), *The ZEUS Detector*. Status Report (unpublished), DESY (1993), available on `http://www-zeus.desy.de/bluebook/bluebook.html`.

[26] M. Derrick et al., Nucl. Inst. Meth. **A 309**, 77 (1991);
A. Andresen et al., Nucl. Inst. Meth. **A 309**, 101 (1991);
A. Caldwell et al., Nucl. Inst. Meth. **A 321**, 356 (1992);
A. Bernstein et al., Nucl. Inst. Meth. **A 336**, 23 (1993).

[27] D.G. Cussans et al., Nucl. Inst. Meth. **A 315**, 397 (1992);
B. Foster et al., Nucl. Phys. Proc. Suppl. **B 32**, 181 (1993);
B. Foster et al., Nucl. Inst. Meth. **A 338**, 254 (1994).

[28] A. Garfagnini, Nucl. Inst. Meth. **A 435**, 34 (1999);
C. Coldewey, Nucl. Inst. Meth. **A 447**, 44 (2000);
E.N. Koffeman, for the ZEUS MVD group, Nucl. Inst. Meth. **A 453**, 89 (2000);
C. Coldewey, for the ZEUS MVD group, Nucl. Inst. Meth. **A 453**, 149 (2000).

[29] D. Kisielewska et al., Nukleonika **31**, 205 (1986). Also in Report DESY-HERA-85-25;
J. Andruszków et al., Preprint DESY-92-066, DESY, 1992;
J. Andruszków et al., Acta Phys. Pol. **B 32**, 2025 (2001).

[30] ZEUS Coll., R. Carlin et al., Nucl. Inst. Meth. **A 379**, 542 (1996);
G.P. Heath et al., Nucl. Inst. Meth. **A 315**, 431 (1992).

[31] L. Lönnblad, Comp. Phys. Comm. **71**, 15 (1992).

[32] V.N. Gribov and L.N. Lipatov, Sov. J. Nucl. Phys. **15**, 438 (1972);
Y.L. Dokshitzer, Sov. Phys. JETP **46**, 641 (1977);
G. Altarelli and G. Parisi, Nucl. Phys. **B 126**, 298 (1977).

[33] M. Bengtsson and T. Sjöstrand, Comp. Phys. Comm. **46**, 43 (1987);
T. Sjöstrand and M. Bengtsson, Comp. Phys. Comm. **43**, 367 (1987);
T. Sjöstrand, Comp. Phys. Comm. **39**, 347 (1986).

[34] G. Marchesini et al., Comp. Phys. Comm. **67**, 465 (1992);
G. Corcella et al., Journal of High Energy Phys. **01**, 010 (2001).

[35] K. Charchula, G.A. Schuler and H. Spiesberger, Comp. Phys. Comm. **81**, 381 (1994);
H. Spiesberger, *HERACLES and DJANGOH: Event Generation for ep Interactions at HERA Including Radiative Processes*, 1998, available on `http://www.desy.de/~hspiesb/djangoh.html`.

[36] G. Ingelman, A. Edin and J. Rathsman, Comp. Phys. Comm. **101**, 108 (1997).

[37] A. Kwiatkowski, H. Spiesberger and H.-J. Möhring, Comp. Phys. Comm. **69**, 155 (1992). Also in *Proc. Workshop Physics at HERA*, 1991, DESY, Hamburg.

[38] CTEQ Coll., H.L. Lai et al., Eur. Phys. J. **C 12**, 375 (2000).

[39] CTEQ Coll., H.L. Lai et al., Phys. Rev. **D55**, 1280 (1997);
T. Sjöstrand et al., Comp. Phys. Comm. **135**, 238 (2001);
T. Sjostrand, L. Lonnblad and S. Mrenna, *PYTHIA 6.2: Physics and manual*, 2001.

[40] T. Abe, Comp. Phys. Comm. **136**, 126 (2001).

[41] T. Sjöstrand, Comp. Phys. Comm. **82**, 74 (1994).

[42] U. Baur, J.A.M. Vermaseren and D. Zeppenfeld, Nucl. Phys. **B375**, 3 (1992).

[43] R. Brun, F. Bruyant, M. Maire, A.C. McPherson and P. Zanarini, 1987. CERN-DD/EE/84-1.

[44] G.M. Briskin, *Diffractive Dissociation in ep Deep Inelastic Scattering.* Ph.D. Thesis, Tel Aviv University, 1998. (Unpublished).

[45] N. Tuning, *ZUFOs: Hadronic Final State Reconstruction with Calorimeter, Tracking and Backsplash Correction* (unpublished). ZEUS-Note-01-021, 2001.

[46] S. Bentvelsen, J. Engelen and P. Kooijman, *Proc. Workshop on Physics at HERA*, W. Buchmüller and G. Ingelman (eds.), Vol. 1, p. 23. Hamburg, Germany, DESY (1992).

[47] F. Jacquet and A. Blondel, *Proc. the Study of an eP Facility for Europe*, U. Amaldi (ed.), p. 391. (1979). Also in preprint DESY 79-48.

[48] G.F. Hartner, *VCTRAK(3.07/04): Offline Output Information* (unpublished). ZEUS-97-064, internal ZEUS-note, 1997;
G. F. Hartner, *VCTRAK Briefing: Program and Math* (unpublished). Zeus-98-058, internal ZEUS-note, 1998.

[49] S.D. Ellis and D.E. Soper, Phys. Rev. **D 48**, 3160 (1993);
S.Catani et al., Nucl. Phys. **B406**, 187 (1993);
S. Catani and M. H. Seymour, Nucl. Phys. **B**, 291 (1997).

[50] B. Straub, *The em Electron Finder*, 1998, available on `http://www.desy.de/~straub/ZEUS_ONLY/doc/em.ps`.

[51] A. Kappes, *Application of Neural Networks for the Identification of the Scattered Positron in ep-Events with High Q^2 at ZEUS* (unpublished). ZEUS-Note-98-051, 1998;
H. Abramowicz, A. Caldwell, R. Sinkus, *Neural Network Based Electron Identification in the ZEUS Calorimeter* (unpublished). DESY-95-054;
A. Kappes, *Verwendung Neuronaler Netze zur Identifikation des gestreuten Elektrons in ep-Ereignissen mit hohem Q^2 bei ZEUS.* Diploma Thesis, Universität Bonn, Bonn, Germany, Report BONN-IB-97-28, 1997, available on
`http://www-zeus.physik.uni-bonn.de/german/diploma.html`.

[52] A. López-Durán Viani and S. Schlenstedt, *Electron Finder Efficiencies and Impurities. A Comparison Between SINISTRA95, EM and EMNET* (unpublished). ZEUS-99-077, internal ZEUS note, 1999.

[53] S. Brandt and H.D. Dahmen, Zeit. Phys. **C1**, 61 (1979).

[54] H.B. Prosper, *Multivariate methods: A unified perspective.* Prepared for Conference on Advanced Statistical Techniques in Particle Physics, Durham, England, 18-22 Mar 2002;
J. Zimmermann and C. Kiesling, Nucl. Instrum. Meth. **A534**, 204 (2004);
K.H. Becks, F. Block, J. Drees, P. Langefeld and F. Seidel, Nucl. Instrum. Meth. **A329**, 501 (1993).

[55] T. Carli and B. Koblitz, Nucl. Instrum. Meth. **A501**, 576 (2003);
B. Koblitz, *Search for instanton-induced processes with the H1 detector in deep-inelastic electron proton collisions at HERA.* Ph.D. Thesis, Universität Hamburg, 2002. DESY-THESIS-2002-015.

[56] R. Sedgewick, *Algorithms in C++.* Addison Wesley (Boston, USA), 1992. Chapter 26.

[57] ZEUS Coll., S. Chekanov et al., Eur. Phys. J. **C 21**, 443 (2001).

[58] K. Nagano, *Measurement of Charged-Current e^+p Deep Inelastic Scattering Cross Sections at $\sqrt{s} = 300\,GeV$.* Ph.D. Thesis, University of Tokyo, 1999. (unpublished);
A.D. Tapper, *Measurement of charged current deep inelastic scattering cross sections using the ZEUS detector at HERA.* Ph.D. Thesis, University of London, 2001. (unpublished).

[59] S. Kretzer, H.L. Lai, F.I. Olness and W.K. Tung, Phys. Rev. **D69**, 114005 (2004).

[60] E. Boos et al., Nucl. Instrum. Meth. **A534**, 250 (2004);
A. Semenov, Nucl. Instrum. Meth. **A502**, 558 (2003).

[61] ZEUS Coll., S. Chekanov et al., Eur. Phys. J. **C42**, 1 (2005).

[62] T. Junk, Nucl. Instrum. Meth. **A434**, 435 (1999).

[63] A. Favara and M. Pieri, Preprint hep-ex/9706016, 1997;
G.J. Feldman and R.D. Cousins, Phys. Rev. **D57**, 3873 (1998).

[64] R.D. Cousins and V.L. Highland, Nucl. Instrum. Meth. **A320**, 331 (1992).

[65] C. Giunti, Phys. Rev. **D59**, 113009 (1999).

[66] R. Brun, F. Rademakers, P. Canal and M. Goto, ECONF **C0303241**, MOJT001 (2003);
R. Brun, F. Rademakers and S. Panacek, *ROOT, an object oriented data analysis framework.* Prepared for CERN School of Computing (CSC 2000), Marathon, Greece, 17-30 Sep 2000.

[67] S. Eidelman et al., Phys. Lett. **B592** (2004).

[68] M. Bern, and D. Eppstein, *Computing in Euclidean Geometry.* World Scientific, Singapore, 1992.

[69] ALEPH Coll., A. Heister et al., Eur. Phys. J. **C31**, 1 (2003);
DELPHI Coll., J. Abdallah et al., Eur. Phys. J. **C36**, 1 (2004);
L3 Coll., P. Achard et al., Phys. Lett. **B524**, 65 (2002);
OPAL Coll., G. Abbiendi et al., Eur. Phys. J. **C11**, 619 (1999).

[70] H1 Coll., A. Aktas et al., Phys. Lett. **B616**, 31 (2005).

[71] P. Langacker, Phys. Lett. **B256**, 277 (1991);
C.S. Wood et al., Science **275**, 1759 (1997).

[72] *ATLAS detector and physics performance. Technical design report. Vol. 2.* CERN-LHCC-99-15;
CMS Coll., S. Abdullin et al., Preprint hep-ph/9806366, 2002;
S. Abdullin and F. Charles, Nuclear Physics B **547**, 60 (1999).

[73] American Linear Collider Working Group, T. Abe et al., Preprint hep-ex/0106056, 2001;
American Linear Collider Working Group, T. Abe et al., Preprint hep-ex/0106057, 2001.

List of Figures

List of Tables

Acknowledgements

I would like to thank Peter for his support and advices throughout the recent years. Thanks also to Wolfram and the referees of my thesis and the defense, Herrn Joachim Meyer, Herrn Robert Klanner and Achim. It was a pleasure to work with all the members of the High-Q^2 and the Synchrotron radiation background group: Claus, Tancredi, Alessandro, Lorenzo, Elisabetta, Katarzyna, Kunihiro, Alex, Masahiro, Enrico, Bruce, Nichol, James, Ingo, Nicola, Uwe et al. The setup of the test-beam stand would have been impossible without the help of Uli Kötz, Gregor, Ingrid, Jaap and Norbert Meyners. And of course, I want to thank all students at ZEUS for having a very good time at DESY: Raquel, Amita, Liz, Sonja, Heuijim, Volker, Benjamin, Oli, Dominik, Damir, John, Alessio, Devis, Uli and many others.